PALLADIUM (Pd) DECORATED ZINC OXIDE (ZnO) NANOPARTICLES FOR GAS SENSING APPLICATIONS: MEAT SPOILAGE GASES

Dissertation submitted in fulfilment of the requirements for the degree of Master of Science in the:

FACULTY OF SCIENCE AGRICULTURE AND ENGINEERING

DEPARTMENT OF PHYSICS

UNIVERSITY OF ZULULAND

Supervisors: Mr. T Mpanza and Dr S.E Mavundla

Co-Supervisor: Dr. C. L Ndlangamandla

Submitted by

K.B Manqele

February 2024

DECLARATION

I hereby declare that this is my original work, that it has not been submitted for credit towards a degree or test at any other university, and that any sources I have used or mentioned have been properly cited.

Signature:……… K.B M ………………..

Date:…7 April 2024………………………………………………..

ABSTRACT

The detection of odours emitted by meat products when they start to spoil remains a challenge. In response to this, materials of ZnO decorated with palladium nanoparticles were synthesised using the hydrothermal method for the purpose of testing their gas sensing properties. After the synthesis of these nanoparticles, various characterization techniques for the investigation of both physical and chemical properties were employed. Different percentages of Palladium ranging between 0.2% and 0.7% from a $PdCl_2$ precursor with 99.9% purity were used during the synthesis. A gas sensor was fabricated through the drop casting method on a gold grid. These gas sensor samples were exposed to both reducing and oxidizing gases. Sensing was performed at a temperature from 25°C to 225°C. The best result was obtained at 150°C using 0.2%Pd-ZnO sensor for NO_2 gas sensing. A sensitivity of 3.8 was recorded, with both response time and recovery time of 3.5 minutes. The 0.5%Pd-ZnO sensor performs well at room temperature for CO_2, SO_2, and ethanol gases.

IsiZulu version

Ukutholakala kwephunga elikhishwa yinyama lapho isiqala ukubola kuseyinselelo. Ukuphendula lokhu, izinto ze-ZnO ezihlotshiswe nge-palladium (Pd) nanoparticles zahlanganiswa kusetshenziswa indlela ye-hydrothermal ngenhloso yokuhlola izakhiwo zabo zokuzwa igesi. Ngemva kokuhlanganiswa kwalawa ma-nanoparticles, kwasetshenziswa amasu ahlukahlukene kucutshungulwa izakhiwo ezingokomzimba nezamakhemikhali. Amaphesenti ahlukene e-Palladium aphakathi kuka-0.2% no-0.7% kusukela ku- $PdCl_2$ eyandulelayo enobumsulwa obungu-99.9% asetshenziswe ngesikhathi sokuhlanganiswa. Inzwa yegesi yakhiwe ngendlela yokulahla phansi kugridi yegolide. Lawa masampula enzwa yegesi avezwe kukho kokubili amagesi anciphisa nawoku-oxidizing. Ukuzwa kwenziwa ezingeni lokushisa elisuka ku-25°C kuya ku-225°C. Umphumela omuhle kakhulu utholwe ku-150°C kusetshenziswa inzwa engu-0.2% Pd-ZnO yenzwa yegesi engu- NO_2. Ukuzwela kwe-3.8 kwarekhodwa, nakho kokubili isikhathi sokuphendula nesikhathi sokuthola kabusha semizuzu ye-3.5. Inzwa engu-0.5% Pd-ZnO isebenza kahle ekamelweni lokushisa le- CO_2, SO_2, kanye negesi ye-ethanol.

LIST OF ABBREVIATIONS

CO_2: Carbon dioxide

EDS: Energy Dispersive Spectroscopy

H_2S: Hydrogen Sulfide

NO_2: Nitrogen dioxide

O_2: Dioxide

Pd-ZnO: Palladium doped Zinc Oxide

Pd: Palladium

ppm: Parts Per Million

SO_2: Sulfur dioxide

SEM: Scanning Electron Microscope

UV/vis: Ultraviolet visible spectroscopy

XRD: X-ray Diffraction

XPS: X-ray photoelectron spectroscopy

ZnO: Zinc Oxide

ACKNOWLEDGEMENTS

My profound appreciation goes out to almighty **God**, and my advisors for their steadfast support and direction as I completed my Master of Science dissertation. Their knowledge, support, and priceless criticism have been extremely helpful in determining the calibre of this work.

I would also like to thank the following:

Dr C.L. Ndlangamandla, Mr. T Mpanza and Dr S.E. Mavundla for the excellent supervision of this thesis, their guidance, encouragement, and the many stimulating discussions.

Dr Masikane for assisting in XRD characterisation.

The University of the Free State technician for XPS and SEM analysis.

Dr S.E. Mavundla for gas sensing collaboration, and UV/vis analysis with Prof D.E Motaung at University of the Free State.

Mr. Yersultan from the Joint Institute for Nuclear Research at Russia for the Raman technique.

Mr. Cebekhulu and Mr. Sunday for the assistance in plotting the data.

EWSETA, NRF, DSI, JINR, iThemba labs, and the University of Zululand for the Research training and a platform to present my project.

I also want to thank my family, friends, and peers for their support and understanding throughout this academic adventure.

DEDICATION

In honour of my parents, Mr G.H Manqele and Mrs G.N Manqele

TABLE OF CONTENTS

LIST OF FIGURES

LIST OF TABLES

CHAPTER 1- INTRODUCTION

Controlling the gases emitted from meat spoilage poses a major challenge in the food sector, particularly given meat's high perishability despite its rich protein content**[1]**. While technologies such as refrigeration, significantly extend the shelf life of meat products, improper storage practices in the supply chain still result in food loss due to decay**[2, 3]**. Temperature control emerges as a crucial factor affecting both the safety and spoilage rate of meat products throughout the supply chain, underscoring the necessity for systematic temperature management from production to consumption**[4]**. Recent studies have emphasised the impact of temperature variations during handling on product quality, highlighting the importance of maintaining proper refrigeration conditions during transportation and marketing**[5]**. Factors such as cabinet size, initial and targeted storage temperatures, ambient conditions, and energy considerations play key roles in effectively controlling spoilage during storage and transportation processes**[6]**.

When meat is stored at inappropriate temperature it spoils, emitting a lot of dangerous gases such as H_2S, CO_2, NO_2, volatile amines (ammonia, trimethylamine, dimethylamine, methylamine) and other nitrogenous compounds**[7, 8]**. Water content promotes microbial growth, accelerating meats decomposition and spoilage. Thus lower water content in meat results in a longer shelf life**[9]**. These gases contribute to off-flavor and have been utilised as biomarkers for meat quality assessment, as they pose a health risk that could be fatal**[10, 11]**. Spoiled food significantly contributes to incidences of food poisoning and zoonic diseases, which result from consuming foods contaminated with pathogenic bacteria, viruses, or parasites, as well as synthetic or organic toxins**[12-14]**. Typically, illnesses result in nausea and short-term diarrhea that usually goes away on its own**[15]**. Early detection of these substances or their derivatives can mitigate undesirable meat rotting**[16]**.

Gas sensors have emerged as valuable tools for detecting food spoilage and volatile compounds like ammonia. These sensors rely on chemiresistors as the sensing material, undergoing changes in their electrical properties in the presence of specific gases**[17]**. Gas sensor device detects the presence of volatile organic substances qualitatively and quantitatively (concentration) using a chemiresistor**[18]**. These devices come in various classes including electrochemical, optical, gas chromatography, magnetic, and metal oxide semiconducting (MOS), such as SnO2, WO3 and ZnO**[19]**. ZnO is known for its great chemical stability, low cost, and considerable manufacturing flexibility and, is one of the most well-known metal oxides utilised as a sensing material**[20]**. ZnO has a great transparency in the visible wavelength region and low electric resistance**[21]**. The best property of ZnO is the presence of free electrons on its surface, which interact with reducing or oxidizing gas molecules**[22]**.

A typical gas sensing process involves the diffusion of gases to the sensitive surface, followed by adsorption and subsequent reaction with active oxygen species on the surface of the material, resulting in gas exchange and changes in material properties**[23, 24]**. The material used in sensors must have pores or voids facilitating the diffusion of gas molecules, a large specific surface area, and numerous active regions improving gas interaction**[23]**. Metal oxide semiconductors doped with metal ions such as Au, Pb, or Pd, are used to enhance gas sensor response**[25]**. When n-ZnO is combined with low-reactive metals like Au, Ag, and Pd they generate reasonably high Schottky barriers of 0.6–0.8 eV**[26]**. Pd is the best metal to dope with as Au, Pt, Ag, Rh and Ir are costly and need complicated procedures to be implanted on ZnO**[27]**. Pd metal catalyst particles increase the adsorption of oxygen and target gas molecules, which in turn leads to greater changes in the charge-depleted layer and improved detection response.**[28]**. Therefore, Pd-ZnO is a promising material for gas sensing application in monitoring gases emitted by meat spoilage and determining the meat's shelf life**[29, 30]**. Recent studies investigated the sensing capabilities of pure and Pd-decorated ZnO electrodes across temperatures from 25°C to 250°C towards varying concentrations of methylamine (25-400 ppm). Findings demonstrated that while pure ZnO showed a 45.5% response to 400 ppm methylamine at 250°C, ZnO decorated with 18% Pd exhibited a significantly higher response of 99.5%, suggesting that the addition of Pd enhances the sensor response of ZnO gas sensors**[3, 31]**. Gas sensing would allow a more precise assessment of the meat's shelf-life, thus, enabling appropriate action to be taken to prevent the loss of meat, and could provide a basis for regulations to control meat quality**[32].**

In this project, we synthesised ZnO and Pd-ZnO materials for highly sensitive and selective responses towards low concentrations of gases emitted by spoiled meats. We also set out to improve the operating temperature when detecting these gases to lower temperature since high temperatures can result in high energy consumption during sensing. Various doping ratios of Pd in-ZnO were studied for their chemical and physical properties and tested across different temperatures, starting from room temperature. This research aimed to develop advanced gas sensing materials that could enable precise assessment of meat shelf life, thereby facilitating appropriate actions to prevent meat loss and potentially informing regulations to control meat quality.

1.1 Problem statement

Meat is the most consumed food product but it is highly perishable, because of complicated biological and chemical processes**[2]**. More accurate assessment of meat's shelf-life is needed this would then enable appropriate action to be taken to prevent the loss of meat, and the consumption of spoiled meat leading to food safety risk**[33]**. Approximately 600 million individuals, constituting nearly one-tenth of the global population, experience illness following consumption of contaminated food, leading to an annual global burden of around 33 million disability-adjusted life years (DALYs) and 420,000 premature deaths (WHO, 2022a)**[16]**. The number of alternative and reliable approaches to investigating meat decay is growing. This includ pH check, pathogens multiplication and gas sensing**[34]**.

Meat, a high-value nutritional commodity in the human diet, decays at a faster rate when good storage is not implemented. This results in the emission of gases including the animal hormone methylamine**[35]**. Traditional volatile examination of meat freshness and quality assessment, such as gas chromatography and mass spectrometry, is time-consuming and often necessitates multiple sampling preparations and expert analysers**[36, 37]**.

Gas sensors have demonstrated enormous potential application in meat quality and freshness monitoring as a helpful tool for investigating off-odours at an early stage, since they could contribute to speedy and precise examination of the condition of the prior consumption**[38]**. However, despite many successes that have been obtained, there are few reports on gas sensors operating at room temperature with high selectivity and sensitivity. Most sensors are sensitive to gases at high concentration, which renders them less selective, and at high working temperatures which require high energy consumption and thus high cost**[39]**. Among the several types of gas sensors, Pd doped ZnO showed to be a promising sensor for detection of gases emitted by meat spoilage**[40]**. The mission is to detect the gases emitted by spoiling meat at low concentration and at room temperature.

1.2 Research aim.

The aim of the study is to fabricate Pd decorated ZnO gas sensors to detect gases emitted by spoiled meat at low operating temperature.

1.3 Objectives

- Synthesis of ZnO using chemical reagents including Zinc acetate dihydrate ($Zn(CH_3COO)_2 \cdot 2H_2O$), Citric acid monohydrate ($C_6H_8O_7 \cdot H_2O$) and NaOH using hydrothermal method.
- Synthesis of ZnO doped with Pd using reagents including PdCl2, Zinc acetate dihydrate ($Zn(CH_3COO)_2 \cdot 2H_2O$) and NaOH by the hydrothermal method.
- Characterise the final products (ZnO and Pd-decorated ZnO nanostructures) using various techniques: x-ray diffraction (XRD), x-ray photoelectron spectroscopy (XPS), scanning electron microscopy (SEM) with EDS, Raman, and UV/vis Spectroscopy.
- Examine the characteristics of gas sensing, such as response time, recovery time, repeatability, sensitivity, and selectivity of the final products (ZnO and Pd-decorated ZnO nanostructures) towards CO_2, SO_2, NO_2, and Ethanol gas at small concentrations (ppm).

1.4 Significance of the study and possible application

This project addresses food safety in the world caused by modifications, namely, meat alternatives plant and mycoprotein which are utilised as meat substitutes**[41]**. Cultivated meat is produced using in vitro tissue or cell culture (stem cells, myocytes) and altered meat made with genetically engineered animals**[42]**. This project contributes to determining meat shelf-life time and solving the food poising issue caused by spoiled meat sold to customers and meats supplied to stores, by synthesising ZnO and Pd-decorated ZnO material for detecting gases emitted by spoiled meat.

1.5 Dissertation outline

In Chapter 1, an introduction is provided, offering insights into meat and the diverse factors contributing to its spoilage. Chapter 2 delves into a comprehensive literature review, examining the properties of ZnO and Pd in relation to their capabilities in gas sensing applications. Chapter 3 focuses on the characterisation techniques employed and outlines the experimental procedures carried out in the study. Chapter 4 presents the results obtained and initiates a thorough discussion on the findings. The application of gas sensing is explored in Chapter 5, shedding light on its relevance and potential in various contexts. Finally, Chapter 6 consolidates the information presented, offering a concise summary and drawing conclusions from the study's outcomes.

1.6 REFERENCES

1. Mohebi, E. and L. Marquez, *Intelligent packaging in meat industry: An overview of existing solutions.* Journal of food science and technology, 2015. **52**: p. 3947-3964.
2. Zhou, G., X. Xu, and Y. Liu, *Preservation technologies for fresh meat–A review.* Meat science, 2010. **86**(1): p. 119-128.
3. Bruce, J., K. Bosnick, and E.K. Heidari, *Pd-decorated ZnO nanoflowers as a promising gas sensor for the detection of meat spoilage.* Sensors and Actuators B: Chemical, 2022. **355**: p. 131316.
4. Manzini, R. and R. Accorsi, *The new conceptual framework for food supply chain assessment.* Journal of food engineering, 2013. **115**(2): p. 251-263.
5. James, S.J. and C. James, *Chilling and freezing*, in *Food Safety Management*. 2023, Elsevier. p. 453-474.
6. Nychas, G.-J.E., et al., *Meat spoilage during distribution.* Meat science, 2008. **78**(1-2): p. 77-89.
7. Andre, R.S., et al., *Recent progress in amine gas sensors for food quality monitoring: Novel architectures for sensing materials and systems.* ACS sensors, 2022. **7**(8): p. 2104-2131.
8. Dilbaghi, N. and S. Sharma, *Food spoilage, food infections and intoxications caused by microorganisms and methods for their detection*. 2007.
9. Dave, D. and A.E. Ghaly, *Meat spoilage mechanisms and preservation techniques: a critical review.* American Journal of Agricultural and Biological Sciences, 2011. **6**(4): p. 486-510.
10. Sørheim, O., T. Aune, and T. Nesbakken, *Technological, hygienic and toxicological aspects of carbon monoxide used in modified-atmosphere packaging of meat.* Trends in Food Science & Technology, 1997. **8**(9): p. 307-312.
11. Sofos, J.N., et al., *Meat, poultry, and seafood.* Food microbiology: Fundamentals and frontiers, 2012: p. 109-167.
12. Pellissery, A.J., et al., *Spoilage bacteria and meat quality*, in *Meat quality analysis*. 2020, Elsevier. p. 307-334.
13. Borchers, A., et al., *Food safety.* Clinical reviews in allergy & immunology, 2010. **39**: p. 95-141.
14. Aljamali, N.M., *Review on food poisoning (types, causes, symptoms, diagnosis, treatment).* Global Academic Journal of Pharmacy and Drug Research, 2021. **3**(4): p. 54-61.
15. Ericsson, C.D. and H.L. DuPont, *Travelers' diarrhea: approaches to prevention and treatment.* Clinical infectious diseases, 1993: p. 616-624.
16. Joshi, N., G. Pransu, and C. Adam Conte-Junior, *Critical review and recent advances of 2D materials-Based gas sensors for food spoilage detection.* Critical Reviews in Food Science and Nutrition, 2022: p. 1-24.

17. Matindoust, S., et al., *Polymer-based gas sensors to detect meat spoilage: A review.* Reactive and Functional Polymers, 2021. **165**: p. 104962.
18. Hulanicki, A., S. Glab, and F. Ingman, *Chemical sensors: definitions and classification.* Pure and applied chemistry, 1991. **63**(9): p. 1247-1250.
19. Phanichphant, S., *Semiconductor metal oxides as hydrogen gas sensors.* Procedia Engineering, 2014. **87**: p. 795-802.
20. Shah, N.A., et al., *Synthesis of metal oxide semiconductor nanostructures for gas sensors.* Gas Sensors, 2019. **1**: p. 101.
21. Dimitrov, I., et al. *Al doped ZnO thin films for gas sensor application*. in *Journal of Physics: Conference Series*. 2008. IOP Publishing.
22. Reddy, B.K.S. and P.H. Borse, *Recent material advances and their mechanistic approaches for room temperature chemiresistive gas sensors.* Journal of The Electrochemical Society, 2021. **168**(5): p. 057521.
23. Constantinoiu, I. and C. Viespe, *ZnO metal oxide semiconductor in surface acoustic wave sensors: A review.* Sensors, 2020. **20**(18): p. 5118.
24. Mujahid, A. and F.L. Dickert, *Surface acoustic wave (SAW) for chemical sensing applications of recognition layers.* Sensors, 2017. **17**(12): p. 2716.
25. Cheng, P., et al., *Investigation of doping effects of different noble metals for ethanol gas sensors based on mesoporous In2O3.* Nanotechnology, 2021. **32**(30): p. 305503.
26. Pearton, S., et al., *Recent progress in processing and properties of ZnO.* Superlattices and Microstructures, 2003. **34**(1-2): p. 3-32.
27. Finkelstein, D.A., et al., *Trends in catalysis and catalyst cost effectiveness for N2H4 fuel cells and sensors: a rotating disk electrode (RDE) study.* The Journal of Physical Chemistry C, 2016. **120**(9): p. 4717-4738.
28. Li, Z., et al., *Advances in designs and mechanisms of semiconducting metal oxide nanostructures for high-precision gas sensors operated at room temperature.* Materials Horizons, 2019. **6**(3): p. 470-506.
29. Zhou, T. and T. Zhang, *Recent progress of nanostructured sensing materials from 0D to 3D: overview of structure–property-application relationship for gas sensors.* Small Methods, 2021. **5**(9): p. 2100515.
30. Theerthagiri, J., et al., *A review on ZnO nanostructured materials: energy, environmental and biological applications.* Nanotechnology, 2019. **30**(39): p. 392001.
31. Hu, J., et al., *Optimization of Pd content in ZnO microstructures for high-performance gas detection.* Journal of Materials Science, 2015. **50**: p. 1935-1942.
32. Pereira, P.F., et al., *Electrical gas sensors for meat freshness assessment and quality monitoring: A review.* Trends in Food Science & Technology, 2021. **118**: p. 36-44.

33. Omanović-Mikličanina, E. and M. Maksimović, *Nanosensors applications in agriculture and food industry.* Bull Chem Technol Bosnia Herzegovina, 2016. **47**: p. 59-70.
34. Bryan, F.L. and W.H. Organization, *Hazard analysis critical control point evaluations: a guide to identifying hazards and assessing risks associated with food preparation and storage*. 1992: World Health Organization.
35. Suganya, T., et al., *Macroalgae and microalgae as a potential source for commercial applications along with biofuels production: a biorefinery approach.* Renewable and Sustainable Energy Reviews, 2016. **55**: p. 909-941.
36. Wilkes, J.G., et al., *Sample preparation for the analysis of flavors and off-flavors in foods.* Journal of Chromatography A, 2000. **880**(1-2): p. 3-33.
37. Brattoli, M., et al., *Gas chromatography analysis with olfactometric detection (GC-O) as a useful methodology for chemical characterization of odorous compounds.* Sensors, 2013. **13**(12): p. 16759-16800.
38. Berna, A., *Metal oxide sensors for electronic noses and their application to food analysis.* Sensors, 2010. **10**(4): p. 3882-3910.
39. Liu, X., et al., *A survey on gas sensing technology.* Sensors, 2012. **12**(7): p. 9635-9665.
40. Wyszynski, B. and T. Nakamoto, *Chemical sensors*, in *Flavour development, analysis and perception in food and beverages*. 2015, Elsevier. p. 83-104.
41. Liu, W., et al., *Assuring food security: consumers' ethical risk perception of meat substitutes.* Agriculture, 2022. **12**(5): p. 671.
42. Kadim, I.T., et al., *Cultured meat from muscle stem cells: A review of challenges and prospects.* Journal of Integrative Agriculture, 2015. **14**(2): p. 222-233.

CHAPTER 2-LITERATURE REVIEW

2.1 Meat Spoilage

The increased transportation and bulk storage of meat, driven in South Africa by factors such as population growth and the expansion of supermarkets, have intensified scientific interest in understanding and detecting meat spoilage**[1]**. Meat decay is primarily caused by chemical processes like oxidation and enzymatic autolysis, resulting in unpleasant odours, bitter flavours, and slime formation, rendering the meat unsuitable for consumption**[2]**. Enzymes and bacteria further degrade nutrients in meat, leading to the formation of aldehydes, ketones, and alcohols, reducing the meat's quality and shelf life**[3]**. Volatile compounds such as H_2S and NH_3 gases are then emitted, serving as key indicators of meat freshness during storage**[4]**. Other gases and volatile substances, including CO, CH_4, SO_2, alcohols, amines, and sulfur, are generated as meat spoilage progresses**[5]**. The proliferation of microorganisms in contaminated meats is influenced by factors like cleanliness, added ingredients, processing conditions, and temperature-related storage conditions**[6]**. In the absence of refrigeration, microorganisms thrive, leading to meat decomposition and significant economic losses**[7]**. Consuming improperly checked meat poses health risks, including food poisoning and zoonotic diseases related to the transfer of harmful microorganisms into the human body**[8]**. Therefore, monitoring and controlling meat spoilage are crucial for both economic and public health considerations. Figure 2.1 shows a diagram representing a schematic interpretation of zoonic diseases.

Figure 2. 1*: The schematic representation of the movement of micro-organisms from animals to humans through direct, indirect, Vector-borne, Foodborne, and Waterborne****[95]****.*

Detecting hazardous compounds produced during meat spoilage is crucial for ensuring meat quality and reducing food safety risks**[9]**. As already noted, according to the World Health Organization (WHO), food contamination causes about 420,000 fatalities and 600 million illnesses annually, resulting in a cost of 33 million healthy life in a years**[3]**.

2.2 History of Gas Sensors

The initial catalytic combustion gas sensor emerged in the early 1920s and was subsequently introduced to the market in 1923. This specific gas sensor employed a single platinum wire heated to elevated temperatures, facilitating a stable reaction with analyte gases**[10]**. The operational method involved measuring the change in resistance caused by the temperature increase during gas sensing. A refined version of the catalytic combustion gas sensor, incorporating a palladium catalyst in bead form, was later introduced; however, its usage was primarily confined to specialised fields and relied on the expertise of professionals**[11]**. Efficient control and monitoring devices are crucial for swiftly identifying and managing contaminants within accepted standard, addressing concerns about environmental safety and pollutants**[12]**. Gas sensors, in addition to their role in environmental monitoring, find applications in food processing and storage companies. They monitor and detect volatile organic compounds (VOCs) released by spoiled food**[13]**.

In the 1960s, there was a substantial demand for cost-effective and highly sensitive domestic gas sensors, prompted by incidents of explosions involving liquefied petroleum (LP) gas, commonly used for heating and cooking in Japan**[14]**. In 1962, Seiyama et al. introduced the first semiconductor gas sensor**[15, 16]**. A few years later, in 1966, Taguchi suggested utilising semiconducting oxides as sensing materials for detecting flammable gases like LP gas**[17]**. The choice of these oxides was due to their noticeable increase in conductivity at elevated temperatures. Subsequently, in 1968, Taguchi and his colleagues successfully pioneered the commercial production of semiconductor gas sensors utilising tin oxide**[18]**.

Later, they successfully enhanced the sensitivity of these sensors by annealing the sensing material, thereby increasing its porosity and elevating the operating temperature**[19]**. Since then, numerous investigations have been conducted to discover novel methods for improving the sensitivity of commercial sensors and exploring new types of semiconducting oxide materials, aiming to deepen our understanding of their sensing mechanisms**[20]**. The development of additional sensors, such as oxygen and humidity sensors, has been spurred by the success of semiconductor gas sensors. For instance, an oxygen gas sensor, based on the research of Wagner and Kiukolla, was created utilising a stabilised zirconia electrolyte that measures the standard free energy of the formation of metal oxides or the activity of oxygen in molten metals. The original concept for this sensor draws from the findings of Kiukolla and Wagner**[21]**, who demonstrated the dependence of the electromotive force (EMF) of an electrochemical cell based on stabilised zirconia electrolyte on the oxygen partial pressure at high temperatures**[22]**.

Advances in sensor technology have played a crucial role since then, identifying and controlling environmental pollutants while ensuring adherence to regulations**[23]**. The enforcement of occupational health and safety standards is becoming mandatory in numerous countries, and this mandate is expected to have a positive impact on the demand for gas sensors. According to the Global gas sensors, detectors, and analyzers market report for 2013, the market size for gas sensors reached $1,782.1 million in 2013, with a projected Compound Annual Growth Rate (CAGR) of 5.1% until 2020**[24]**.

2.3 Types of Gas Sensors

A gas sensor functions as a device designed to detect the presence of volatile substances in the vapour phase within a specific volume, providing both qualitative and quantitative information about their concentration**[25]**. These sensors are categorised according to two primary criteria: (i) the type of sensing material, which includes optical absorption**[26]**, catalytic, thermo conductive**[27]**, solid electrolytic**[28]**, and Metal oxides**[29, 30]**; and (ii) the sensing mechanism, which further divides gas sensors into two groups. The first group involves variations in electrical parameters, while the second group encompasses diverse detection methods such as optical, catalytic, thermometric, photoacoustic, chemiluminescence, and gas chromatographic alterations**[25]**. This classification system facilitates a comprehensive understanding of the various approaches employed in gas sensors, emphasising the diversity of sensing materials and mechanisms to cater to different applications and environmental conditions**[31]**.

2.3.1 Electrochemical Gas Sensor

This gas sensor type comprises of electrochemical cells constructed with a minimum of two electrodes: a sensing electrode (working electrode) and a reference electrode, connected through a thin electrolyte layer. In the electrochemical sensors, gases can diffuse through a membrane to the working electrode, where either oxidation or reduction of the gases occurs**[32]**. Electrochemical gas sensors are commonly employed in restricted spaces and require very little electricity to operate. They are especially well adapted for the accurate and focused detection of O_2. The short functioning life (1-3 years) and relatively low ability of these sensors to detect gases that are not electrochemically active are two of their main disadvantages**[33]**.

Figure 2.2 shows a schematic diagram of an electrochemical gas sensor illustrating all the components.

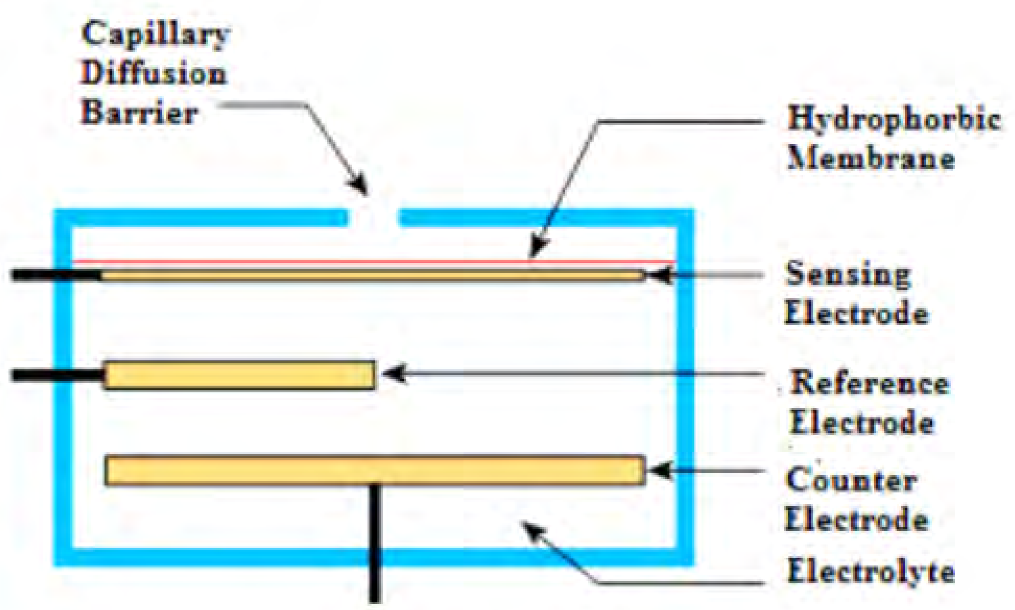

Figure 2. 2: A schematic diagram of an Electrochemical sensor[34].

2.3.2 Chemical Gas Sensor

In 1991, the International Union of Pure and Applied Chemistry (IUPAC) established the definition of chemical sensors. According to this official definition, a chemical sensor is a device that converts chemical information, encompassing the concentration of a particular sample component to an analysis of the total composition, into a signal that is analytically useful[35]. These sensors detect alterations in properties such as composition, pH, concentration. The foundation for quantitative investigations using chemical sensors lies in their efficient signal recognition, reception, and transduction[35].

2.3.3 Metal Oxide Semiconductor Gas Sensor

Various chemiresistive sensing materials, including metal-oxide semiconductors, exhibit desirable properties[36-38]. The utilisation of metal oxide semiconductors in gas sensors dates back to 1953 when Brattein and Bardeen noted changes in the electrical resistance of germanium (Ge) in the presence of surface impurities[39]. Seiyama et al. later observed a similar effect in ZnO, demonstrating increased adsorption and desorption processes on the ZnO surface at high temperatures (around 400 °C), enabling the detection of gaseous compounds**[40]**. The first chemiresistive gas sensor, based on SnO_2, was developed by Taguchi and Seiyama and commercially released in 1968 for detecting inflammable and reducing gases like liquefied propane (LP). Despite their early success, these metal-oxide sensors often encounter issues such as extended response times, cross-sensitivity, sensitivity to humidity, and inadequate long-term stability**[41]**. Chemiresistive MOS-based sensors exhibit alterations in resistance upon exposure to gases, with gas sensing mechanisms significantly influenced by factors such as surface nature, microstructure, and catalyst presence**[42]**. Operating temperature, film thickness, and oxide grain size play crucial roles in affecting MOS-based sensor responses.

2.4 Metal oxide Semiconductor

Over recent decades, the development of sensors has been diverse, employing different sensing materials and transduction stages. MOS-based gas sensors, featuring materials like SnO_2, TiO_2, and ZnO, are notable for their simplicity and cost-effectiveness, proving effective in detecting hazardous gases such as CO, CO_2, NH_3, N_2O, SO_2, O_3, LP gas, and CH_4**[43]**. Various synthesis methods, including chemical vapour deposition, sol-gel, and pulsed laser deposition, contribute to the creation of n-type metal oxides semiconductors for gas sensors**[43]**. However, metal oxide sensing materials have several limitations, including high operating temperatures, instability, and cross-sensitivity **[15, 44-49]**. The sensor's reaction is influenced by the operating temperature, especially when heating the sensitive layer is required to enable gas molecules to adhere to its surface. This leads to higher energy consumption and increased sensor costs **[13, 45]**. Furthermore, Metal oxide materials are susceptible to sensor poisoning during chemical reactions with target gases and may experience phase transitions at high temperatures, which can result in instability. These events can have a negative effect on the functioning of the sensor.

2.4.1 Tin Oxide (SnO_2) Properties

For over three decades, metal oxides have been extensively studied in gas-sensing research, with initial research predominantly centred around tin oxide. Tin oxide (SnO_2) possesses a tetragonal crystal structure with specific lattice parameters. In its intrinsic state, SnO_2 functions as an n-type semiconductor with a wide bandgap (Eg of ~3.4 eV) and is naturally oriented along (100) and (110) planes**[50]**. The (110) plane is thermodynamically the most stable due to the bridging of oxygen ions, but its stability can be altered through processes like high-temperature heating or high-energy particle bombardment**[51]**. SnO_2 has emerged as a favored material in gas-sensing research and commercial gas sensors among semiconducting metal oxides. Their advantages include affordability, high sensitivity to various gases, and potential miniaturisation for integration into micromachined substrates.

Despite their popularity, pure SnO_2 sensors often lack selectivity, detecting a range of gases instead of a specific one. To address this issue, nanocomposites, formed by incorporating metal or metal oxide additives, are utilised to induce electronic and chemical sensitisation. While the addition of dopants has shown improvements in sensitivity and recovery times, many additive modified SnO_2 gas sensors still operate at relatively high temperatures. Further research is needed to explore appropriate additive materials that can lower the operating temperatures of SnO_2 gas sensors**[52]**.

2.4.2 Titanium Dioxide (TiO_2) Properties

Titanium dioxide, or TiO_2, has gained significant prominence in the realm of surface science, particularly with the rutile(110) surface emerging as a pivotal model system in the study of metal oxides**[53]**. This heightened interest can be attributed to various compelling factors. Firstly, TiO_2 plays a crucial role in numerous essential technological applications, making a more in-depth comprehension of the fundamental aspects of TiO_2 surfaces and interfaces highly valuable**[54]**. The versatile applications of titanium dioxide include its utilisation in heterogeneous catalysis, functioning as a photocatalyst, and contributing to the production of hydrogen and electric energy in solar cells. Additionally, TiO_2 serves a pivotal role in gas sensing technologies**[55]**. The exploration and understanding of TiO_2 surfaces, particularly the rutile(110) surface, holds the potential to positively impact a wide array of technological advancements.

2.4.3 Zinc Oxide (ZnO) Propterties

Zinc oxide (ZnO), has a direct band gap of 3.37 eV and the high excitation of binding energy required for effective UV emission, has been thoroughly studied for a variety of applications, gas sensing being one of them**[56]**. Zinc oxide was previously unknown as a sensor material until the development of contemporary nanotechnology, which made it a most intriguing study topic**[57]**. In the chemical description of ZnO, the lattice can be defined as two interconnected hexagonal close-packed Zn and O lattices that are set up so that each Zn^{+2} ion is coordinated by four O^{-2} ions in a tetrahedral arrangement, and similarly, each O^{-2} ion is coordinated by four Zn^{+2} ions in the same way as shown in figure 2.3**[57, 58]**.The structure is Hexagonal closest packed with the lattice parameters a=b=3.2 Å, c=5.22 Å and angles β=90°=α and ɣ=120°**[59]**.

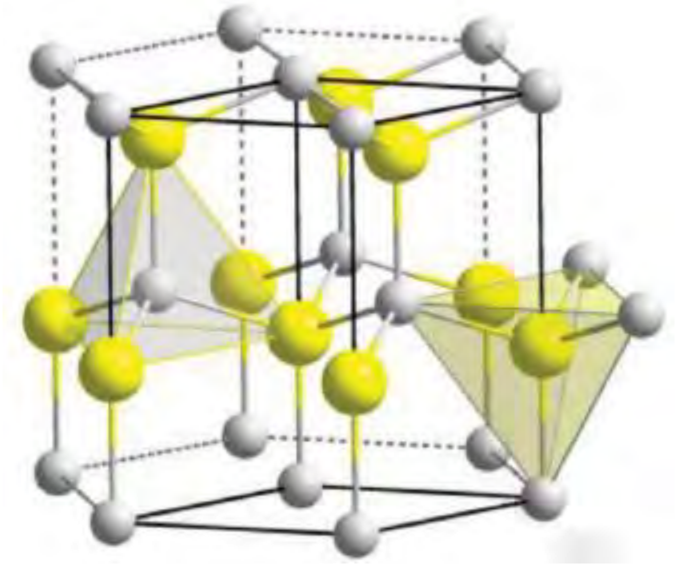

Figure 2. 3**: The Hexagonal closest packed (HCP) structure of ZnO**[59].

The sp3 hybridised bonds have roughly equal amounts of ionic and covalent properties. ZnO can generate zinc blende lattice films with the same ionic coordination types under growth conditions or employing cubic lattice substrates**[60]**. ZnO is an n-type semiconductor, and this material can be created using a wide range of techniques to different nanostructure morphologies**[61]**. This nanostructure can be created in a range, such as nanoparticles, nanowires, and other distinct structures with varied forms, utilising a number of different ways. The fabricated ZnO nanostructure has a number of surface modification which alter the surface layers, material's mechanical and functional characteristics. Doping improves the sensitivity by adding more sensitive material, and light activation can result in room temperature gas sensing**[62, 63]**. Due to its exceptional optical characteristics and relatively low production cost, zinc oxide has been studied for gas sensing applications**[63]**.

Fabrication of ZnO large-scale single crystals, epitaxial structures, thin and thick film structures, nanostructures, and nanoparticles can all be created from ZnO throughout its growth process**[64]**. As broad as the reported structures and their applications are the fabrication techniques**[65]**. The methods are often selected based on their typical inherent potentials and constraints to create a specific sort of structure, with some studies pushing the conventional potentials of growth to produce unconventional forms in the hydrothermal process, where crystal formation takes place in a water-based solution with a temperature gradient and high pressure**[66]**. When compared to ambient pressure, high pressure is required for the dissolution of the raw materials for crystals at a lower temperature (500 °C)**[66]**. Due to their higher specific surface area and greater length-to-diameter ratio, ZnO materials are regarded as being the most viable candidate among them for high-sensitivity gas sensors**[67]**. Additionally, latest findings on metal oxides studies have shown that noble metal components including Ag, Pt, Au and Pd can be used to decorate the surface of ZnO**[68-71]**.

2.5 Gas Sensing Parameters

2.5.1 Gas response

A gas sensor's response to a gas analyte is typically calculated as the ratio of resistance changes on the sensor's surface before and after exposure. It is mathematically stated by several study groups in various ways, as indicated in the Equations below.

$$R = \frac{R_g}{R_a} \qquad \text{Eq 2.1}\textbf{[72]}$$

$$R = \frac{R_g - R_a}{R_a} = \frac{\Delta R}{R_a} \qquad \text{Eq 2.2}\textbf{[73]}$$

$$R = \frac{R_g - R_a}{R_a} \times 100 = \frac{\Delta R}{R_a} \times 100$$ Eq 2.3**[74]**

$$R = \frac{I_0 - I_g}{I_g} = \frac{\Delta I}{I_g}$$ Eq 2.4**[75]**

where Ra is the sensor resistance in the presence of ambient dry air and Rg is the sensor resistance in the presence of the target gas. I_0 is the reference value (baseline) of the ZnO nanomaterials in ambient dry air and I_g is the current of the ZnO nanomaterials in the presence of the target gas**[76]**.

2.5.2 Response time of the Sensor

Response time is the amount of time a gas sensor needs to react to a target gas before reaching a stable end value at a certain percentage level (either often taken as 90% in many reports or typically indicated as T90)**[77]**. The detecting abilities of the sensor are also improved with a decreased reaction time. For target gas concentrations that are high, result in the response time being fast. Because they could need a longer response time, dangerous gases at low concentrations should be monitored carefully**[78]**. Response times for ZnO-based gas sensors are typically in the range of a minute or less**[79]**.

2.5.3 Recovery time of the Sensor

Recovery time is the amount of time needed for the sensor to return to 90% of the initial baseline when the target gas is removed and the sensor is later cleaned with dry air**[79]**. A good sensor application should have a low sensor recovery time to allow for repeated use of the sensor**[40]**. The observation of this behavior is represented in figure 2.4.

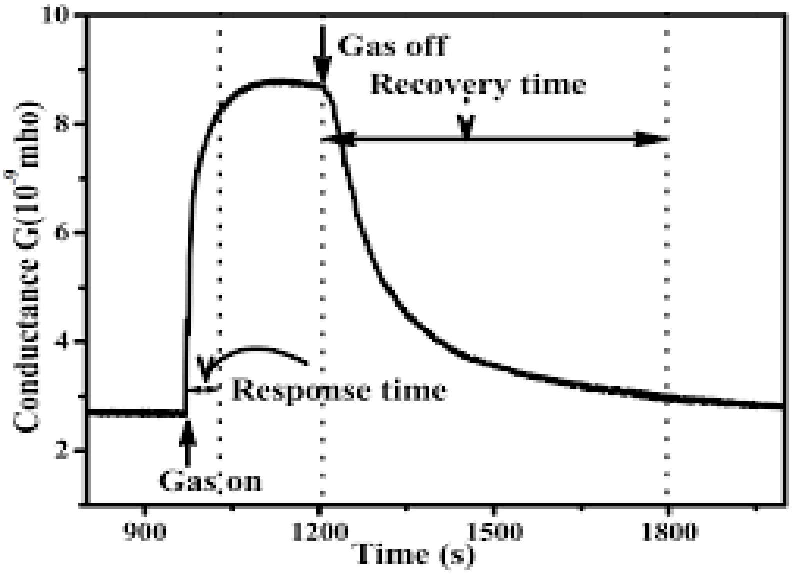

***Figure 2. 4**: Schematic plot of response and recovery time for chemiresistive gas sensor.*

2.5.4 Selectivity of the Sensor

Selectivity is the preferred chemiresistive sensing for a certain gas in the presence of another gas under comparable working circumstances**[80]**. ZnO-based nano sensors' selectivity may be described by.

$$\text{Selectivity} = \frac{\text{Sensitivity of the sensor towards interface gas } S_i}{\text{Sensitivity of the sensor towards target gas } S_g} \qquad \text{Eq 2.5}$$ **[80].**

2.5.5 Detection limit of the Sensor

The sensor should be able to detect gases at even extremely low concentrations for high-performance sensor applications. Lower detection limit refers to the lowest concentration of analyte gas that a sensor can detect while functioning**[73]**. The lowest detection limit of NO_2 gas for ZnO nanorod-based gas sensors has been reported to be 50 ppb at 300 °C**[73]**, and 100 ppb at 250 °C**[75]**.

2.5.6 Recyclability and Stability of the Sensor

The capacity of the sensor material to consistently maintain its sensing capabilities, even over extended periods, is referred to as stability**[80]**. When operating to a steady state, the ZnO sensor has a relatively strong response that gradually decreases over time owing to interface change**[80]**.

2.5.7 Other Parameters for the Sensor

A gas sensor's performance can also be evaluated using a number of other crucial factors. The detection limit is the minimum concentration of the target gas that a gas sensor can identify**[24]**. In the industrial and environmental monitoring scenarios, achieving a detection limit at the parts per million (ppm) level is typically preferable**[24]**. The working temperature aligns with the optimal temperature for the sensor to attain maximum sensitivity to the target gas. The life cycle denotes the duration during which the sensor can consistently operate**[81]**.

Figure 2.5 displays dynamic gas sensor response as an example of various Pt-loading amounts and pure mesoporous WO_3 toward various CO concentrations (100-500 ppm) at 125 °C, 57%RH. In comparison to previous WO_3/Pt-n sensors (n = 0, 0.2, and 1.0), the response of the WO_3/Pt-0.5 sensor rose rapidly with an increase in CO concentration from 10 1 at 100 ppm to 20 1.3 at 500 ppm. Additionally, each sensor exhibits a strong linearity connection link CO concentrations and the sensory response on a log-log plot (Figure 2.5 B), qualifying them for the quantitative measurement and detection of CO in real-world applications**[82]**.

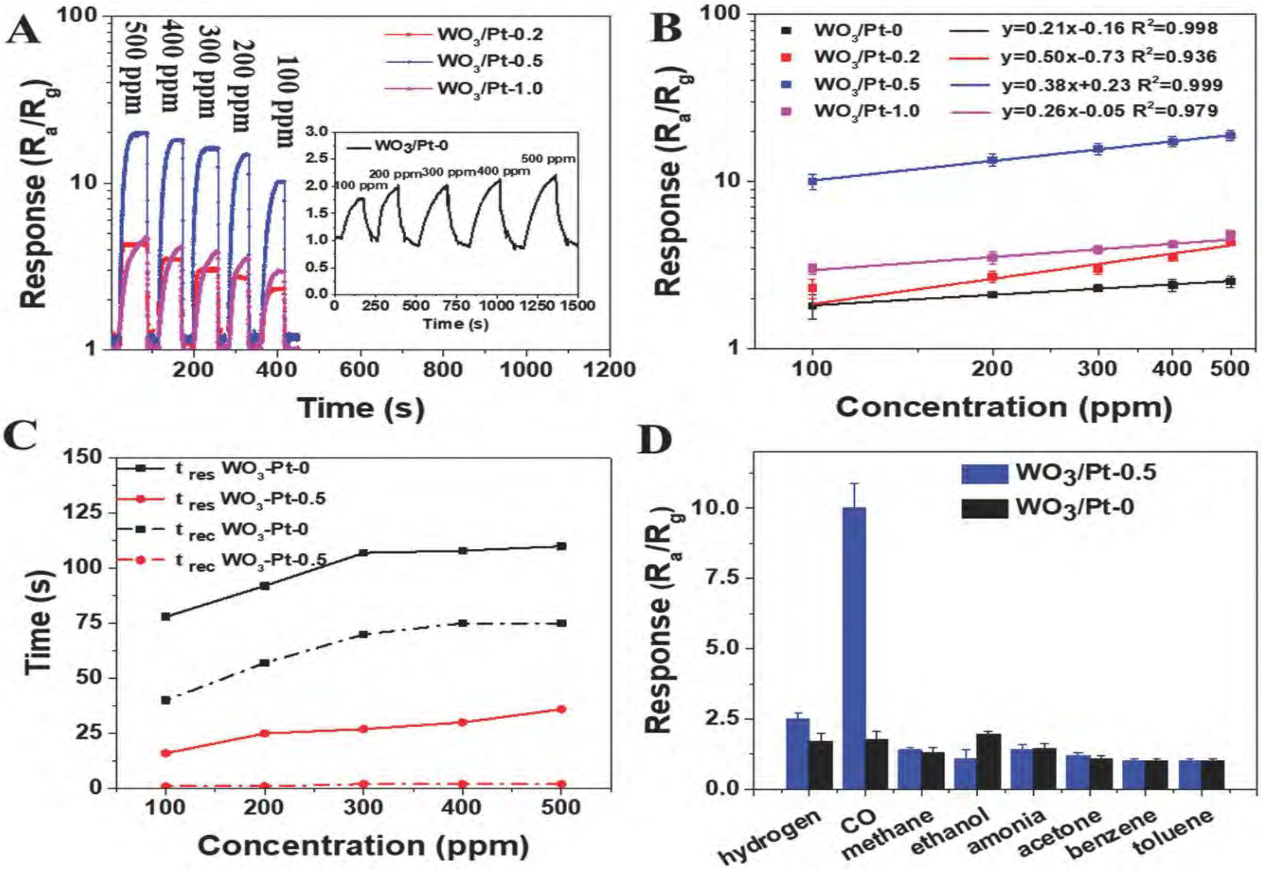

***Figure 2. 5**: The obtained mesoporous WO_3/Pt-n (n = 0, 0.2, 0.5, 1.0) showed a dynamic response-recovery characteristic curve when exposed to CO at different concentrations (100, 200, 300, 400, and 500 ppm) at 125 °C, 57%RH; B) Relationships between CO concentration and the response of the obtained mesoporous WO_3/Pt-n (n = 0, 0.2, 0.5, 1.0) in a log–log plot; C) The response and recovery time for the WO_3/Pt-0.5 and WO3/Pt-0 toward CO at different concentrations (100, 200, 300, 400, and 500 ppm) at 125 °C, 57%RH; D) The gas response of WO_3/Pt-0.5 and WO_3/Pt-0 toward various gases (hydrogen, CO, methane, ethanol, ammonia, acetone, benzene, and toluene) at an amount of 100 ppm at 125 °C, 55%–60%RH* **[82]**.

2.6 General Gas Sensing Mechanism

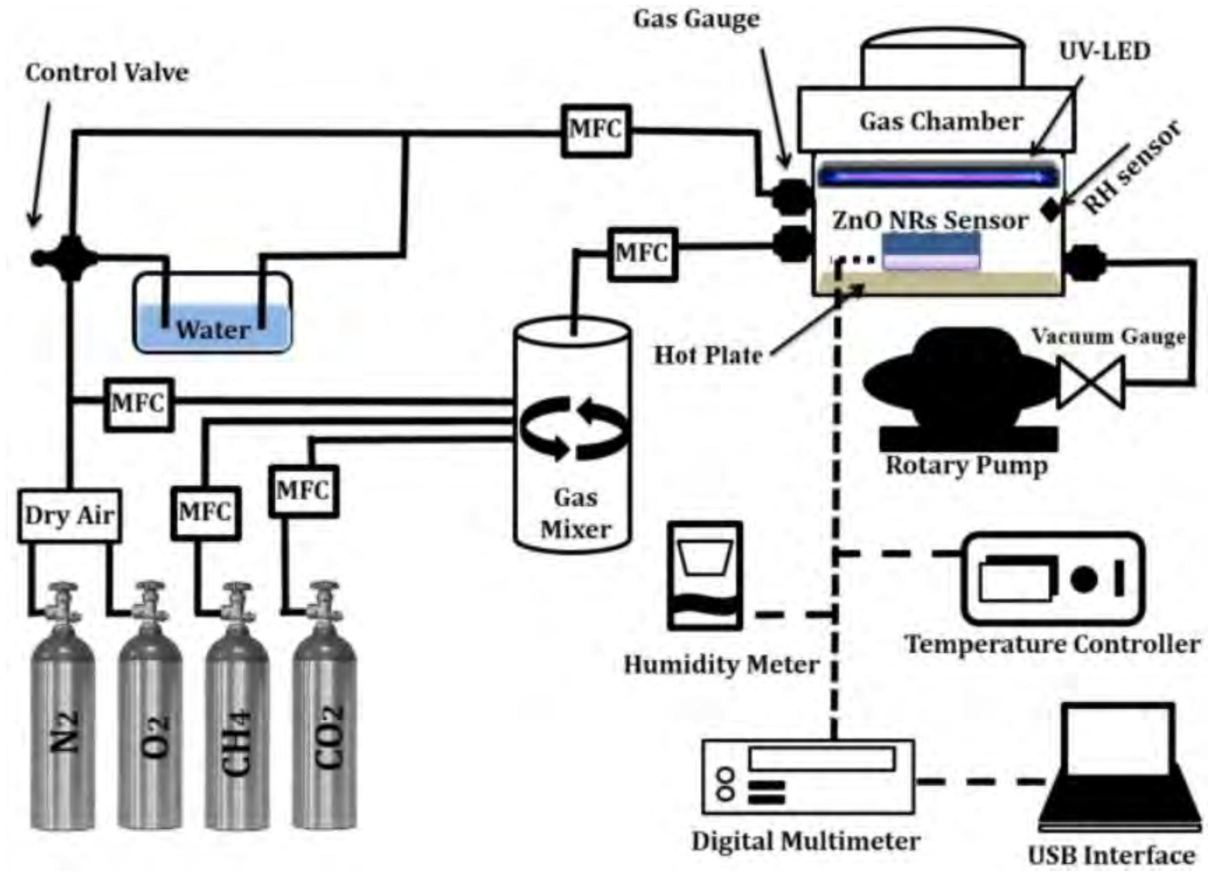

Figure 2. 6*: Experimental gas sensing Setup***[83]**.

According to the gas sensing literature, oxygen vacancies primarily affect sensing effectiveness by providing more coordinately unsaturated metal atoms, which increase the concentration of the level of surface-adsorbed oxygen, this changes the baseline resistance**[84]**. The agglomeration of nanoparticles in metal oxides causes pores to form, which facilitates the adsorption and desorption of gas molecules. Defects also appear at the oxide nanoparticle interfaces, forming heterojunctions that speed up the transfer of electrons between particles and result in a significantly faster response to the sensor.**[85]**.

It is generally known that surface area and porosity play a significant role in the gas-sensing property**[86]**. An electron depletion layer will then form on the surface of oxides as a result of the oxygen molecules being chemisorbed onto the surface of nanograins and converting into oxygen species (O_2, O, or O_2^-) by removing electrons from the conduction band**[87]**. The chemisorbed oxygen species will interact with the reducing gases and be drawn away from the surface of the oxides if the sensor is exposed to an environment that contains reducing gases**[88]**. As the potential barriers drop and the trapped electrons return to the conduction band, the sensor resistance will be reduced**[88, 89]**. An oxidizing gas will flow into the tube walls through interspaces and chemisorb on the surface of the nanograins when the sensor is exposed to it, further trapping electrons from the conduction band**[90]**. As a result, the potential barrier will rise, causing the sensor resistance to rise**[90]**. The sensor response, or change in sensor resistance, is mostly determined by the modification of potential barriers between neighboring nanograins in the sensing process**[44]**. The observation of parameters where this behavior takes place is shown in figure 2.6.

The target gas molecule and adsorbed oxygen species have better surface contacts when noble metal elements like gold (Au), platinum (Pt), and palladium (Pd) are decorated onto the surface of Flavin-containing mono-oxygenases (FMOs), this improves sensing performance.**[91]**. Moreover, different studies have also been devoted to improving the gas sensing properties of ZnO based sensors through the development of suitable functionalisation of noble metals and heterostructures **[92]**. Many research investigations have suggested that Pd is a viable addition for improving the sensing capabilities of ZnO nanostructures**[93]**. When ZnO is doped with Pd, its conduction band electrons move to Pd due to work function**[93]**. Pd is a highly effective oxygen dissociation catalyst, it catalytically promotes oxygen dissociation forming O^{-2} and O^{-} which spread over the entire surface, while extracting electrons from ZnO and creating the depletion region**[94, 95]**. As a result, an increase in the number of chemisorbed oxygen ions on the surface leads to more reaction with the target gas and therefore higher device sensitivities**[96]**.

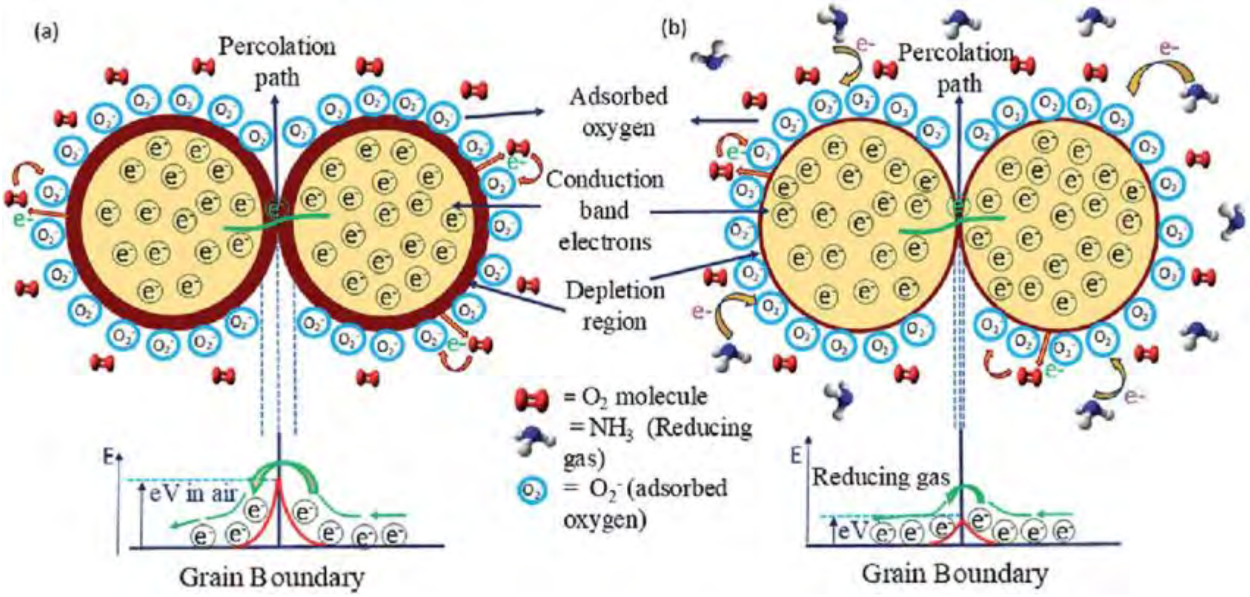

Figure 2. 7*: Schematic representation of the sensing technique for detecting NH 3, (a) before and (b) after ammonia exposure***[97]***.*

The detecting anomalies in figure 2.7 (a) and (b) sensors were most likely caused by a drop in the concentration of electrons on the ZnO surface. ZnO first absorbs oxygen atoms from the surrounding atmosphere**[98]**. The oxygen that has been adsorbed then removes electrons from the ZnO conduction band, changes into a single or double oxygen ion, and is ion adsorbed on the ZnO surface**[99]**. This resulted in a drop in electron concentration and a rise in surface resistance as a result. The following equations are used to describe this mechanism**[100]**.

$$O_2 \text{ (gas)} \leftrightarrow O_2 \text{ (absorbed)} \qquad (2.6)$$

$$\text{O2(absorbed)} + e^- \leftrightarrow O_2^- \text{ (<100 °C),} \qquad (2.7)$$

$$O_2^- + e^- \leftrightarrow 2O^- \text{ (100 - 300 °C),} \qquad (2.8)$$

$$\text{And } O^- + e^- \leftrightarrow O^{2-} \text{ (>300 °C)} \qquad (2.9)$$

The trapped electrons are released back into the conduction band when hydrogen or any other reduction gas reacts with the ion adsorbed material. As a result, there are more electrons present, which lowers resistance**[61]**.

2.7 References

1. Mercier, S., et al., *Time–temperature management along the food cold chain: A review of recent developments.* Comprehensive Reviews in Food Science and Food Safety, 2017. **16**(4): p. 647-667.
2. Januškevičienė, G., G. Zaborskienė, and A. Kabašinskienė, *Evaluation of meat physical, chemical and technological quality.* Kuriame Lietuvosateitj. Europos Sajunga, Germany. Pp1-37, 2012.
3. Joshi, N., G. Pransu, and C. Adam Conte-Junior, *Critical review and recent advances of 2D materials-Based gas sensors for food spoilage detection.* Critical Reviews in Food Science and Nutrition, 2022: p. 1-24.
4. Prabhakar, P.K., et al., *A comprehensive review on freshness of fish and assessment: Analytical methods and recent innovations.* Food research international, 2020. **133**: p. 109157.
5. Mackie, R.I., P.G. Stroot, and V.H. Varel, *Biochemical identification and biological origin of key odor components in livestock waste.* Journal of Animal Science, 1998. **76**(5): p. 1331-1342.
6. Sofos, J., *Microbial growth and its control in meat, poultry and fish.* Quality attributes and their measurement in meat, poultry and fish products, 1994: p. 359-403.
7. Rawat, S., *Food Spoilage: Microorganisms and their prevention.* Asian journal of plant science and Research, 2015. **5**(4): p. 47-56.
8. Das, A.K., et al., *Hazards and safety issues of meat and meat products*, in *Food safety and human health*. 2019, Elsevier. p. 145-168.
9. Soladoye, O., et al., *Protein oxidation in processed meat: Mechanisms and potential implications on human health.* Comprehensive Reviews in Food Science and Food Safety, 2015. **14**(2): p. 106-122.
10. Han, C.-H., et al., *Catalytic combustion type hydrogen gas sensor using TiO2 and UV-LED.* Sensors and Actuators B: Chemical, 2007. **125**(1): p. 224-228.
11. Yamazoe, N., G. Sakai, and K. Shimanoe, *Oxide semiconductor gas sensors.* Catalysis Surveys from Asia, 2003. **7**: p. 63-75.
12. Yamazoe, N. and N. Miura, *Environmental gas sensing.* Sensors and Actuators B: Chemical, 1994. **20**(2-3): p. 95-102.
13. Capone, S., et al., *Solid state gas sensors: state of the art and future activities.* Journal of Optoelectronics and Advanced Materials, 2003. **5**(5): p. 1335-1348.
14. Sakamoto, J., et al., *Leakage-type-based analysis of accidents involving hydrogen fueling stations in Japan and USA.* International journal of hydrogen energy, 2016. **41**(46): p. 21564-21570.
15. Seiyama, T., et al., *A new detector for gaseous components using semiconductive thin films.* Analytical Chemistry, 1962. **34**(11): p. 1502-1503.

16. Seiyama, T. and S. Kagawa, *Study on a Detector for Gaseous Components Using Semiconductive Thin Films.* Analytical chemistry, 1966. **38**(8): p. 1069-1073.
17. Khunou, R., *Gas sensing properties of Ceo2 nanostructures.* 2020.
18. Miura, N. and N. Yamazoe, *Development of new chemical sensors based on low-temperature proton conductors.* Solid State Ionics, 1992. **53**: p. 975-982.
19. Lu, L., et al., *Effects of annealing conditions on the photoelectrochemical properties of dye-sensitized solar cells made with ZnO nanoparticles.* Solar Energy, 2010. **84**(5): p. 844-853.
20. Yamazoe, N., *New approaches for improving semiconductor gas sensors.* Sensors and actuators B: Chemical, 1991. **5**(1-4): p. 7-19.
21. Ono, K., T. Oishi, and J. Moriyama, *Measurements on galvanic cells involving solid-sulphide electrolytes.* Solid State Ionics, 1981. **3**: p. 555-558.
22. Zha, S., C. Xia, and G. Meng, *Calculation of the emf of solid oxide fuel cells.* Journal of applied Electrochemistry, 2001. **31**: p. 93-98.
23. Wilson, J.S., *Sensor technology handbook*. 2004: Elsevier.
24. Liu, X., et al., *A survey on gas sensing technology.* Sensors, 2012. **12**(7): p. 9635-9665.
25. Hulanicki, A., S. Glab, and F. Ingman, *Chemical sensors: definitions and classification.* Pure and applied chemistry, 1991. **63**(9): p. 1247-1250.
26. Yu, H. and T. Shiquan, *An optical fiber sensor probe using a PMMA/CPR coated bent optical fiber as a transducer for monitoring trace ammonia.* Journal of Sensor Technology, 2011. **2011**.
27. Grate, J.W. and E.T. Zellers, *The fractional free volume of the sorbed vapor in modeling the viscoelastic contribution to polymer-coated surface acoustic wave vapor sensor responses.* Analytical Chemistry, 2000. **72**(13): p. 2861-2868.
28. Hooker, S.A. *Nanotechnology advantages applied to gas sensor development*. in *The nanoparticles 2002 conference proceedings*. 2002. Business Communications Co., Inc.
29. Moretto, L.M. and K. Kalcher, *Environmental analysis by electrochemical sensors and biosensors*. Vol. 1. 2014: Springer.
30. Basu, S. and P.K. Basu, *Nanocrystalline metal oxides for methane sensors: role of noble metals.* Journal of Sensors, 2009. **2009**.
31. Zhang, R., et al., *Gas sensing based on metal-organic frameworks: Concepts, functions, and developments.* Journal of hazardous materials, 2022. **429**: p. 128321.
32. Fraden, J., *Handbook of modern sensors.* Physics, designs, 1997.
33. Korotcenkov, G., S.D. Han, and J.R. Stetter, *Review of electrochemical hydrogen sensors.* Chemical reviews, 2009. **109**(3): p. 1402-1433.
34. Velasco, G., J.P. Schnell, and M. Croset, *Thin solid state electrochemical gas sensors.* Sensors and Actuators, 1981. **2**: p. 371-384.

35. Bi, H. and X. Han, *Chemical sensors for environmental pollutant determination*, in *Chemical, gas, and biosensors for internet of things and related applications*. 2019, Elsevier. p. 147-160.
36. Kaur, G., et al., *Electrically conductive polymers and composites for biomedical applications.* Rsc Advances, 2015. **5**(47): p. 37553-37567.
37. Sun, Y.-F., et al., *Metal oxide nanostructures and their gas sensing properties: a review.* Sensors, 2012. **12**(3): p. 2610-2631.
38. Vander Wal, R., et al., *Metal-oxide nanostructure and gas-sensing performance.* Sensors and Actuators B: Chemical, 2009. **138**(1): p. 113-119.
39. Pearson, G. and W.H. Brattain, *History of semiconductor research.* Proceedings of the IRE, 1955. **43**(12): p. 1794-1806.
40. Kumar, R., et al., *Zinc oxide nanostructures for NO 2 gas–sensor applications: A review.* Nano-Micro Letters, 2015. **7**: p. 97-120.
41. Bochenkov, V. and G. Sergeev, *Sensitivity, selectivity, and stability of gas-sensitive metal-oxide nanostructures.* Metal oxide nanostructures and their applications, 2010. **3**: p. 31-52.
42. Krishna, K.G., et al., *Nanostructured metal oxide semiconductor-based gas sensors: A comprehensive review.* Sensors and Actuators A: Physical, 2022. **341**: p. 113578.
43. Gautam, Y.K., et al., *Nanostructured metal oxide semiconductor-based sensors for greenhouse gas detection: Progress and challenges.* Royal Society open science, 2021. **8**(3): p. 201324.
44. Wang, C., et al., *Metal oxide gas sensors: sensitivity and influencing factors.* sensors, 2010. **10**(3): p. 2088-2106.
45. Choi, K.J. and H.W. Jang, *One-dimensional oxide nanostructures as gas-sensing materials: review and issues.* Sensors, 2010. **10**(4): p. 4083-4099.
46. Mondal, B., et al., *ZnO–SnO2 based composite type gas sensor for selective hydrogen sensing.* Sensors and Actuators B: Chemical, 2014. **194**: p. 389-396.
47. Zhang, L., et al., *Facile synthesis of mesoporous ZnO/Co3O4 microspheres with enhanced gas-sensing for ethanol.* Sensors and Actuators B: Chemical, 2015. **221**: p. 1492-1498.
48. Brattain, W.H. and J. Bardeen, *Surface properties of germanium.* The Bell System Technical Journal, 1953. **32**(1): p. 1-41.
49. Shaver, P., *Activated tungsten oxide gas detectors.* Applied Physics Letters, 1967. **11**(8): p. 255-257.
50. McGinley, C., et al., *Pure and Sb-doped SnO 2 nanoparticles studied by photoelectron spectroscopy.* The European Physical Journal D-Atomic, Molecular, Optical and Plasma Physics, 2001. **16**: p. 225-228.

51. Nütz, T. and M. Haase, *Wet-chemical synthesis of doped nanoparticles: optical properties of oxygen-deficient and antimony-doped colloidal SnO2.* The Journal of Physical Chemistry B, 2000. **104**(35): p. 8430-8437.
52. Liangyuan, C., et al., *Synthesis of ZnO–SnO2 nanocomposites by microemulsion and sensing properties for NO2.* Sensors and Actuators B: Chemical, 2008. **134**(2): p. 360-366.
53. Limo, M.J., et al., *Interactions between metal oxides and biomolecules: from fundamental understanding to applications.* Chemical reviews, 2018. **118**(22): p. 11118-11193.
54. Zhao, Z., et al., *Structure, synthesis, and applications of TiO2 nanobelts.* Advanced materials, 2015. **27**(16): p. 2557-2582.
55. Ma, Y., et al., *Titanium dioxide-based nanomaterials for photocatalytic fuel generations.* Chemical reviews, 2014. **114**(19): p. 9987-10043.
56. Wang, Z.L., *Zinc oxide nanostructures: growth, properties and applications.* Journal of physics: condensed matter, 2004. **16**(25): p. R829.
57. Lee, C.-T., *Fabrication methods and luminescent properties of ZnO materials for light-emitting diodes.* Materials, 2010. **3**(4): p. 2218-2259.
58. Zamiri, R., et al., *Aqueous starch as a stabilizer in zinc oxide nanoparticle synthesis via laser ablation.* Journal of alloys and compounds, 2012. **516**: p. 41-48.
59. Cajzl, J., et al., *Creation of gold nanoparticles in ZnO by ion implantation–DFT and experimental studies.* Nanomaterials, 2020. **10**(12): p. 2392.
60. Morkoç, H. and Ü. Özgür, *Zinc oxide: fundamentals, materials and device technology*. 2008: John Wiley & Sons.
61. Nunes, D., et al., *Metal oxide nanostructures for sensor applications.* Semiconductor Science and Technology, 2019. **34**(4): p. 043001.
62. Shetti, N.P., et al., *ZnO-based nanostructured electrodes for electrochemical sensors and biosensors in biomedical applications.* Biosensors and Bioelectronics, 2019. **141**: p. 111417.
63. Theerthagiri, J., et al., *A review on ZnO nanostructured materials: energy, environmental and biological applications.* Nanotechnology, 2019. **30**(39): p. 392001.
64. Schmidt-Mende, L. and J.L. MacManus-Driscoll, *ZnO–nanostructures, defects, and devices.* Materials today, 2007. **10**(5): p. 40-48.
65. Hirt, L., et al., *Additive manufacturing of metal structures at the micrometer scale.* Advanced Materials, 2017. **29**(17): p. 1604211.
66. Sadat-Shojai, M., et al., *Synthesis methods for nanosized hydroxyapatite with diverse structures.* Acta biomaterialia, 2013. **9**(8): p. 7591-7621.
67. Barth, S., et al., *Synthesis and applications of one-dimensional semiconductors.* Progress in Materials Science, 2010. **55**(6): p. 563-627.

68. Jang, H.W., Y.R. Choi, and Y.H. Kim, *Novel metal oxide gas sensors for mobile devices.* Smart Sensors and Systems, 2015: p. 131-153.
69. Li, S., et al., *Sandwich-like TiO2@ ZnO-based noble metal (Ag, Au, Pt, or Pd) for better photo-oxidation performance: Synergistic effect between noble metal and metal oxide phases.* Applied Surface Science, 2018. **443**: p. 603-612.
70. Liu, H., J. Feng, and W. Jie, *A review of noble metal (Pd, Ag, Pt, Au)–zinc oxide nanocomposites: synthesis, structures and applications.* Journal of Materials Science: Materials in Electronics, 2017. **28**: p. 16585-16597.
71. Demille, T.B., et al., *Light-mediated growth of noble metal nanostructures (Au, Ag, Cu, Pt, Pd, Ru, Ir, Rh) from micro-and nanoscale ZnO tetrapodal backbones.* Frontiers in chemistry, 2018. **6**: p. 411.
72. Shi, L., et al., *Highly sensitive ZnO nanorod-and nanoprism-based NO2 gas sensors: size and shape control using a continuous hydrothermal pilot plant.* Langmuir, 2013. **29**(33): p. 10603-10609.
73. Öztürk, S., N. Kılınç, and Z.Z. Öztürk, *Fabrication of ZnO nanorods for NO2 sensor applications: effect of dimensions and electrode position.* Journal of Alloys and Compounds, 2013. **581**: p. 196-201.
74. Oh, E., et al., *High-performance NO2 gas sensor based on ZnO nanorod grown by ultrasonic irradiation.* Sensors and Actuators B: Chemical, 2009. **141**(1): p. 239-243.
75. Şahin, Y., et al., *Electrical conduction and NO2 gas sensing properties of ZnO nanorods.* Applied Surface Science, 2014. **303**: p. 90-96.
76. Sapkota, R., et al., *Thin Film Gas Sensors Based on Planetary Ball-Milled Zinc Oxide Nanoinks: Effect of Milling Parameters on Sensing Performance.* Applied Sciences, 2021. **11**(20): p. 9676.
77. Van Han, H., et al., *Single-crystal zinc oxide nanorods with nanovoids as highly sensitive NO2 nanosensors.* Materials Letters, 2013. **94**: p. 41-43.
78. Xu, J., et al., *Synthesis of hierarchical ZnO orientation-ordered film by chemical bath deposition and its gas sensing properties.* materials Letters, 2012. **81**: p. 145-147.
79. Lee, H.-U., et al., *ZnO nanobarbed fibers: fabrication, sensing NO2 gas, and their sensing mechanism.* Applied Physics Letters, 2011. **98**(19).
80. Chougule, M., S. Sen, and V. Patil, *Fabrication of nanostructured ZnO thin film sensor for NO2 monitoring.* Ceramics International, 2012. **38**(4): p. 2685-2692.
81. Zhu, L. and W. Zeng, *Room-temperature gas sensing of ZnO-based gas sensor: A review.* Sensors and Actuators A: Physical, 2017. **267**: p. 242-261.
82. Ma, J., et al., *Pt nanoparticles sensitized ordered mesoporous WO3 semiconductor: gas sensing performance and mechanism study.* Advanced Functional Materials, 2018. **28**(6): p. 1705268.

83. Kimiagar, S., et al., *High performance and low temperature coal mine gas sensor activated by UV-irradiation.* Scientific Reports, 2018. **8**(1): p. 16298.
84. Wang, X., et al., *Enhanced formaldehyde gas sensing performance of ternary CuBi2O4 oxides through oxygen vacancy manipulation and surface platinum decoration.* Sensors and Actuators B: Chemical, 2021. **344**: p. 130190.
85. Li, Z., et al., *Advances in designs and mechanisms of semiconducting metal oxide nanostructures for high-precision gas sensors operated at room temperature.* Materials Horizons, 2019. **6**(3): p. 470-506.
86. Yin, Y., et al., *Improved gas sensing properties of silver-functionalized ZnSnO 3 hollow nanocubes.* Inorganic Chemistry Frontiers, 2018. **5**(9): p. 2123-2131.
87. Kim, J.-H., et al., *Synthesis and selective sensing properties of rGO/metal-coloaded SnO 2 nanofibers.* Journal of Electronic Materials, 2017. **46**: p. 3531-3541.
88. Kohl, D., *Surface processes in the detection of reducing gases with SnO2-based devices.* Sensors and actuators, 1989. **18**(1): p. 71-113.
89. Moseley, P.T., *Solid state gas sensors.* Measurement Science and technology, 1997. **8**(3): p. 223.
90. Diao, K., et al., *Selectively enhanced sensing performance for oxidizing gases based on ZnO nanoparticle-loaded electrospun SnO 2 nanotube heterostructures.* RSC advances, 2016. **6**(34): p. 28419-28427.
91. Cho, S., et al., *Ethanol sensors based on ZnO nanotubes with controllable wall thickness via atomic layer deposition, an O2 plasma process and an annealing process.* Sensors and Actuators B: Chemical, 2012. **162**(1): p. 300-306.
92. Li, T., W. Zeng, and Z. Wang, *Quasi-one-dimensional metal-oxide-based heterostructural gas-sensing materials: a review.* Sensors and Actuators B: Chemical, 2015. **221**: p. 1570-1585.
93. Mhlongo, G.H., et al., *A highly responsive NH3 sensor based on Pd-loaded ZnO nanoparticles prepared via a chemical precipitation approach.* Scientific reports, 2019. **9**(1): p. 9881.
94. Polzonetti, G., et al., *The interface between aluminium and a rod-like organometallic Pd-containing polymer film investigated by XPS.* Journal of electron spectroscopy and related phenomena, 1997. **85**(1-2): p. 73-80.
95. Kim, H., et al., *Amorphous Pd-assisted H2 detection of ZnO nanorod gas sensor with enhanced sensitivity and stability.* Sensors and Actuators B: Chemical, 2018. **262**: p. 460-468.
96. Cao, P., et al., *Ethanol sensing behavior of Pd-nanoparticles decorated ZnO-nanorod based chemiresistive gas sensors.* Sensors and Actuators B: Chemical, 2019. **298**: p. 126850.

97. Deng, Y., *Sensing mechanism and evaluation criteria of semiconducting metal oxides gas sensors*, in *Semiconducting Metal Oxides for Gas Sensing*. 2023, Springer. p. 33-74.
98. Devan, R.S., et al., *One-dimensional metal-oxide nanostructures: recent developments in synthesis, characterization, and applications.* Advanced Functional Materials, 2012. **22**(16): p. 3326-3370.
99. Pimentel, A., et al., *Ultra-fast microwave synthesis of ZnO nanorods on cellulose substrates for UV sensor applications.* Materials, 2017. **10**(11): p. 1308.
100. Wetchakun, K., et al., *Semiconducting metal oxides as sensors for environmentally hazardous gases.* Sensors and Actuators B: Chemical, 2011. **160**(1): p. 580-591.

CHAPTER 3-CHARACTERISATION TECHNIQUE AND SYNTHESIS

3.1 INTRODUCTION

In order to get more insight on Zinc materials synthesized by hydrothermal various characterisation techniques such as x-ray diffraction (XRD), Raman spectroscopy, scanning electron microscope (SEM), X-ray Photoelectron spectroscopy (XPS), Energy Diffraction Spectroscopy (EDS), UV/vis Spectroscopy, and gas sensing system were used to characterize the manufactures material. This chapter briefly discusses all the characterization techniques.

3.2 X-Ray Diffraction (XRD)

Today, atomic spacing and crystal structures are studied using X-ray diffraction. The basis of X-ray diffraction is the interference of a crystalline sample with monochromatic X-rays. A cathode ray tube produces these X-rays, which are then collimated to concentrate them, filtered to produce monochromatic radiation, and directed toward the sample **[1]**. This is shown in figure 3.1 below.

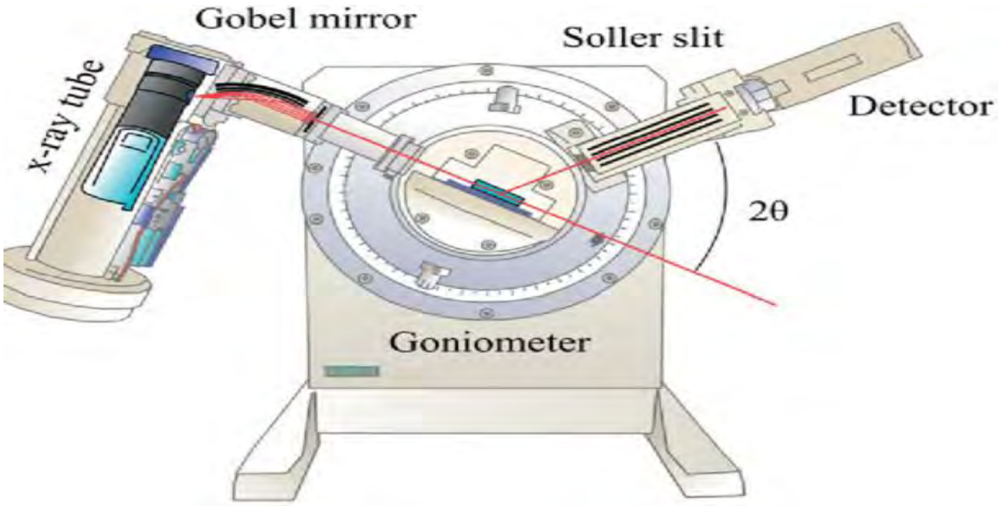

Figure 3. 1*: Schematic diagram of X-Ray Diffraction****[30]****.*

When the following criteria are met, the incident rays' interaction with the sample results in constructive interference (as well as a diffracted ray):

$$n\lambda = 2d_{(hkl)}\sin\theta$$ eq1**[2].**

where n is an integer, d is the interplanar spacing that causes the diffraction, θ is the diffraction angle in degrees, and λ is the wavelength of the X-rays in nm**[2].** The interaction between the material and the X-ray is represented in figure 3.2 below. The interaction is interpreted in Braggs equation on equation 1 above.

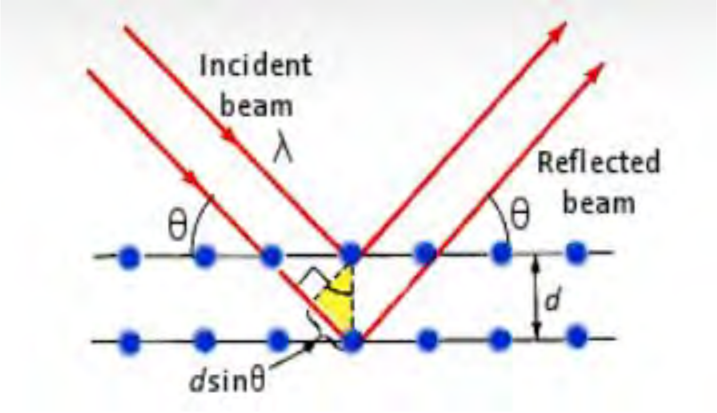

Figure 3. 2*: Schematic representation of the Bragg equation****[31]****.*

XRD analysis steps; In a combination of substances, each develops its pattern independently of the others, and every crystalline material yields a pattern that is always the same**[3]**. The identification process includes the following aspects of crystals: microstructure, quantitative resolution of chemical species, isomorphous substitutions, unknown crystalline materials, solids, crystalline phase, transition, and their quantitative proportion**[3, 4]**. By comparing the pattern to the Joint Committee on Powder Diffraction Standards library (JCPDS), X-ray diffraction patterns function similarly to fingerprints in identifying crystalline materials**[3]**. It is a widely used analytical approach in forensics, nanomaterials, catalysis, and geological materials because it generates separate patterns of components in mixes**[5]**.

3.2.1 Crystallite size measurement

The positions of the peaks in a diffraction profile and, to some extent, the relative intensities of these peaks determine the phase of x-ray diffraction. Another aspect of diffraction from material is the significance of considering how diffraction peaks are changed by the presence of various types of defects, such as small number of dislocations in crystals with dimensions of millimeters. Grain size smallness can alter the diffraction peaks has a width of 29 nm and be regarded as a different type of defect. Peak broadening is caused by small crystals. It is simple to determine the crystallite size as a function of peak location, peak width (defined as the full width at half maximal FWHM), and wavelength**[2]**.

$$\boldsymbol{D} = \frac{\mathbf{0.9}\boldsymbol{\lambda}}{\boldsymbol{\beta}\,\mathbf{cos}\,\boldsymbol{\theta}} \qquad \text{eq2}\textbf{[2]}$$

The Scherrer equation relates the full width at half maximum (FWHM) of a diffraction peak to the crystallite size, where D is the crystallite size, $\boldsymbol{\lambda}$ the wavelength of the X-ray radiation, β is the FWHM of the peak measured in μm and $\boldsymbol{\theta}$ is the Bragg angle measured in degrees**[2]**.

3.3 X-ray Photoelectron Spectroscopy (XPS)

The mid-1960s saw the invention of X-ray Photoelectron Spectroscopy (XPS) by Kai Siegbahn, XPS uses monoenergetic soft x-rays to irradiate a material in vacuum and measures the energy of the released electrons**[6, 7]**. Typically, x-rays of Mg Ka (1253.6 eV) or Al K~ (1486.6 eV) are used**[8]**. Within a solid, these photons have a restricted ability to penetrate 1–10 micrometers. Through their interactions with atoms in the surface area, the photoelectric effect releases electrons**[9]**. The overall setup of XPS system and plots is shown in figure 3.3 below.

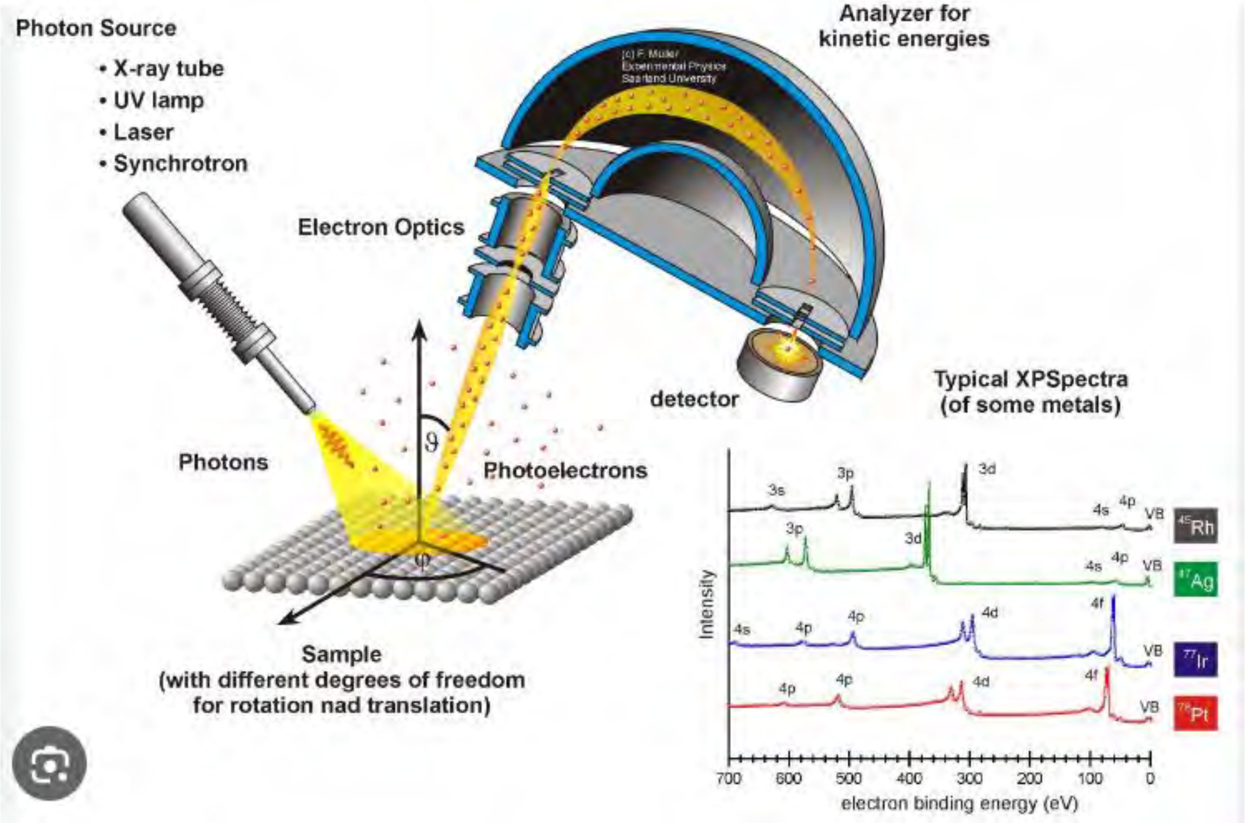

***Figure 3. 3**: Schematic drawing of a XPS setup with photon source, a sample manipulation with different linear and rotational degrees of freedom, electron optics, an energy dispersive analyzer and a detector. XP spectra (intensity vs. binding energy) are shown for four different metals**[32]**.*

This photoelectric escape depth varies from sample to sample and is dependent on the energy of the radiation, the kinetic energy of the ejected electrons, the crystallinity, and the density of the sample material**[8]**. The measured kinetic energy of the released electrons is obtained by:

$$KE = hv - BE - \phi$$

eq3**[8]**.

The chemical environment of an atom alters the binding energy (BE) of a photoelectron which results in a change in the measured kinetic energy (KE). The BE is related to the measured photoelectron KE by the simple equation; BE = hv - KE where hv is the photon (x-ray) energy. and ϕ is the flux. Plotting the quantity of observed electrons per energy interval against their kinetic energy yields the spectrum every element possesses a distinct specific spectrum. The estimated total of the peaks of each individual component makes up the spectrum of a combination of components**[10]**. XPS is a special surface-sensitive method for chemical analysis because the measured electrons come from the top few atomic layers due to the extremely tiny mean free path of electrons in solids**[11]**. Peak heights and peak areas can yield quantitative data, and precise measurements of peak locations and heights can frequently be used to identify chemical states**[11]**.

3.4 Raman Spectroscopy

Raman spectroscopy is a vibrational method, it uses high-energy photons and the inelastic scattering of light in the visible or near-infrared range of the material**[12]**. The wavelength of the laser source light is shared by most of the dispersed light, or Rayleigh scatter**[13]**. Elastic and inelastic scattering are the two different forms of light scattering. When the photon frequency remains constant or changes its wavelength, this is known as elastic scattering**[12]**. Raman spectroscopy uses inelastic scattering, which is the opposite. Information on molecular chemistry may be obtained by using the frequency shift**[14]**. The schematic diargram is shown in the figure3.4 below.

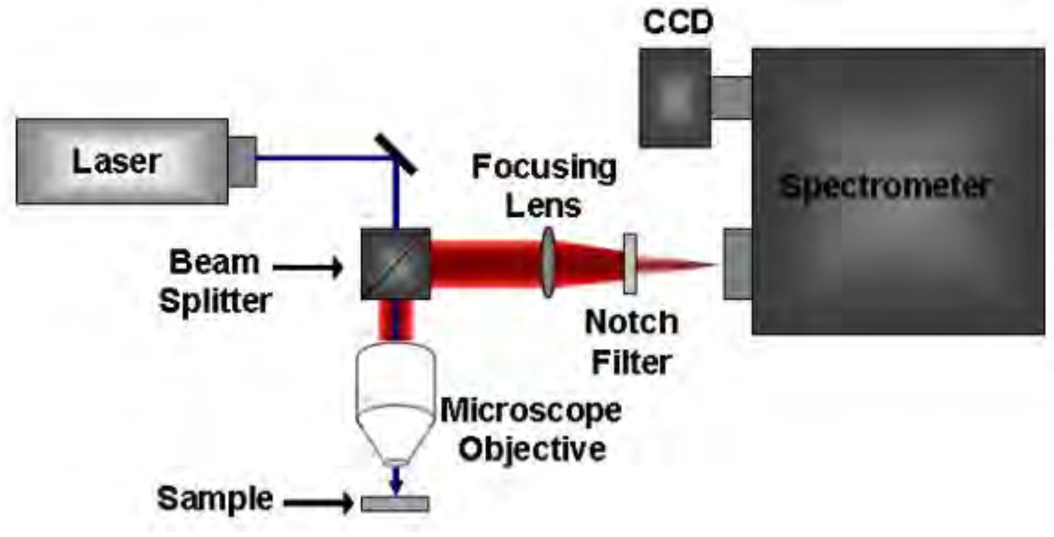

***Figure 3. 4**: Schematic diagram showing the different components of a Raman instrument**[33]**.*

When the resulting scattered light has a lower frequency than the initial photon, it is referred to as Stokes Raman scattering; when it has a higher frequency, it is referred to as anti-Stokes Raman scattering this is shown in figure 3.5**[15]**. When the bond is originally in the excited vibrational state, the photon obtain energy from the molecule's bond**[16]**. The basis of Raman is the measurement of the outgoing photon's energy shift, the chemical composition of the molecules causing the scattering determines the wavelength shift of the scattered light**[16, 17]**. The amount that the molecule polarization changes determine how intense the Raman scattering is**[17]**.

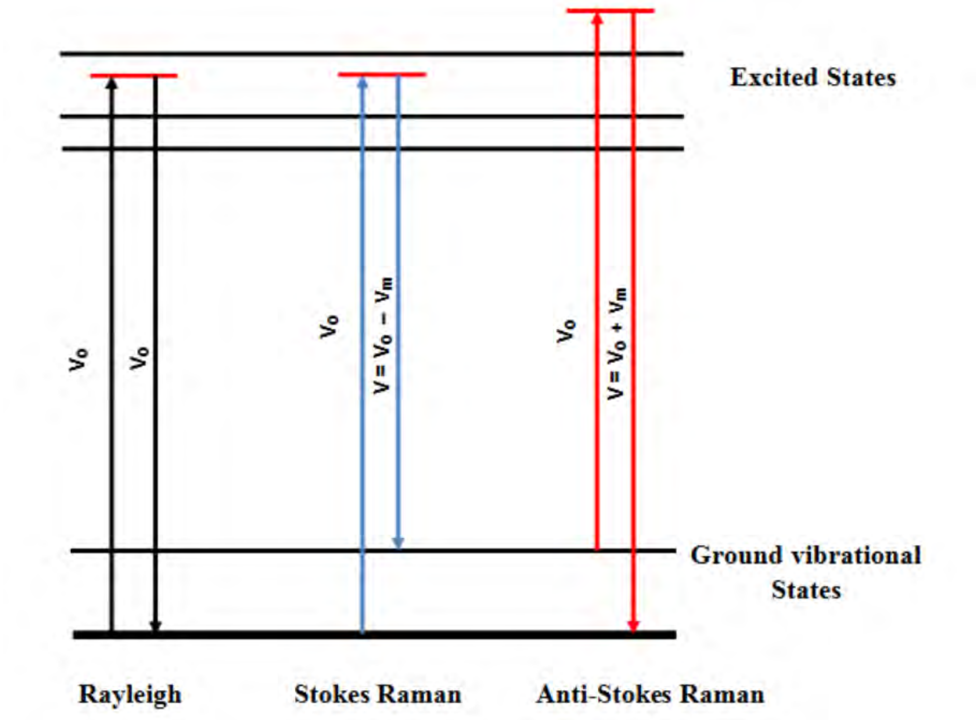

Figure 3. 5*: Three different forms of laser scattering****[34]****.*

The different vibration phonons are observed from the Raman spectra and are interpreted for understanding the molecular chemistry of the material. Phonons are A_1 and E_1 modes are polar and divide into transverse optical (A_1T and E_1T) and longitudinal-optical (A_1T and E_1T) phonons, respectively, while the E_2 mode is made up of two modes of low- and high-frequency phonons (E_2(low) and E_2(high)) which are Raman active**[18]**.

3.5 UV/VIS spectroscopy

UV-VIS spectroscopy involves the study of interaction of electromagnetic radiation with matter. The energy is either absorbed or emitted by matter in distinct amounts called quanta**[19]**. The fundamental idea behind ultraviolet- visible spectroscopy is the electronic transition that describes an electron's excitation from its ground state to its excited state. Spectrophotometer measurements need the utilisation of a restricted range of light wavelengths using monochromators and filters**[20]**. A filter is a device that transmits light at a specific wavelength while completely or partially absorbing light at other wavelengths**[21]**. The schematic diagram of the UV/vis is shown in figure 3.6 below.

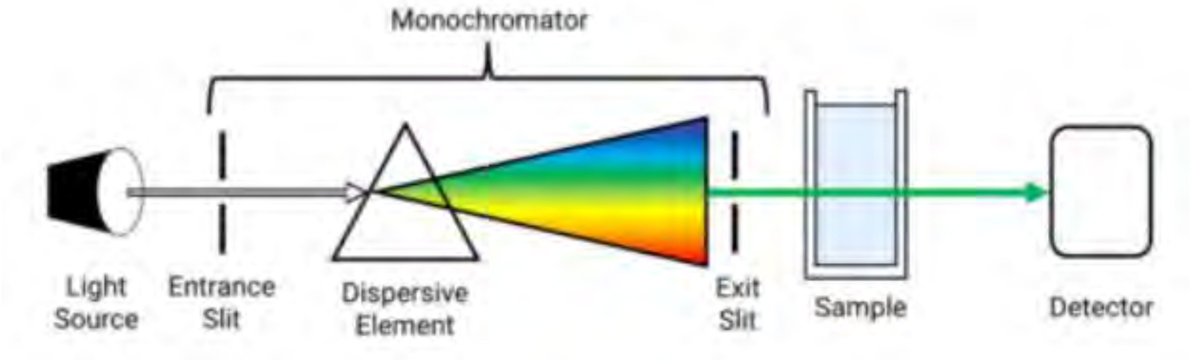

***Figure 3. 6**: A basic block diagram of the elements in a single beam UV-visible spectrometer**[35]**.*

The polychromatic light is transformed into the desired monochromatic light using a monochromator**[21]**. The detector's primary job is to convert the light source into an electrical signal**[21]**. UV/vis instrument has a detector that transform transmitted or reflected light from the sample into a signal used for measurement**[21]**. Apart from the wavelength, the other parameters of interest are absorbance (A), transmittance (%T), and reflectance (%R), as well as their variations over time**[19]**.

Using optical absorption spectra the band gap energy of amorphous semiconductors can be estimated.

$$(\alpha \cdot h\nu)^{1/\gamma} = B(h\nu - E_g) \qquad \text{eq3[22]}$$

where *h* is the Planck constant, ν is the photon's frequency, E_g is the band gap energy, and *B* is a constant. The γ factor depends on the nature of the electron transition and is equal to 1/2 or 2 for the direct and indirect transition band gaps, respectively. The measured reflectance spectra can be transformed to the corresponding absorption spectra by applying the Kubelka–Munk function (eq 4):

$$(\mathrm{F}(\mathrm{R}\infty)\cdot\mathrm{h}\nu)^{1/\gamma}=\mathrm{B}(\mathrm{h}\nu-\mathrm{E}g) \qquad \text{eq4}$$ **[23]**

where B is a constant, v is the frequency of the photon, E_g is the energy of the band gap, and h is the Planck constant. The factor is equal to 1/2 or 2, depending on the type of electron transfer, for the direct and indirect transition band gaps, respectively**[24]**.

3.6 Scanning Electron Microscopy (SEM) & Electron Diffraction Spectroscopy (EDS)

SEM has been applied in several fields around the globe, and is considered as a useful technique for analysing materials on the nanoscale to micrometer (μm) scale, both organic and inorganic**[25]**. With a high magnification of up to 300,000x and even 1000000 (in some contemporary versions), SEM can provide incredibly exact images of a wide variety of materials**[25]**. The apparatus has a variable pressure system that can accommodate any kind of sample, including ones that need little pretreatment or are moist. Analysing samples up to 200 mm in diameter and 80 mm in height is possible with this instrument**[26]**. A schematic diagram of a SEM system is shown in figure 3.7 below.

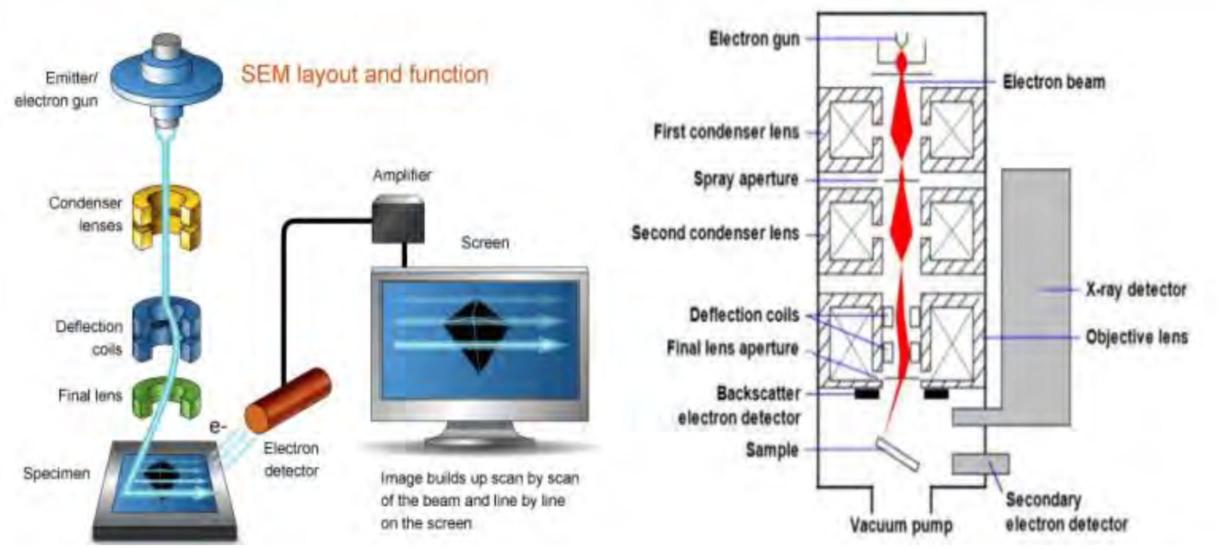

Figure 3. 7: *Schematic representation of SEM layout and function**[36]**.*

Together with SEM, energy dispersive X-ray spectroscopy (EDS) yields qualitative and semi-quantitative data. EDS is a method for analysing a sample's elemental composition that is used in combination with transmission electron microscopy (TEM) or scanning electron microscopy (SEM)**[27]**. When the high-energy electron beam interacts with the material, X-rays are produced**[27]**. The elements found in the sample are reflected in these X-rays. A crystal or solid-state detector disperses the energy of these X-rays, and the resultant spectrum gives details on the abundance and elemental composition of the sample**[27]**.

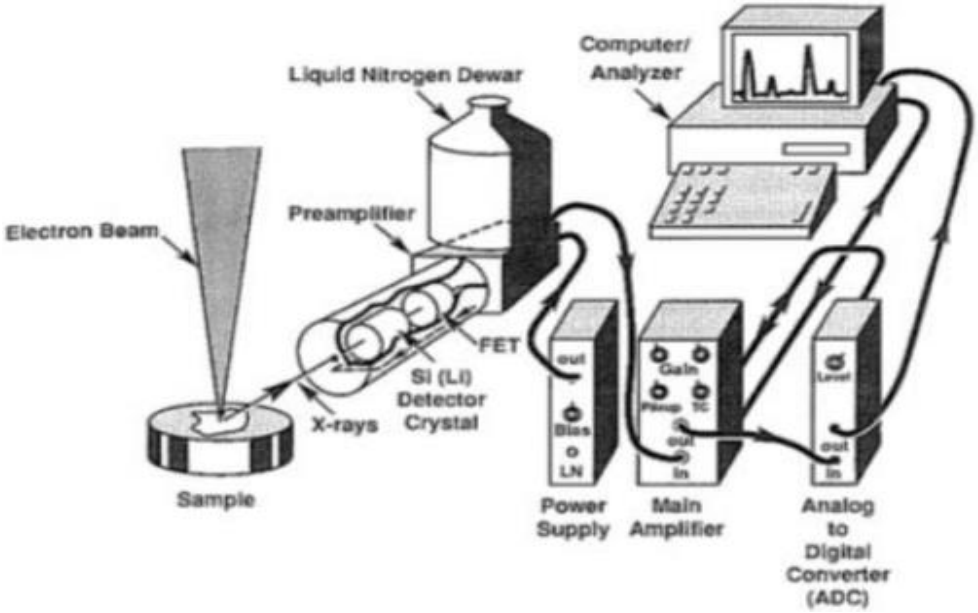

Figure 3. 8*: Schematic diagram of EDS machine functions****[37]****.*

Kilo-electron volts (keV) are units used to quantify the energy of X-rays released by the sample during its contact with the electron beam. The data acquired from EDS analysis is commonly shown as an X-ray spectrum. The X-ray intensity, expressed in counts, at each energy level**[28]**. The counts correspond to the quantity of X-rays that the EDS system was able to identify**[28]**.

3.7 Gas Sensing System

A gas detecting device is used to identify and track the presence of gases in various environments, including houses, public spaces, and underground mining sites. The environment and human health are both at risk from the potentially dangerous and flammable gases. These gas leaks are detected using gas sensing systems which have an alarm to warn users, allowing them time to get away and take the necessary safety precautions. Some models can also start an automatic shut-off. In the past, humans relied on their noses to detect gases. However, some gases are odourless in nature, while some leak at low concentration and can be harmful when inhaled over an extended period. As a result, before the invention of contemporary electronic sensors, several tragic occurrences and life-threatening situations happened. Gas detectors can be categorised based on how they work, including holographic, infrared, semiconductor, electrochemical, and ultrasonic**[29]**. The images of gas system and sensing chamber is shown in figure 3.9 below.

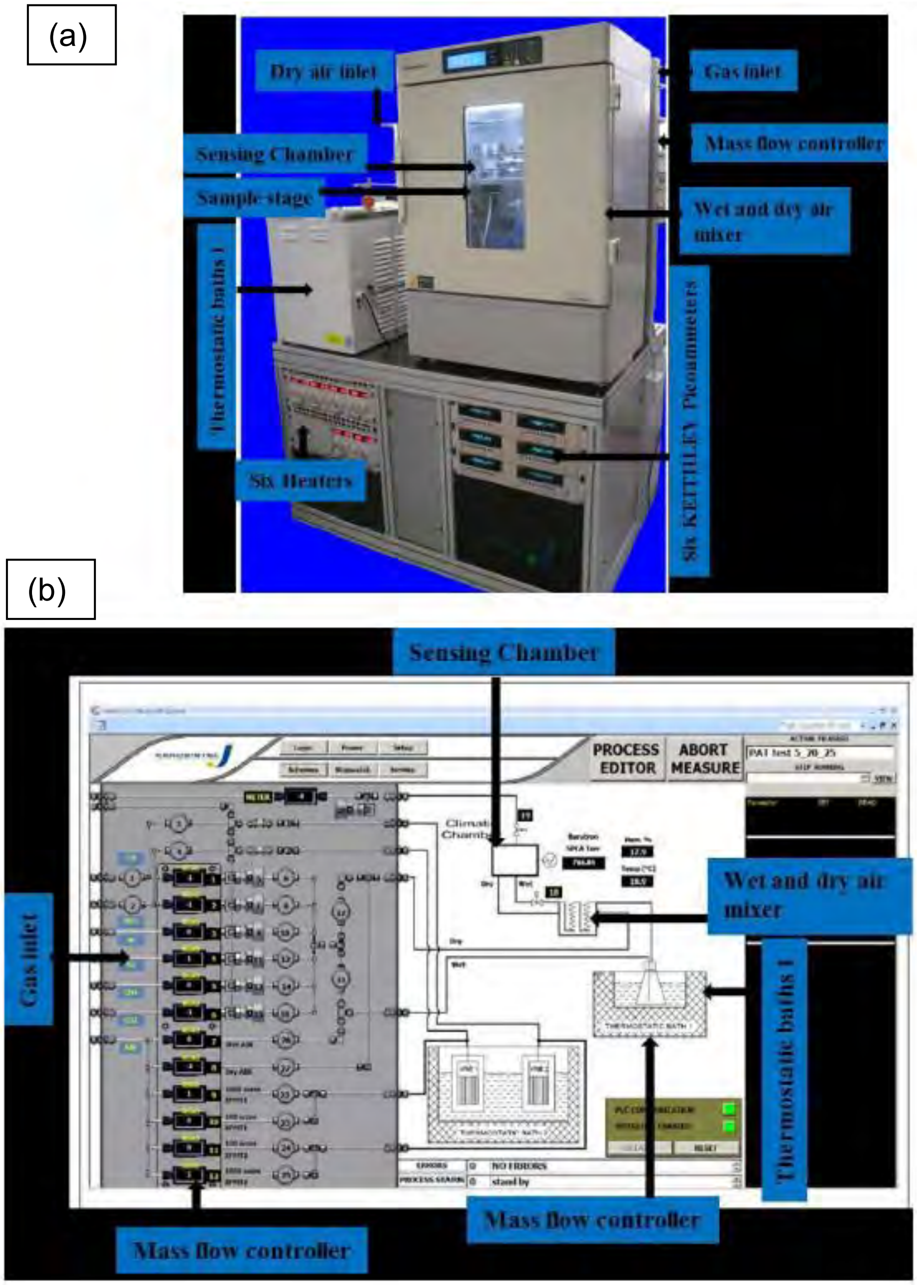

***Figure 3. 9**: (a) KENOSISTEC Gas sensing station and (b) main operating window of UHV and thin film**[29]**.*

The system is made up of a sensing chamber with sample stages, an air mixer, a dry air inlet that supplies dry air to the mixer, four distinct gas inlets, mass flow controllers that regulate the gas volume into the chamber, two thermostatic baths, one for supplying wet air into the mixer during measurements of humidity, and the other for measuring volatile gases, six KEITHLEY picoammeters for conductance measurements, and six heaters that provide voltage across the sample, gas inlet, and outlets, including a vent outlet**[29]**. In this project powder samples were synthesised for this sensing application.

3.8 SYNTHESIS METHODS

3.8.1 Pure ZnO

Zinc acetate dihydrate ($Zn(CH_3COO)_2 \cdot 2H_2O$), Sodium hydroxide (NaOH), Palladium chloride (PdCl2), Hydrochloric acid (HCl) were all analytical graded and were used as they are without any purification. Salt of 2.00 g Zinc acetate dihydrate was mixed with 4.00 g of Sodium hydroxide in 30 ml of distilled water. The solution was stirred in a magnetic stirrer under heating at 80 ^{o}C for 30 minutes. The initial pH was 11.37 but HCl was added to neutralize the solution, which led to a final pH of 7.04. The solution was transferred to a stainless-steel autoclave reactor and put in an oven at 150 ^{o}C for 1 hour. The solution was cooled to room temperature, washed with distilled water in a centrifuge and dried at 60 ^{o}C. It was then annealed at 550 ^{o}C for 1 hour.

3.8.2 Pd doped ZnO Nanoparticles

2.00 g Zinc acetate dihydrate was mixed with 4.00 g of Sodium hydroxide in a 30 ml of distilled water. From the percentage of the doping amount number of moles was calculated using the stoichiometric ratio. Then the calculated mass of PdCl2 was added to the solutions: 0.017733 g, 0.02660 g, 0.04433 g and 0.06207 g to make 0.2% Pd-ZnO, 0.3% Pd-ZnO, 0.5% Pd-ZnO and 0.7% Pd-ZnO respectively. All samples were dried at 60 ^{o}C and annealed at 550 ^{o}C.

3.9 References

1. Bunaciu, A.A., E.G. UdriŞTioiu, and H.Y. Aboul-Enein, *X-ray diffraction: instrumentation and applications.* Critical reviews in analytical chemistry, 2015. **45**(4): p. 289-299.
2. Monshi, A., M.R. Foroughi, and M.R. Monshi, *Modified Scherrer equation to estimate more accurately nano-crystallite size using XRD.* World journal of nano science and engineering, 2012. **2**(3): p. 154-160.
3. Khan, H., et al., *Experimental methods in chemical engineering: X-ray diffraction spectroscopy—XRD.* The Canadian journal of chemical engineering, 2020. **98**(6): p. 1255-1266.
4. Chauhan, A. and P. Chauhan, *Powder XRD technique and its applications in science and technology.* J Anal Bioanal Tech, 2014. **5**(5): p. 1-5.
5. Das, R., E. Ali, and S.B. Abd Hamid, *CURRENT APPLICATIONS OF X-RAY POWDER DIFFRACTION-A REVIEW.* Reviews on Advanced Materials Science, 2014. **38**(2).
6. Watts, J.F. and J. Wolstenholme, *An introduction to surface analysis by XPS and AES*. 2019: John Wiley & Sons.
7. Haasch, R.T., *X-ray photoelectron spectroscopy (XPS) and auger electron spectroscopy (AES)*, in *Practical Materials Characterization*. 2014, Springer. p. 93-132.
8. Koppelman, M.H., *sampling depth. X-rays generated by targets such as aluminum (Ka, o, hu= 1486.6 eV) or magnesium (Ka, a2, hu= 1253.6 eV) have sufficient energy to.* Advanced Chemical Methods for Soil and Clay Minerals Research: Proceedings of the NATO Advanced Study Institute held at the University of Illinois, July 23–August 4, 1979, 2012. **63**: p. 205.
9. Kozai, T.D. and A.L. Vazquez, *Photoelectric artefact from optogenetics and imaging on microelectrodes and bioelectronics: new challenges and opportunities.* Journal of Materials Chemistry B, 2015. **3**(25): p. 4965-4978.
10. Chastain, J. and R.C. King Jr, *Handbook of X-ray photoelectron spectroscopy.* Perkin-Elmer Corporation, 1992. **40**: p. 221.
11. Oswald, S., *X-Ray photoelectron spectroscopy in analysis of surfaces.* Encyclopedia of Analytical Chemistry: Applications, Theory and Instrumentation, 2006.
12. Smith, E. and G. Dent, *Modern Raman spectroscopy: a practical approach*. 2019: John Wiley & Sons.
13. Kaye, W. and J. McDaniel, *Low-angle laser light scattering—Rayleigh factors and depolarization ratios.* Applied Optics, 1974. **13**(8): p. 1934-1937.
14. Rostron, P., S. Gaber, and D. Gaber, *Raman spectroscopy, review.* laser, 2016. **21**: p. 24.

15. Asher, S.A., *UV resonance Raman spectroscopy for analytical, physical, and biophysical chemistry. Part 2.* Analytical chemistry, 1993. **65**(4): p. 201A-210A.
16. Kudelski, A., *Raman spectroscopy of surfaces.* Surface Science, 2009. **603**(10-12): p. 1328-1334.
17. Kudelski, A., *Analytical applications of Raman spectroscopy.* Talanta, 2008. **76**(1): p. 1-8.
18. Khan, A., S.N. Khan, and W.M. Jadwisienczak, *One step growth of ZnO nano-tetrapods by simple thermal evaporation process: structural and optical properties.* Science of Advanced Materials, 2010. **2**(4): p. 572-577.
19. Pate, S., et al., *Prof. Mitali Dalwadi, Dr. Umesh Upadhyay, A Review on "Uv Visible Spectroscopy".* International Journal of Pharmaceutical Research and Applications, 2022. **7**(5): p. 1144-1151.
20. Penner, M.H., *Basic principles of spectroscopy.* Food analysis, 2017: p. 79-88.
21. Sudharshan, N. and V. Swetha, *UV-VISIBLE SPECTROSCOPY: A COMPREHENSIVE REVIEW ON INSTRUMENTATION.* 2023.
22. Dolgonos, A., T.O. Mason, and K.R. Poeppelmeier, *Direct optical band gap measurement in polycrystalline semiconductors: A critical look at the Tauc method.* Journal of solid state chemistry, 2016. **240**: p. 43-48.
23. Myrick, M.L., et al., *The Kubelka-Munk diffuse reflectance formula revisited.* Applied Spectroscopy Reviews, 2011. **46**(2): p. 140-165.
24. Phokojoe, R., et al., *Effect of annealing time on copper selenide thin films prepared by chemical bath deposition.* Physica B: Condensed Matter, 2023. **666**: p. 415112.
25. Kwiecińska, B., S. Pusz, and B.J. Valentine, *Application of electron microscopy TEM and SEM for analysis of coals, organic-rich shales and carbonaceous matter.* International Journal of Coal Geology, 2019. **211**: p. 103203.
26. Mohammed, A. and A. Abdullah. *Scanning electron microscopy (SEM): A review*. in *Proceedings of the 2018 International Conference on Hydraulics and Pneumatics—HERVEX, Băile Govora, Romania*. 2018.
27. Inkson, B.J., *Scanning electron microscopy (SEM) and transmission electron microscopy (TEM) for materials characterization*, in *Materials characterization using nondestructive evaluation (NDE) methods*. 2016, Elsevier. p. 17-43.
28. Newbury*, D.E. and N.W. Ritchie, *Is scanning electron microscopy/energy dispersive X-ray spectrometry (SEM/EDS) quantitative?* Scanning, 2013. **35**(3): p. 141-168.
29. Tshabalala, Z.P., *Room temperature gas sensing characteristics of titanium dioxide nanostructures: effects of hydrochloric acid on the structure and magnetic properties*. 2016, University of the Free State.

CHAPTER 4-RESULTS AND DISCUSSION

4.1 Morphology and structure analysis of the nanoparticles

4.1.1 X-Ray Diffraction

The powder of ZnO and doped Pd-ZnO samples were analysed using XRD. XRD patterns were recorded on a Bruker Advance D8 instrument with Cu Kα radiation (λ= 0.154056 nm) at 2θ ranging from 20°C to 80°C.

Figure 4.1 shows the XRD spectra of ZnO and Pd-ZnO samples. Intensities are different but they all show peaks centered at 2θ = 32.00, 34.65, 36.49, 47.76, 56.82, 63.07, 66.59, 68.16, 69.31, 72.75, 77.15 degrees corresponds to ZnO planes of (100), (002), (101), (102), (110), (103), (200), (112), (201), (004) and (202), respectively and these were gladly indexed to the wurtzite hexagonal structure, which is consistent with the standard card (JCPDS No: 01–079–0205). These peaks were also present in Pd-decorated ZnO. Pd peak is at 68.10 degrees and correspond to a (220) plane**[1]**.

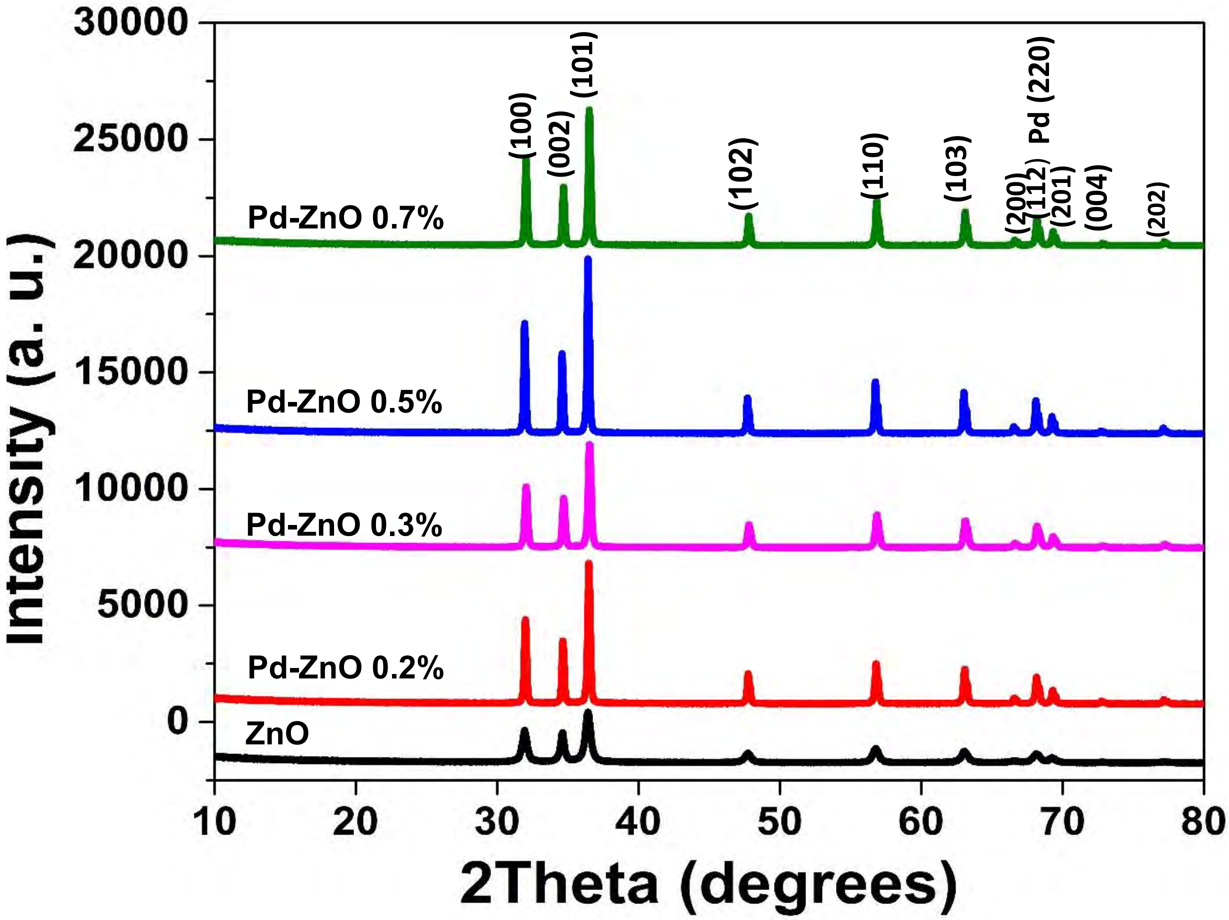

Figure 4. 1*: XRD of Pd–ZnO material and Pure ZnO material.*

The are no extra peaks indicating no impurities in the samples. This shows that the produced ZnO nanostructure is of high purity**[2]**. Doped Pd-ZnO material showed higher diffraction peaks intensity than that of pure ZnO, demonstrating that the crystallinity from pure ZnO was improved with the increase in dopant amount. Diffraction peaks sharpness increase in Pd-ZnO samples because of the presence of Pd molecule. The distinctive peaks of Pd were not explicitly observed in the doping patterns because of the low weight doping ratio of Pd, in addition to the evenly distributed Pd in the ZnO crystal lattice by hydrothermal technique**[2]**. This might also be attributed to the fact that the first three most intense peaks of ZnO namely (100), (002), and (101) suppress the Pd peak which is supposed to be observed at 37.5 degrees. The obtained result is in line with findings reported in the literature**[3]**. The average particle size was determined from full width at half maximum (FWHM) of the diffraction peaks using Scherrer's equation**[4]**. The data is recorded in table **4.1** together with strain, and dislocation. All calculations were performed using the three most intense peaks.

Table 4. 1: *The calculation of crystal size, dislocation density and strain for pure ZnO and Pd doped-ZnO.*

SAMPLES	AVERAGE CRYSTAL SIZE $D = \frac{0.9\lambda}{\beta \cos\theta}$	DISLOCATION DENSITY $\delta = \frac{1}{D^2}$	STRAIN $\varepsilon = \frac{\beta}{4\cos\theta}$
PURE ZnO	37.23555 nm	0.02656 nm^{-2}	0.003162
0.2% Pd-ZnO	37.24106 nm	0.026852 nm^{-2}	0.003157
0.3% Pd-ZnO	37.23463 nm	0.026857 nm^{-2}	0.003163
0.5% Pd-ZnO	37.2452 nm	0.026849 nm^{-2}	0.003153
0.7% Pd-ZnO	37.24391 nm	0.02685 nm^{-2}	0.003154

The 0.5%Pd-ZnO material has the highest average crystal size of 37.2452 nm, meaning the doped material shows an increased in crystal size compared to Pure ZnO. In a crystal lattice, dislocations are breaks or imperfections in the atoms' regular arrangement, and they have a significant impact on the thermal, electrical, and mechanical characteristics of materials. Table 4.1 shows the increasing trend of dislocation density from pure ZnO to the highest doped material which is 0.7%Pd-ZnO. The amount that a substance has distorted or changed shape in relation to its initial state is measured by strain, the strain is a little less on doped Pd-ZnO materials and while 0.3%Pd-ZnO material has the highest strain.

4.2.2 X-ray Photoelectron Spectroscopy (XPS)

The XPS was used to determine the electronic states of the elements at the surface of pure ZnO and 0.5%Pd-ZnO. Figures 4.2 and 4.3 show the survey spectra of pure ZnO and 0.5%Pd-ZnO together their corresponding high resolution elementary spectra respectively.

Pure ZnO

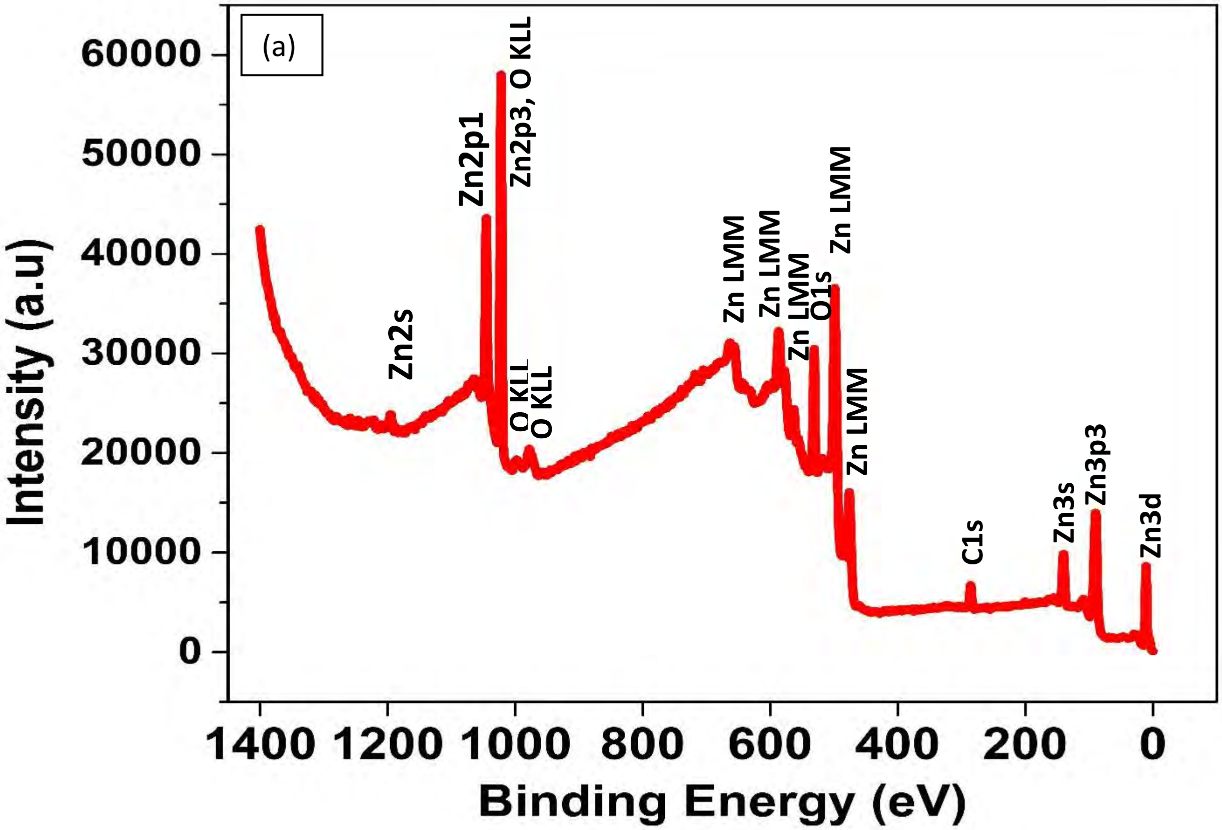

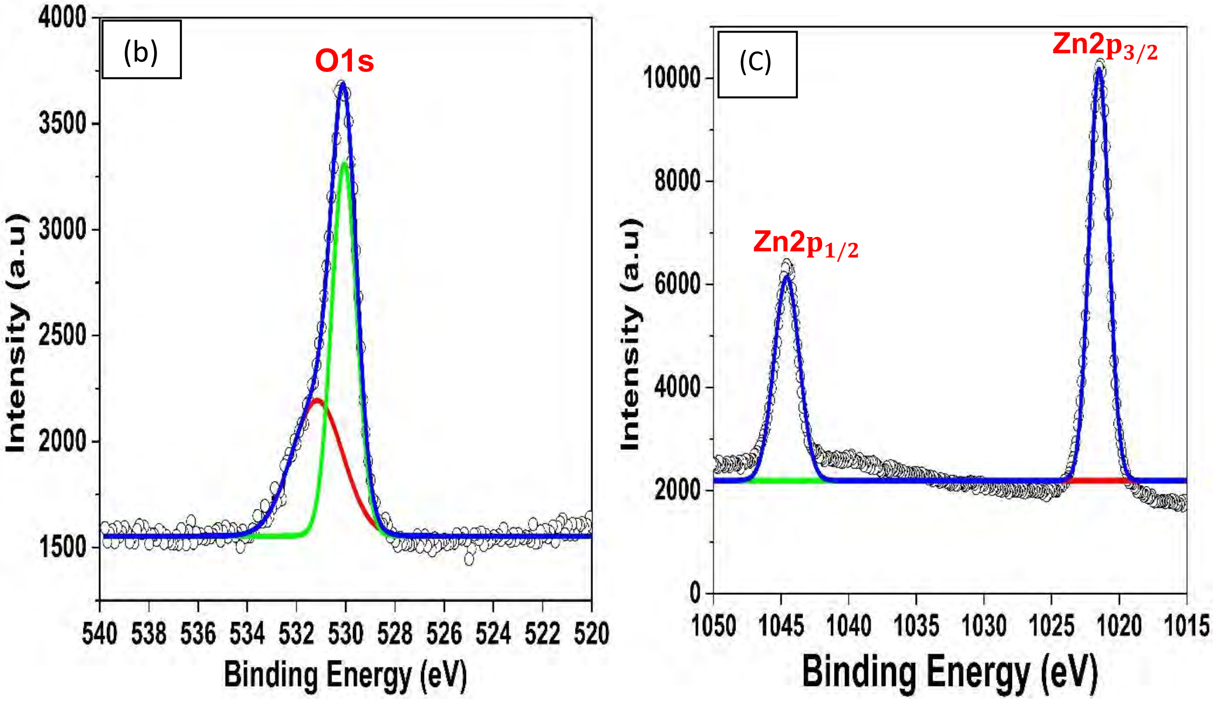

Figure 4. 2*: (a) Wild energy, (b) O1s core level, (c) Zn2p core level XPS spectra of ZnO.*

0.5%Pd-ZnO

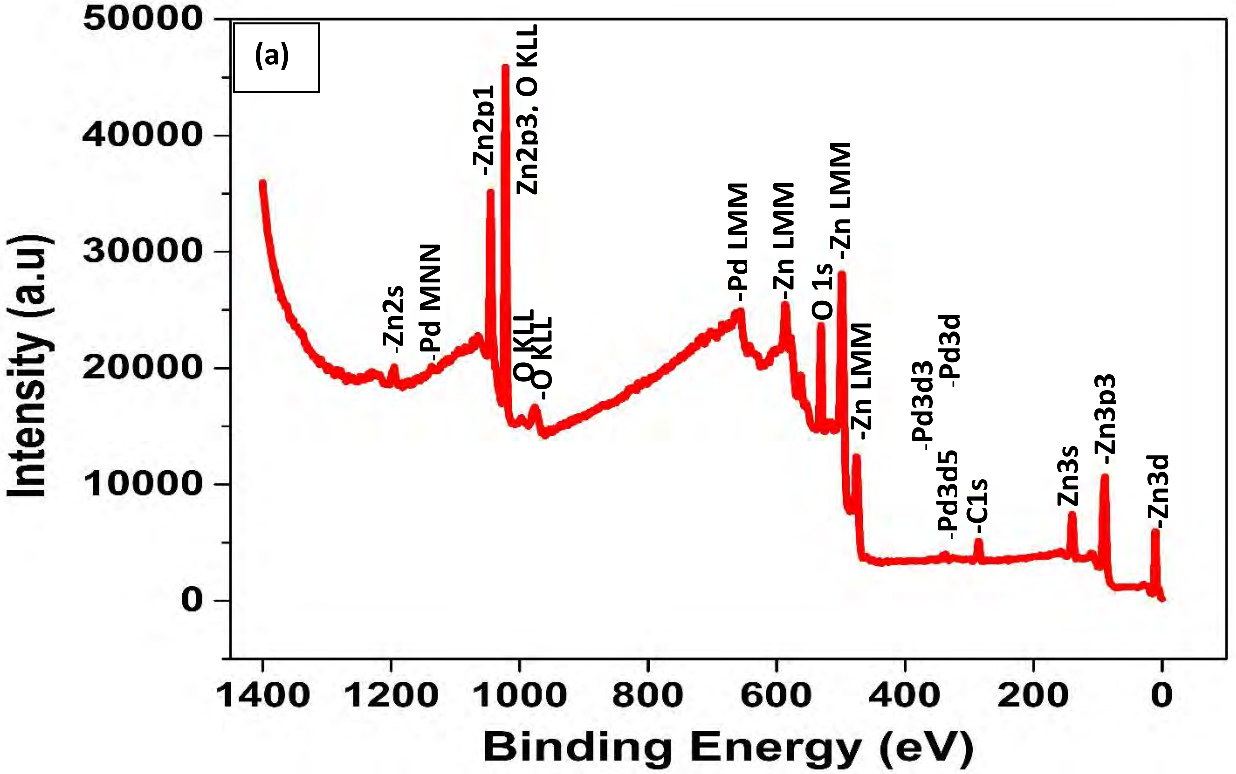
(a)
Intensity (a.u)
Binding Energy (eV)
50000
40000
30000
20000
10000
0
1400
1200
1000
800
600
400
200
0
-Zn2s
-Pd MNN
-Zn2p1
Zn2p3, O KLL
-O KLL
-O KLL
-Pd LMM
-Zn LMM
O 1s
-Zn LMM
-Zn LMM
-Pd3d3
-Pd3d
-Pd3d5
-C1s
Zn3s
-Zn3p3
-Zn3d

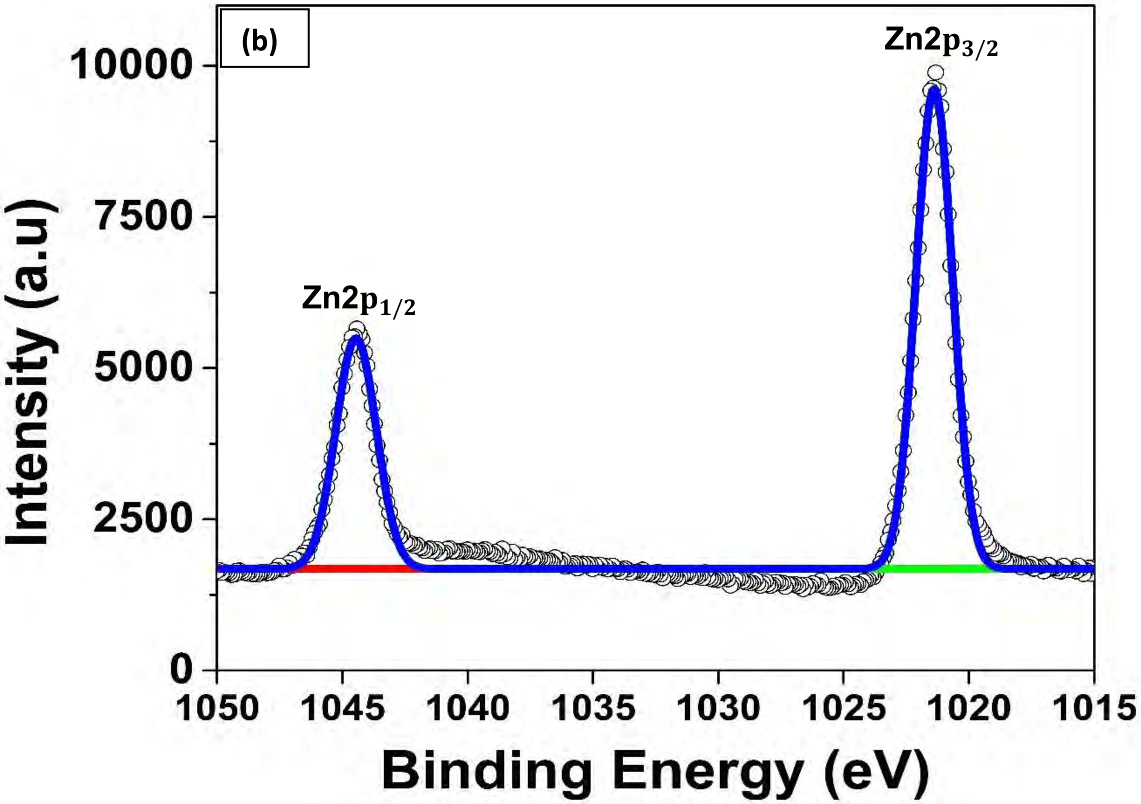
(b)
Intensity (a.u)
Binding Energy (eV)
10000
7500
5000
2500
0
1050
1045
1040
1035
1030
1025
1020
1015
Zn2p$_{1/2}$
Zn2p$_{3/2}$

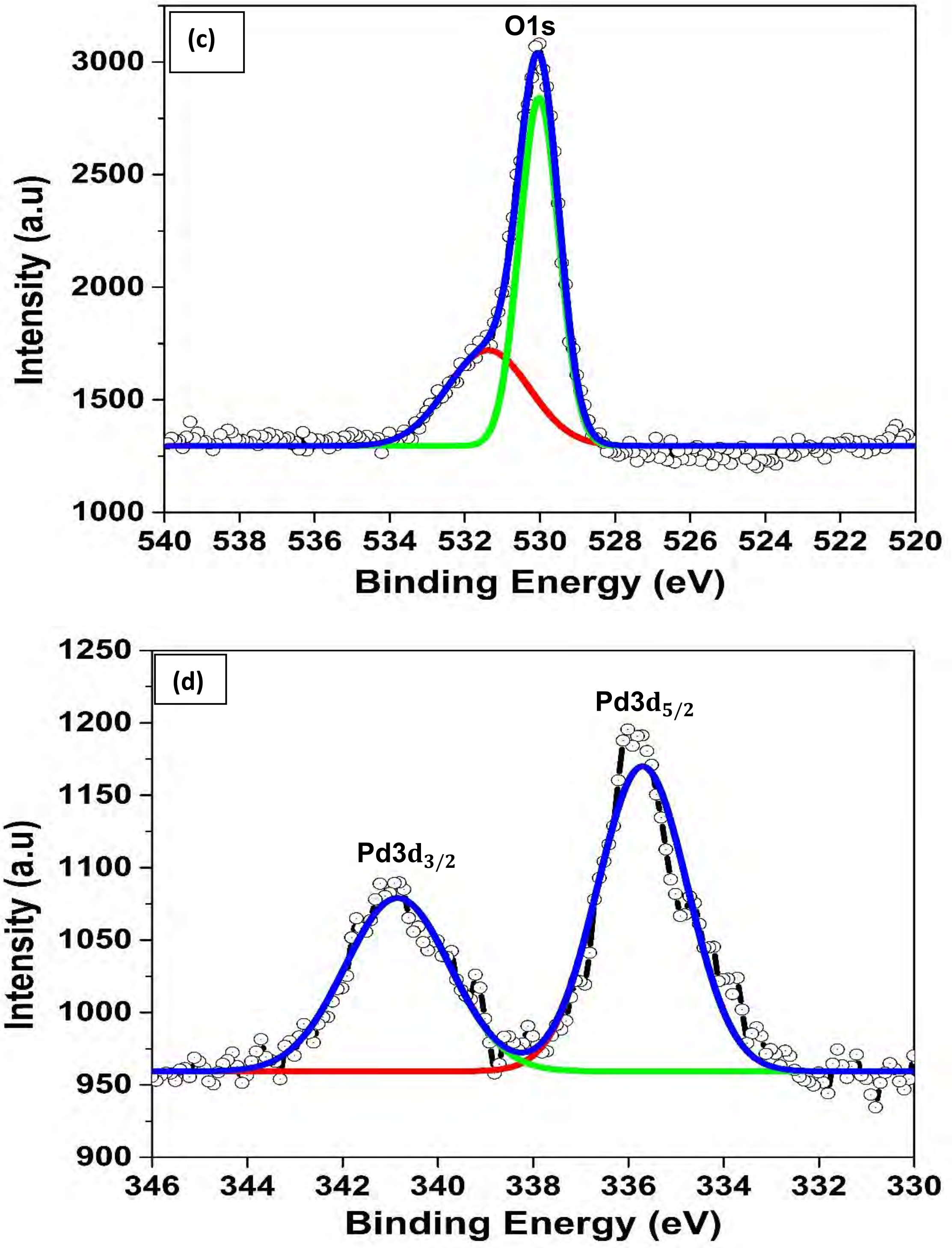

Figure 4. 3*: (a) Wild energy, (b) ZnO2p core level, (c) O1s core level, and (d) Pd3d core level XPS spectra of 0.5%Pd-loaded ZnO.*

Figure 4.2 (a) depicts the survey XPS spectrum of zinc oxide, from which zinc (Zn) and oxygen (O) peak values are clearly observed. Figure 4.2 (b) depicts the O1s core level spectra of pure ZnO. The deconvoluted O1s spectra have two peaks at 532.58 eV and 533.53 eV**[5]**. According to Figure 4.2 (c), the ZnO core level of the Zn2p XPS spectrum exhibits two binding energy peaks at 1044.59 eV and 1021.39 eV, which are associated to $\mathrm{Zn2p_{1/2}}$ and $\mathrm{Zn2p_{3/2}}$, respectively. About 23.2 eV of binding energy is detected between the strong $\mathrm{Zn2p_{1/2}}$and $\mathrm{Zn2p_{3/2}}$ peaks, indicating that Zn is in the +2-oxidation state**[5, 6]**. Fig. 4.3 (d) depicts the core level XPS spectra of the Pd3d region, which provides exact details regarding the chemical state of Pd-NPs over ZnO-NRs. In 0.5%Pd-ZnO two large peaks associated to $\mathrm{Pd3d_{5/2}}$ and $\mathrm{Pd3d_{3/2}}$ doublets are seen in the core level XPS spectra of Pd3d, with binding energies of 336.01eV and 341.71eV, respectively. The primary property of Pd2+, which results from the interaction between Pd and ZnO, is the observed $\mathrm{Pd3d_{5/2}}$ and $\mathrm{Pd3d_{3/2}}$ doublet**[7]**. The spin-orbit doublet separation value described in literature is comparable to the binding energy difference of 5.7 eV between $\mathrm{Pd3d_{5/2}}$ and $\mathrm{Pd3d_{3/2}}$ **[8]**. The Pd3d core level spectrum may also be broken down into four peaks at 337.22, 339.29, 342.47, and 344.55 eV which are caused by Pd metal, Pd(II), and Pd(IV) species in the Pd-ZnO, respectively**[9]**. According to Figure 4.3 (b), the 0.5%Pd-ZnO core level of Zn2p XPS spectrum exhibits two binding energy peaks at 1044.4 eV and 1021.31 eV, which are associated to $\mathrm{Zn2p_{1/2}}$ and $\mathrm{Zn2p_{3/2}}$, respectively. About 23.1 eV of binding energy is detected between the strong $\mathrm{Zn2p_{1/2}}$and $\mathrm{Zn2p_{3/2}}$ peaks, indicating that Zn is in the +2-oxidation state**[5, 6]**. The deconvoluted O1s spectra have two peaks at 532.58 eV and 533.53 eV**[5].** The XPS was able to detect Palladium from the samples with the higher concentrations which is 0.5%Pd-ZnO and 0.7%Pd-ZnO. Other samples such as 0.2%Pd-ZnO and 0.3%Pd-ZnO behaved like pure ZnO i.e no Pd was not observed.

***Table 4. 2**: XPS plot fitting for ZnO, 0.5%Pd-ZnO and 0.7%Pd-ZnO using the Origin software complemented with Fityk software.*

***Table 4.2. 1**: The fitting of ZnO peaks.*

ZnO	AREA	BINDING ENERGY (eV)	INTENSITY (a.u.)	FWHM
Highest Zn peak	22949.8	1021.39	10266.6	2.1
Lowest Zn Peak	20373.8	1044.59	6379.97	3
Oxygen Peak	13679	530.19	3671.59	3.5

***Table 4.2. 2**: The fitting of Pd-ZnO 0.5% peaks.*

0.5%Pd- ZnO	AREA	BINDING ENERGY (eV)	INTENSITY (a.u.)	FWHM
Highest Zn peak	20456.1	1021.31	10114.4	1.9
Lowest Zn Peak	18720.3	1044.4	6280.91	2.8
Oxygen Peak	11769.4	530.01	3071.27	3.6
Highest Pd peak	25722	336.01	1208.21	20
Lowest Pd Peak	185.37	341.71	96.74	1.8

***Table 4.2. 3**: The fitting of 0.7%Pd-ZnO peaks.*

0.7%Pd- ZnO	AREA	BINDING ENERGY (eV)	INTENSITY (a.u.)	FWHM
Highest Zn peak	13549.1	1021.18	6699.22	1.9
Lowest Zn Peak	12270.1	1044.38	4269.26	3.1
Oxygen Peak	7422.56	530.08	2249.36	31
Highest Pd peak	17810.6	335.58	836.60	20
Lowest Pd Peak	44.48	340.98	46.43	0.9

The XPS fitting table 4.2.2 shows that Zn, O, Pd peaks of the 0.5%Pd-ZnO sample have a greater Area, Energy (eV) and intensity (a.u.) compared to 0.7%Pd-ZnO sample in table 4.2.3. The two ZnO peaks in table 4.2.1 and Oxygen peaks are greater than 0.5%Pd-ZnO and 0.7%Pd-ZnO. This happens because the 0.5%Pd concentration is the optimal amount doping concentration in Hydrothermal method.

4.2.3 Scanning Electron Microscopy (SEM)

Using a JSM-JEOL 6390 Scanning Electron Microscope, images of the ZnO, 0.2%Pd-ZnO, 0.3%Pd-ZnO, 0.5%Pd-ZnO and 0.7%Pd-ZnO nanoparticles were captured, and the result are shown in figure 4.4.

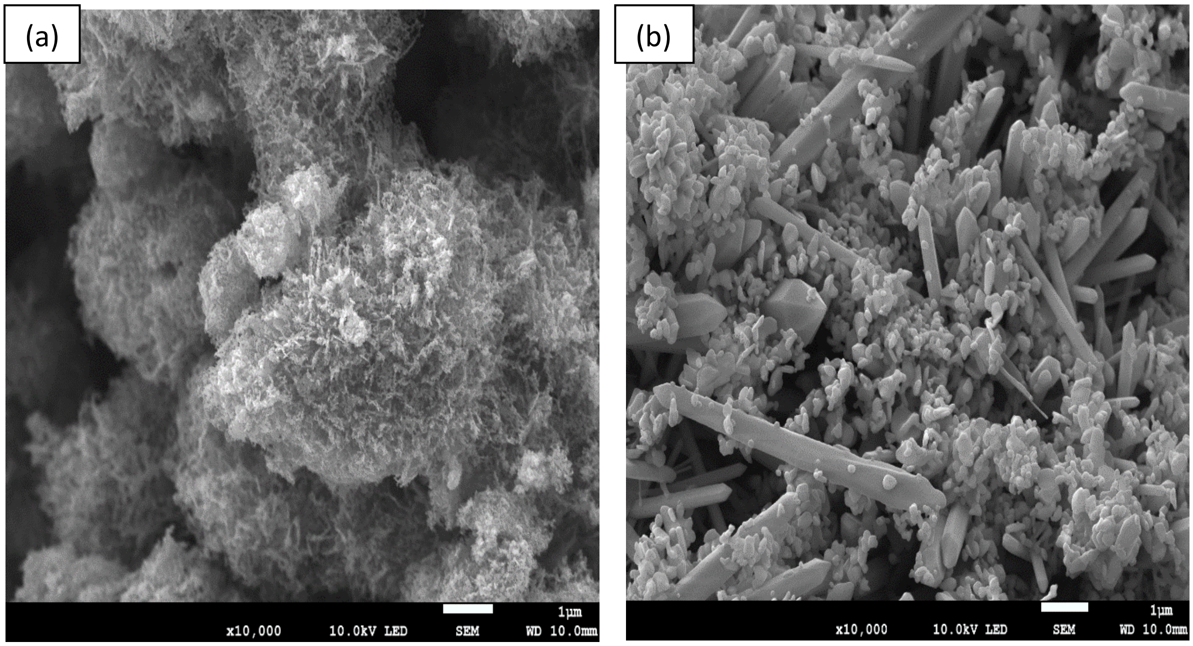

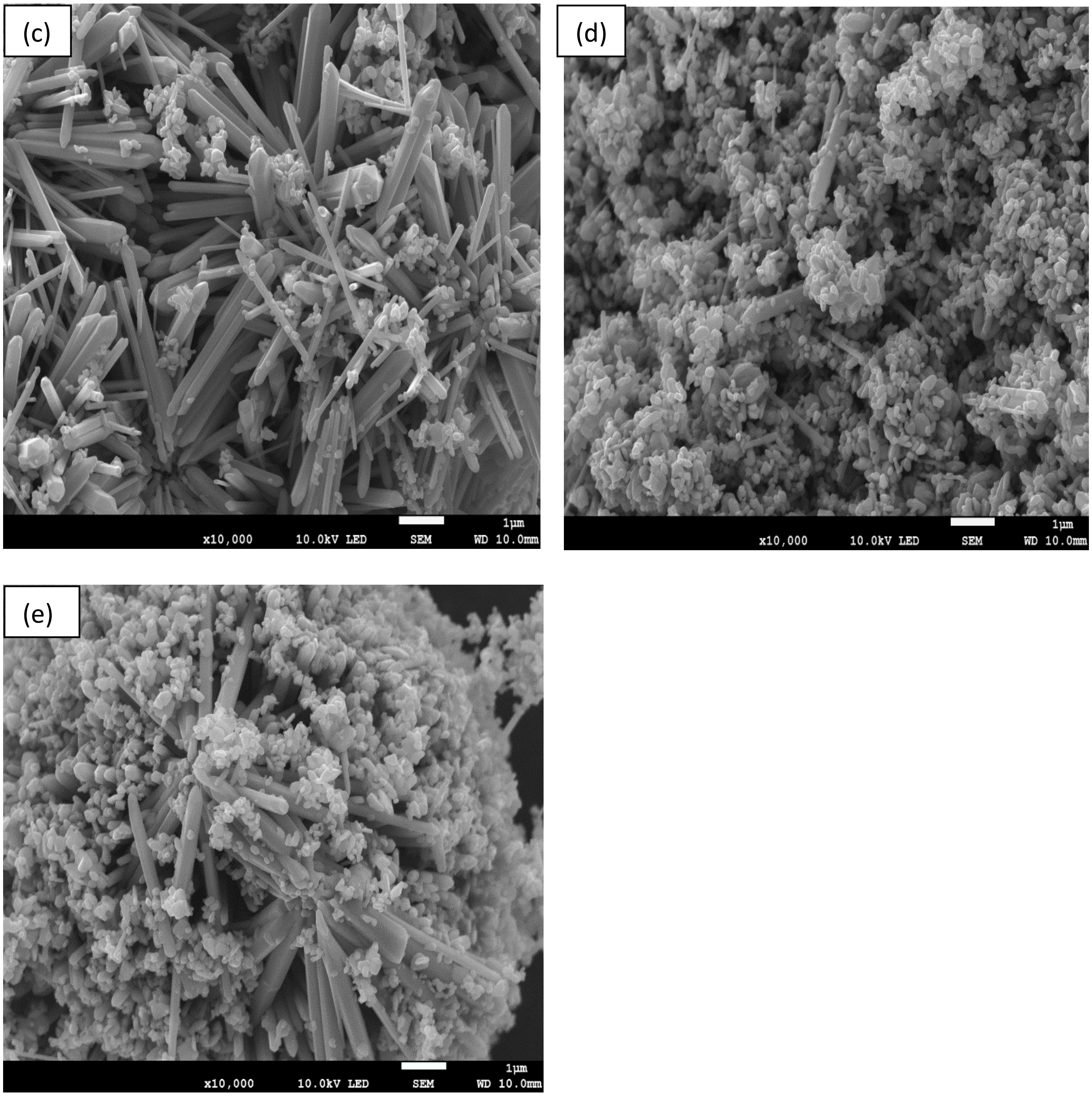

***Figure 4. 4**: The SEM images of the (a)Pure ZnO, (b) 0.2%Pd-ZnO, (c) 0.3%Pd-ZnO, (d) 0.5%Pd-ZnO and (e) 0.7%Pd-ZnO.*

Figure 4.4 (a) shows the Scanning Electron Microscope (SEM) image of the zinc oxide particles under higher magnification and it reveals that the particles are marginally agglomerated, and complete separation of nanoparticles is not good. We can see that the particles are held together because of weak physical forces. The particles were formed with size in micron range. For (b) 0.2%Pd-ZnO and (c) 0.3%Pd-ZnO a small difference between them was observed. Both materials are separated due to the introduction of Pd to form rods structures with nanoparticles attached to them, this was observed in micro range. There are also some small gaps in the material between particles. As the concentration of the dopant Palladium was increased to 0.5% in figure 4.4 (d) and 0.7% in figure 4.4 (e), rods particles were still observed with nanoparticles covering them like a cluster, leading to fewer gaps between particles and this was observed in micro range also. The nanorods are clearly observed in 0.3%Pd-ZnO sample, further increased in dopant amount rods grew with nanoparticles.

The longer ZnO nanorods are a result of the seed layer surface being more reactive during the nucleation stage. Their creation can be attributed to the fact that ZnO possesses a polar hexagonal crystal structure, displaying significant anisotropy in growth along the c-axis, specifically the (0001) facet due to its lowest surface energy **[10]**. Within the ZnO crystal, zinc and oxygen atoms are placed in a c-axis in an alternating order, with Zn-terminated (0001) surfaces on top, exhibiting catalytic activity, and O-terminated (0001) surfaces at the bottom, which are chemically inert**[11]**. In hydrothermal conditions, the polar (0001) faces exhibit the most rapid growth rate among various facets **[10, 11]**, thus favouring the preferred morphology of nanorods. The growth of nanoparticles is faster than the growth of rods, with the maximum growth of rods being in the 0.5%Pd-ZnO sample.

4.2.4 Energy Dispersive Spectroscopy (EDS)

Energy Dispersive Spectroscopy (EDS) micro analysis within SEM, is based on the generation of distinctive X-rays that indicate the existence of elements present in the specimens. In addition to the high-resolution information about the sample surface morphology supplied by the electron microscope, qualitative information on elemental composition with approximately 10-nm spatial resolution can be obtained**[12]**.

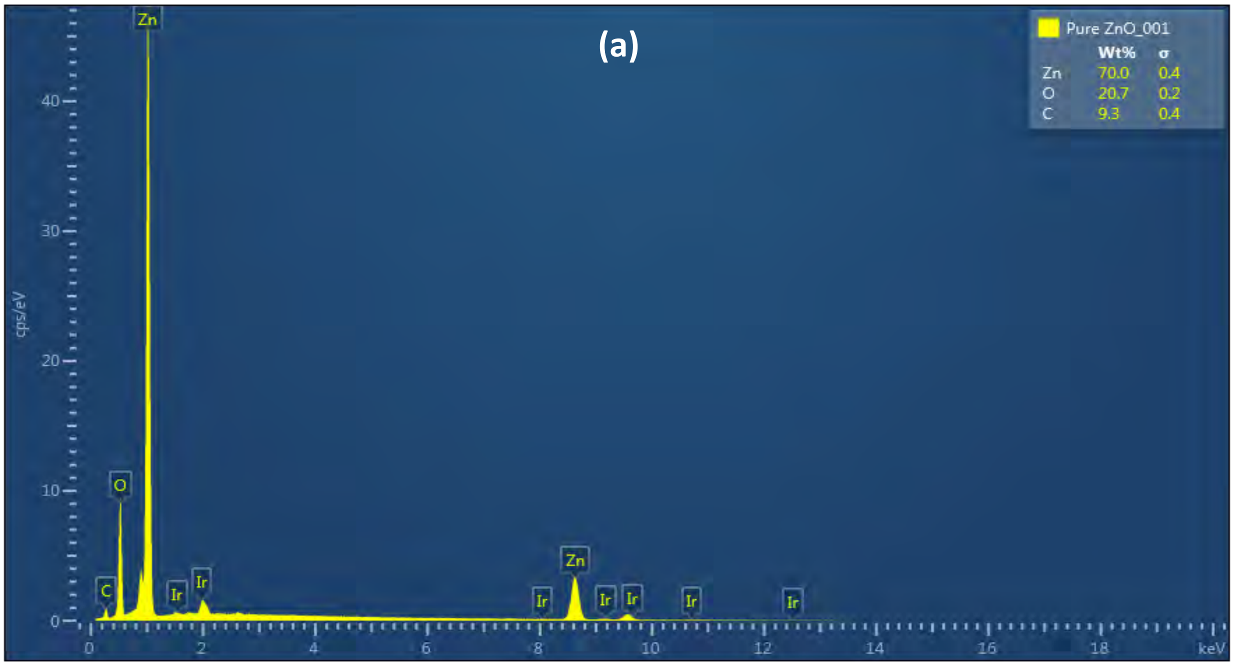
(a)
Pure ZnO_001
Wt% σ
Zn 70.0 0.4
O 20.7 0.2
C 9.3 0.4
cps/eV
0
10
20
30
40
Zn
O
C
Ir
Ir
Zn
Ir
Ir
Ir
Ir
Ir
0
2
4
6
8
10
12
14
16
18
keV

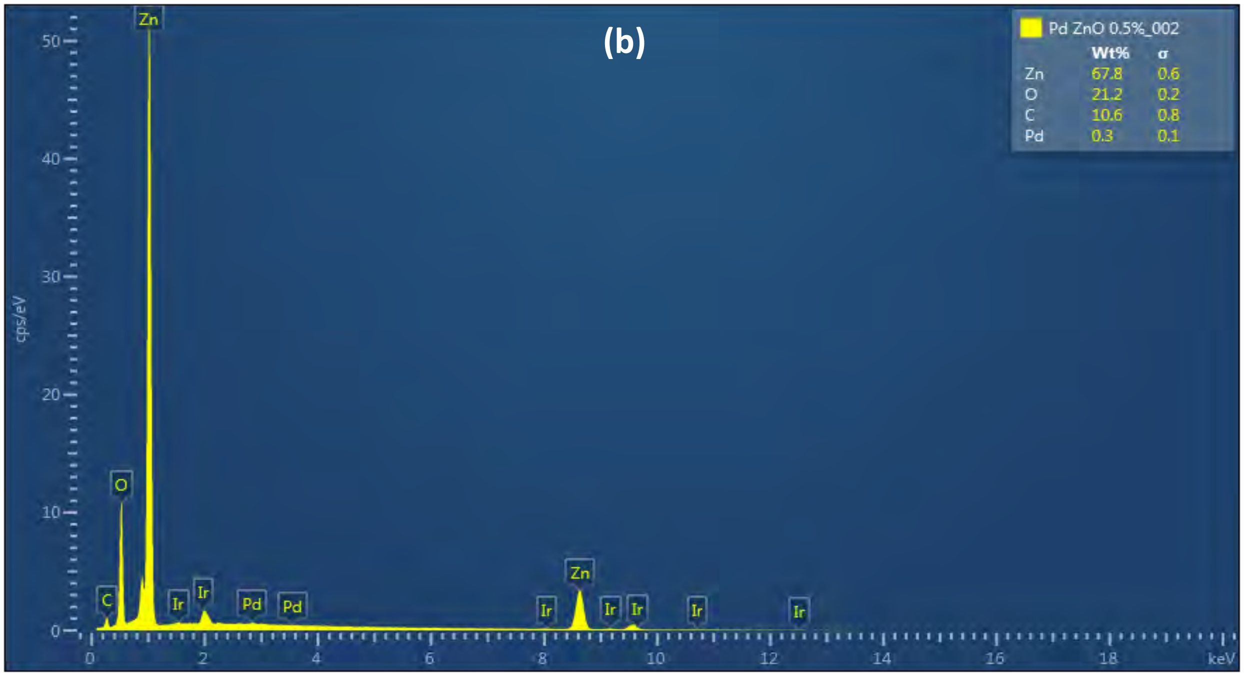
(b)
Pd ZnO 0.5%_002
Wt% σ
Zn 67.8 0.6
O 21.2 0.2
C 10.6 0.8
Pd 0.3 0.1
cps/eV
0
10
20
30
40
50
Zn
O
C
Ir
Ir
Pd
Pd
Zn
Ir
Ir
Ir
Ir
Ir
0
2
4
6
8
10
12
14
16
18
keV

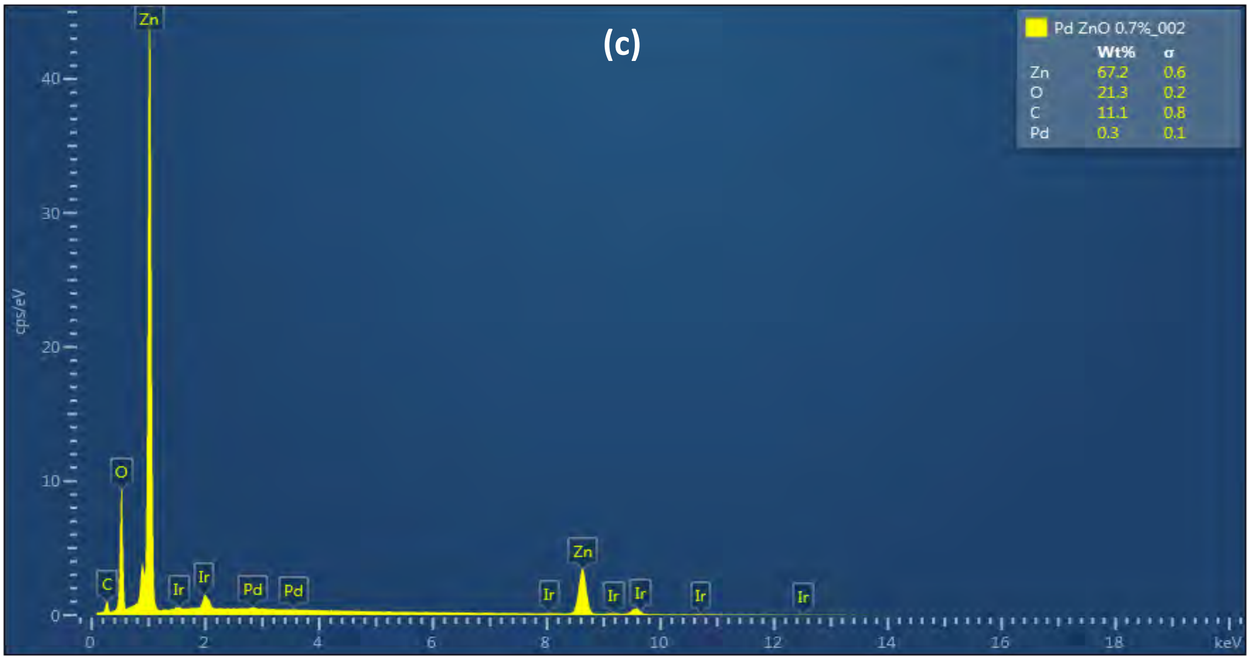

Figure 4. 5*: EDS spectra of (a) ZnO, (b) 0.5%Pd-ZnO, and 0.7%Pd-ZnO.*

Figure 4.5 shows the EDS spectra of two Pd loaded on ZnO and pure ZnO. With regard to the pure ZnO, the EDS spectrum in figure 4.5 (a) revealed the presence of Zn and O components. The presence of Zn, O, and Pd was identified for higher doped samples 0.5%Pd-ZnO and 0.7%Pd-ZnO. The lower doped samples 0.2%Pd-ZnO and 0.3%Pd-ZnO did not show any Pd atom; they behaved like pure ZnO in EDS, this is because of the small concentration of the added Pd, and the resolution of the EDS. 0.5%Pd-ZnO and Pd-ZnO 0.7% spectra in Figure 4.5 (b) and Figure 4.5 (c) respectively verified the presence of Pd in two small peaks. Oxygen for the first peak in all samples is an additional element associated with impurities which were found in a spectrum, and the other small peaks observed.

Table 4. 3*: The discovered compositions of atomic elements of Zn, O, and Pd using EDS.*

Table 4.3. 1*: Fitting data for the elemental composition of ZnO.*

ZnO	WEIGHT (wt%)	SIGMA	APPARENT CONCENTRATION	HEIGHT (cps/eV)	ENERGY (KeV)	AREA
1st peak Zn	70.0	0.4	16.58	25513	1.02	1901.04
2nd peak Zn				1860	8.62	296.986
O	20.7	0.2	47.48	5112	0.52	326.49

Table 4.3. 2*: Fitting data for the elemental composition of Pd-ZnO 0.5%.*

Pd-ZnO 0.5%	WEIGHT (wt%)	SIGMA	APPARENT CONCENTRATION	HEIGHT (cps/eV)	ENERGY (KeV)	AREA
1st peak Zn	65.65	0.59	54.92	34099	1.02	2540.81
2nd peak Zn				2254	8.62	383.89
O	21.41	0.24	20.75	7200	0.52	459.85
1st peak Pd	0.32	0.08	0.31	446	2.84	1096.68
2nd peak Pd				6.00	3.58	0.06

***Table 4.3. 3**: Fitting data for the elemental composition of Pd-ZnO 0.7%.*

Pd-ZnO 0.7%	WEIGHT (wt%)	SIGMA	APPARENT CONCENTRATION	HEIGHT (cps/eV)	ENERGY (KeV)	AREA
$\mathbf{1}^{st}$ peak Zn	67.20	0.62	46.16	33109	1.02	2467.04
$\mathbf{2}^{nd}$ peak Zn				2515	8.62	428.34
O	21.32	0.25	17.14	7129	0.52	455.315
$\mathbf{1}^{st}$ peak Pd	0.34	0.09	0.27	436	2.84	1030.32
$\mathbf{2}^{nd}$ peak Pd				1.63	3.58	0.02

The observed peaks of Zn, O and Pd were fitted using fityk software. Most of the 0.5%Pd-ZnO EDS peaks are greater in wt%, sigma, apparent concentration, height energy and Area than all other samples as shown in table 4.3.2. The higher peaks are associated with higher-energy X-rays emitted by elements in the sample. This means that the 0.5%Pd-ZnO sample has got stronger chemical bonds compared to pure ZnO and 0.7%Pd-ZnO.

4.2.5 Raman Analysis

Raman-scattering spectra of the grown ZnO, 0.2%Pd-ZnO, 0.3%Pd-ZnO, 0.5%Pd-ZnO and 0.7%Pd-ZnO structures were analysed using a 473 nm blue laser as the excitation source of MR-150 Raman from JINR (Russia). The structure of the crystal as well as any imperfections in the crystal structure are often particularly sensitive to the Raman signals**[13]**. Wurtzite, the hexagonal crystal structure of ZnO, is in the C_{6v}^{4} space group and has two formula units per primitive cell with all atoms occupying the C_{3v} sites**[14]**. A1 and E1 modes are polar and divide into transverse optical (A1T and E1T) and longitudinal-optical (A1L and E1L) phonons, respectively, while the E_2 mode is made up of two modes of low- and high-frequency phonons (E_2(low) and E_2(high)) which are Raman active**[15]**.

According to group theory, there are eight sets of zone centre optical phonons. Figure 4.6 shows Raman shift for all sample.

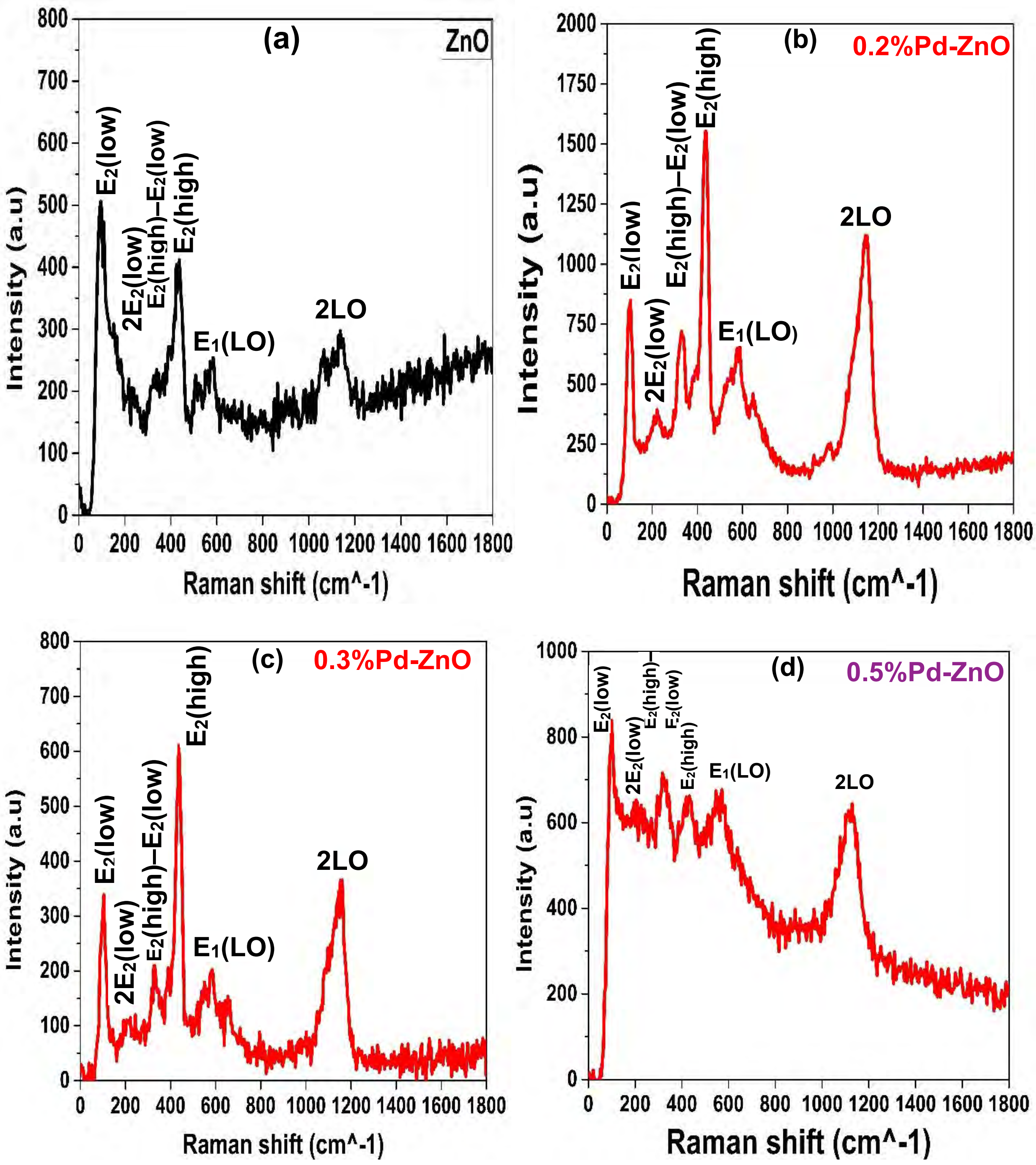

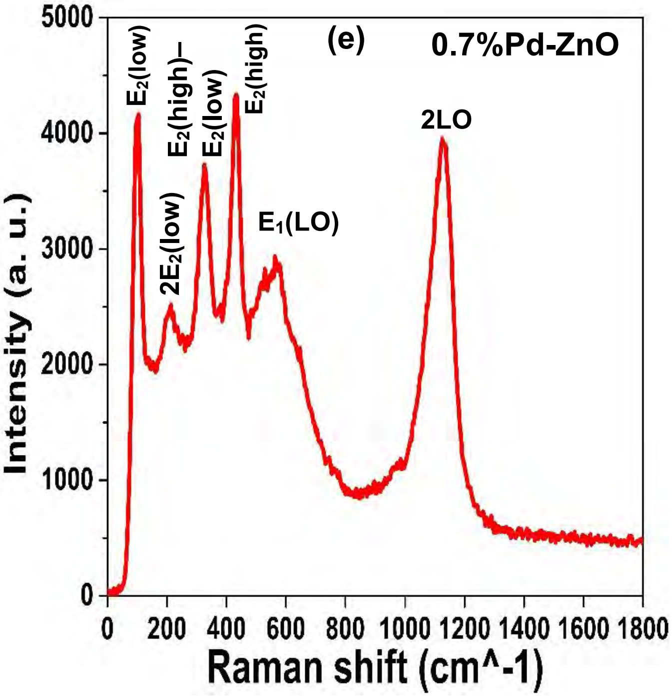

***Figure 4. 6**: Raman shift of different material (a) ZnO, (b) 0.2%Pd-ZnO, (c) 0.3%Pd-ZnO, 0.5%Pd-ZnO, and (d) 0.7%Pd-ZnO.*

The two dominant peaks at 95 cm^{-1} and 436 cm^{-1} can be observed in all samples and are attributed to the E_2(low) and E_2(high) modes of the wurtzite structure of ZnO, respectively**[16].** E_2(low) and E_2(high) are comparable with the literature on the Raman active optical phonon mode, which is known as the major dominant sharp peak identified as E_2 at 437 cm-1 and is an indicator of the wurtzite hexagonal phase ZnO**[17]**. The E_2(High) peak shifts of nanorods are shifted with +8 units and also vibrate the same as nanoflowers**[18].** E_2(Low) is red-shifted for nanorods and sphere-like structures and E_2(High) is blue-shifted in all morphologies, but E_2(Low) was not apparent in other structures**[18, 19]**. For nanorods the E_2(High) mode is blue shifted by 6, this suggests that the pure ZnO samples' crystallinity is lower. However, when the samples have been doped with Pd, a crucial narrowing that denotes greater crystallinity is observed and it is comparable with the literature. The blueshift in E_2(High) can be due to the laser-induced optical phonon confinement in nanostructures by defects or impurities in the nanostructures or because of anisotropic internal stresses corresponding to various development orientations, induce heating and/or phonon localization**[20-22].**The edge-filter applied in these spectra to exclude the contribution of the Rayleigh intensity slightly truncates the E_2(low) peak at 95 cm^{-1} **[23]**.

Other peaks with lower intensities for ZnO material were observed at 1137 cm^{-1}, and 583 cm^{-1} which can be attributed to the 2LO and E_1(LO) modes, respectively**[23]**. When compared to other detected peaks, the E_2(High) mode at 437 cm^{-1} had a substantially greater intensity and sharp peak, which showed that the as grown ZnO structures are of the well-crystallized wurtzite hexagonal phase**[24]**. The peaks corresponding to the E_2(low) and E_2(high) modes, which represent the perfection of the ZnO crystal, are wider, as shown in the case of the ZnO nanostructure and for both concentrations of Pd**[25]**. Oxygen vacancy defect (VO) is the cause of the Raman peaks between 520 cm^{-1} and 600 cm^{-1} **[26, 27]**. The Pd-ZnO material shows a very great shift and more intense peaks proportional to the increase in the concentration of the dopant Pd, improving the crystallinity. Two peaks which are partially observed in the pure ZnO samples are at 328 cm^{-1} and 217 cm^{-1} respectively, relating to E_2(high)–E_2(low), $2E_2$(low). They are clear and prominent in the doped Pd-ZnO material**[28]**. 0.5%Pd-ZnO does not show $2E_2$(low). The ZnO Raman plot in figure 4.6 (a) exhibits a noisy signal which shows that the crystallinity is not pure compared to doped material from figure 4.6; (b), (c), (d) and (e). Big shifts are observed on the pure ZnO material compared to Pd-ZnO doped materials. Peaks are clearly fitted and recorded in Table 4.4.

***Table 4. 4**: The fitted peaks the Raman shift (cm−1) peaks using fityk software for pure ZnO, 0.2%Pd-ZnO, 0.3%Pd-ZnO, 0.5%Pd-ZnO and 0.7%Pd-ZnO with the literature peaks.*

SYMMETRY	LITERATURE RAMAN SHIFT (cm^-1)	ZnO (cm^-1)	0.2%Pd-ZnO (cm^-1)	0.3%Pd-ZnO (cm^-1)	0.5%Pd-ZnO (cm^-1)	0.7%Pd-ZnO (cm^-1)
E2(Low)	101	95	104	104	100	95
2E2(Low)	203	217	209	191	-	209
E2(High)-E2(Low)	333	338	330	330	317	330
E2(High)	437	436	436	436	419	432
E2(Lo)	583	583	589	584	571	575
2LO	1158	1137	1145	1161	1125	1125

The 0.5%Pd-ZnO structure has the smallest Raman shift compared to other samples and the recent literature. A small Raman shift is associated with weaker or less intense Raman signals.

4.3 Optical properties

4.3.1 UV/vis

The ZnO, 0.2%Pd-ZnO, 0.3%Pd-ZnO, 0.5%Pd-ZnO and 0.7%Pd-ZnO material were tested for the absorbance since they are powders with a defined crystal form, and they have a direct transition band gap. Tauc methods were used to interpret the optical properties.

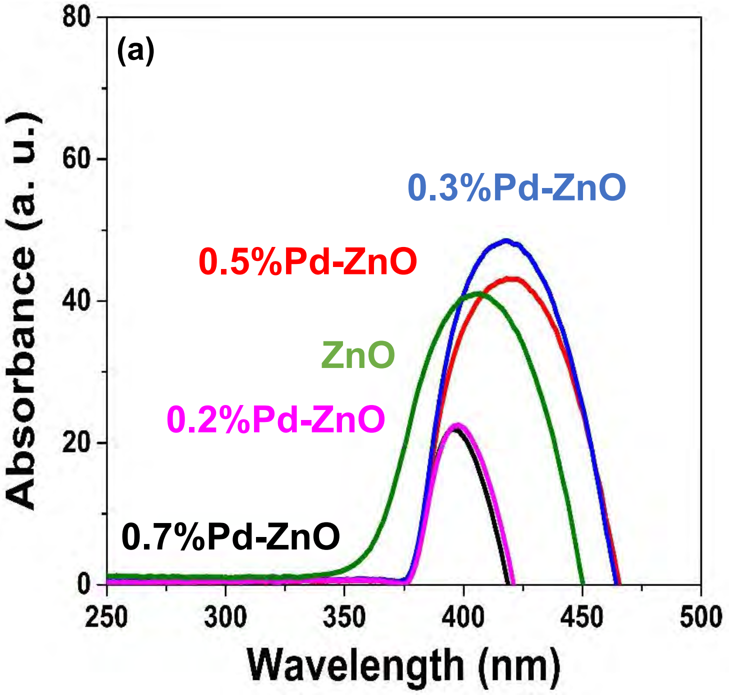

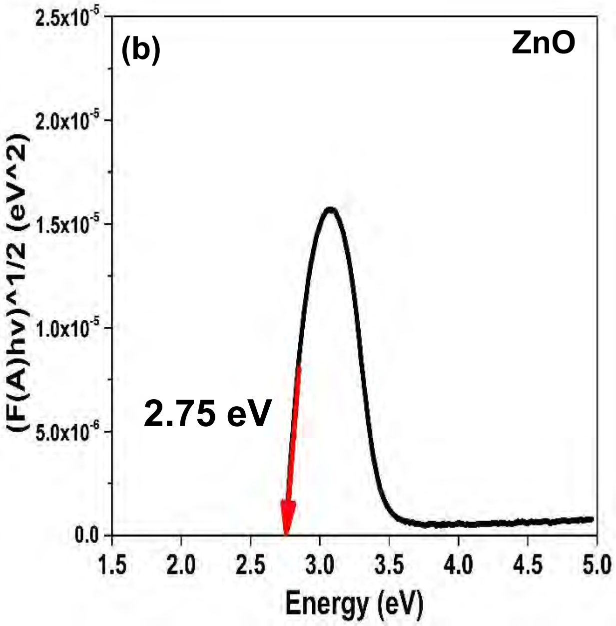
(b)
ZnO
2.75 eV
(F(A)hv)^1/2 (eV^2)
2.5x10⁻⁵
2.0x10⁻⁵
1.5x10⁻⁵
1.0x10⁻⁵
5.0x10⁻⁶
0.0
1.5
2.0
2.5
3.0
3.5
4.0
4.5
5.0
Energy (eV)

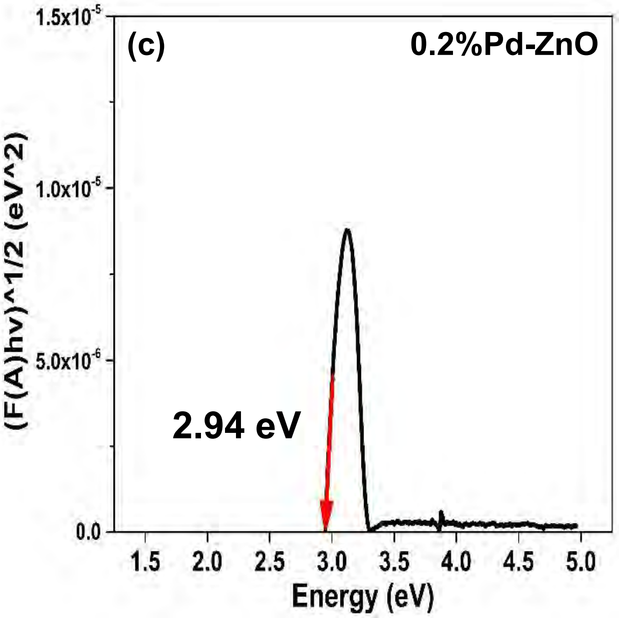
(c)
0.2%Pd-ZnO
2.94 eV
(F(A)hv)^1/2 (eV^2)
1.5x10⁻⁵
1.0x10⁻⁵
5.0x10⁻⁶
0.0
1.5
2.0
2.5
3.0
3.5
4.0
4.5
5.0
Energy (eV)

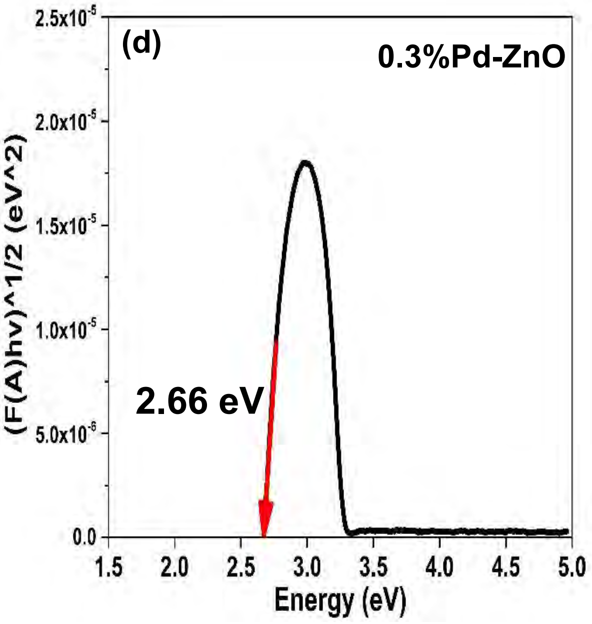
(d)
0.3%Pd-ZnO
2.66 eV
(F(A)hv)^1/2 (eV^2)
2.5x10⁻⁵
2.0x10⁻⁵
1.5x10⁻⁵
1.0x10⁻⁵
5.0x10⁻⁶
0.0
1.5
2.0
2.5
3.0
3.5
4.0
4.5
5.0
Energy (eV)

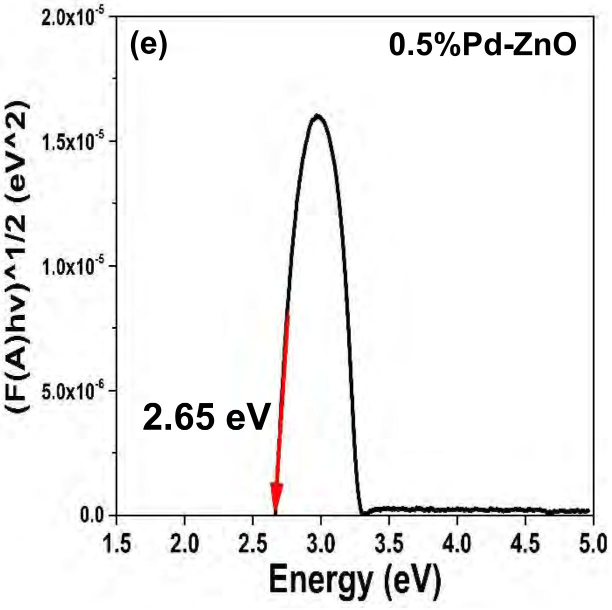
(e)
0.5%Pd-ZnO
2.65 eV
(F(A)hv)^1/2 (eV^2)
2.0x10⁻⁵
1.5x10⁻⁵
1.0x10⁻⁵
5.0x10⁻⁶
0.0
1.5
2.0
2.5
3.0
3.5
4.0
4.5
5.0
Energy (eV)

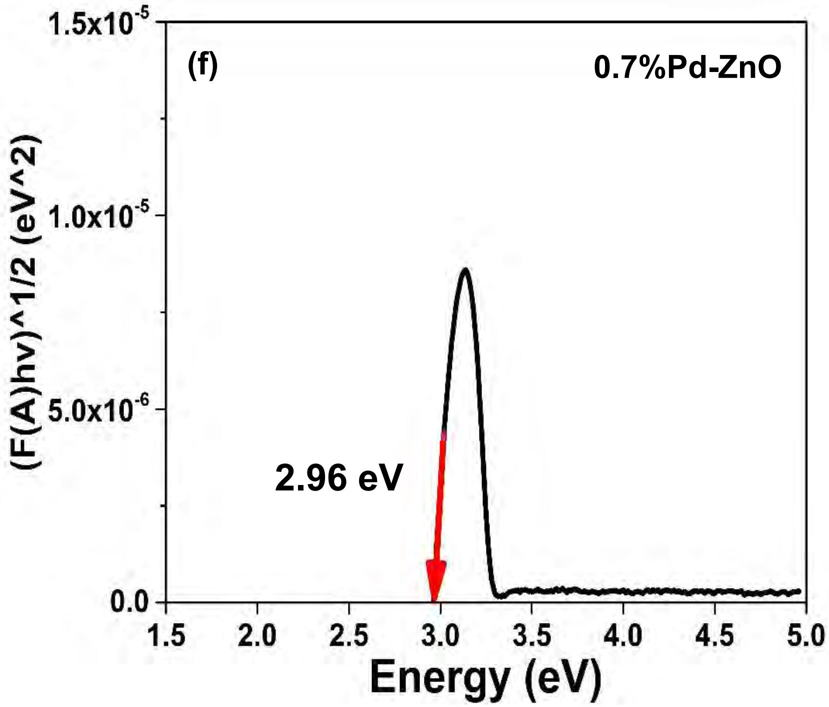

Figure 4. 7*: UV/vis spectra of (a) Absorbances and wavelengths, band gaps of (b) ZnO, (c) 0.2%Pd-ZnO, (d) 0.3%Pd-ZnO, (e) 0.5%Pd-ZnO and (f) 0.7%Pd-ZnO.*

Figure 4.7 (a) displays the results of UV-vis measurements for ZnO, 0.2%Pd-ZnO, 0.3%Pd-ZnO, 0.5%Pd-ZnO and 0.7%Pd-ZnO in the 250-800 nm wavelength range. The absorption peaks for ZnO, 0.2%Pd-ZnO, 0.5%Pd-ZnO, 0.7%Pd-ZnO are 406 nm, 398 nm, 418 nm, 421 nm, 396 nm respectively and are due to electronic transitions of the electrons from valence band to conduction band. The greatest absorption peak was observed at 421 nm for 0.5%Pd-ZnO, and the absorption was mostly centered in the UV area, with minimal absorption of visible light. The passage of electrons from the valence band to the conduction band caused the absorption band to appear at 421 nm. Pd-ZnO composite material's UV-vis spectra revealed a slightly shifted peak. This demonstrated the introduction of an effective impurity band via Pd doping. According to data presented in the literature, it is possible that the metal ions were present in the internal ZnO lattice and that the interaction of the doping ions with the ZnO damaged a portion of the original lattice, creating lattice defects and rendering the ZnO absorption edge mobile**[29]**. The rate of creation of electron-hole pairs on the catalyst surface rose significantly, as evidenced by the redshift in the absorption wavelength range and the rise in absorption intensity, leading to the catalyst's improved photocatalytic efficiency**[30]**. The creation of defective energy levels between the valence and conduction bands in the ZnO band structure was the most likely cause of the redshift in the absorption wavelength range for the Pd-doped ZnO**[31]**.

Table 4. 5*: The material absorption wavelengths with the calculated bang gap and the interpolated band gap.*

SAMPLES	WAVELENGTH (λ) IN (nm)	CALCULATED BAND GAP FROM THE FORMULA ENERGY=h*C/(λ)	INTERPOLATED BAND GAP FROM ORIGIN
ZnO	406	3.05	2.75
0.2%Pd-ZnO	398	3.12	2.94
0.3%Pd-ZnO	418	2.97	2.66
0.5%Pd-ZnO	421	2.94	2.65
0.7%Pd-ZnO	396	3.13	2.96

In table 4.5 the 0.2%Pd-ZnO and 0.7%Pd-ZnO material show a theoretical deviation on the band gap, which is greater than the band gap of ZnO, because introducing Pd metal should reduce the band gap. The first band gap was calculated using the formular which requires the absorption wavelength, planks constant and speed of light. The other band gap was interpolated on the Origin software. All the band gas shows the same trends. There is a decreasing trend of a band gap from 0.2%Pd-ZnO, 0.3%Pd-ZnO to 0.5%Pd-ZnO then a big increase from 0.5%Pd-ZnO to 0.7%Pd-ZnO. This means that 0.5%Pd-ZnO is a sample with the smallest band gap. The absorption of light is inversely proportional to the band gap.

4.4 References

1. Hemalatha, K., et al., *Visible light assisted photocatalytic degradation of organic dyes on TiO 2–CNT nanocomposites.* Journal of Sol-Gel Science and Technology, 2015. **73**: p. 72-82.
2. Hashim, F.S., et al., *Effect of (Ag, Pd) doping on structural, and optical properties of ZnO nanoparticales: As a model of photocatalytic activity for water pollution treatment.* Chemical Physics Letters, 2019. **737**: p. 136828.
3. Bruce, J., K. Bosnick, and E.K. Heidari, *Pd-decorated ZnO nanoflowers as a promising gas sensor for the detection of meat spoilage.* Sensors and Actuators B: Chemical, 2022. **355**: p. 131316.
4. Mohan, A.C. and B. Renjanadevi, *Preparation of zinc oxide nanoparticles and its characterization using scanning electron microscopy (SEM) and X-ray diffraction (XRD).* Procedia Technology, 2016. **24**: p. 761-766.
5. Cao, P., et al., *Ethanol sensing behavior of Pd-nanoparticles decorated ZnO-nanorod based chemiresistive gas sensors.* Sensors and Actuators B: Chemical, 2019. **298**: p. 126850.
6. Jain, G., et al., *Porous zinc oxide nanocrystalline film deposition by atmospheric pressure plasma: Fabrication and energy band estimation.* Plasma Processes and Polymers, 2017. **14**(12): p. 1700052.
7. Zhang, Y.-H., et al., *2D nanosheet-assembled PdZnO microflowers for acetone sensor with enhanced performances.* Journal of Physics and Chemistry of Solids, 2019. **124**: p. 330-335.
8. Polzonetti, G., et al., *The interface between aluminium and a rod-like organometallic Pd-containing polymer film investigated by XPS.* Journal of electron spectroscopy and related phenomena, 1997. **85**(1-2): p. 73-80.
9. Qu, W.-L., et al., *Investigation on performance of Pd/Al 2 O 3–C catalyst synthesized by microwave assisted polyol process for electrooxidation of formic acid.* Rsc Advances, 2012. **2**(1): p. 344-350.
10. Pol, V.G., J.M. Calderon-Moreno, and P. Thiyagarajan, *Facile synthesis of novel photoluminescent ZnO micro-and nanopencils.* Langmuir, 2008. **24**(23): p. 13640-13645.
11. Nur Syafinaz, R., et al., *Formation of ZnO nanorods via seeded growth hydrothermal reaction.* Applied Mechanics and Materials, 2011. **83**: p. 116-122.
12. Hodoroaba, V.-D., *Energy-dispersive X-ray spectroscopy (EDS)*, in *Characterization of Nanoparticles*. 2020, Elsevier. p. 397-417.
13. Hatch, S., et al., *Influence of anneal atmosphere on ZnO-nanorod photoluminescent and morphological properties with self-powered photodetector performance.* Journal of Applied Physics, 2013. **113**(20).
14. Decremps, F., et al., *High-pressure Raman spectroscopy study of wurtzite ZnO.* Physical Review B, 2002. **65**(9): p. 092101.

15. Khan, A., S.N. Khan, and W.M. Jadwisienczak, *One step growth of ZnO nano-tetrapods by simple thermal evaporation process: structural and optical properties.* Science of Advanced Materials, 2010. **2**(4): p. 572-577.
16. Arguello, C., D.L. Rousseau, and S.d.S. Porto, *First-order Raman effect in wurtzite-type crystals.* Physical Review, 1969. **181**(3): p. 1351.
17. Klingshirn, C.F., et al., *Crystal structure, chemical binding, and lattice properties.* Zinc Oxide: From Fundamental Properties Towards Novel Applications, 2010: p. 7-37.
18. Khan, A., *Raman spectroscopic study of the ZnO nanostructures.* J Pak Mater Soc, 2010. **4**(1): p. 5-9.
19. Ahmed, B., et al., *Facile and controlled synthesis of aligned WO3 nanorods and nanosheets as an efficient photocatalyst material.* Spectrochimica Acta Part A: Molecular and Biomolecular Spectroscopy, 2017. **175**: p. 250-261.
20. Yin, H., et al., *Controlled synthesis of ultrathin ZnO nanowires using micellar gold nanoparticles as catalyst templates.* Nanoscale, 2013. **5**(15): p. 7046-7053.
21. Pokropivny, V., et al., *Introduction to nanomaterials and nanotechnology*. 2007: Tartu University Press Ukraine.
22. Law, M., J. Goldberger, and P. Yang, *Semiconductor nanowires and nanotubes.* Annu. Rev. Mater. Res., 2004. **34**: p. 83-122.
23. Lupan, O., et al., *PdO/PdO 2 functionalized ZnO: Pd films for lower operating temperature H 2 gas sensing.* Nanoscale, 2018. **10**(29): p. 14107-14127.
24. Zargar, R.A., *Fabrication and improved response of ZnO-CdO composite films under different laser irradiation dose.* Scientific Reports, 2022. **12**(1): p. 10096.
25. Zhang, R., et al., *Photoluminescence and Raman scattering of ZnO nanorods.* Solid State Sciences, 2009. **11**(4): p. 865-869.
26. Xu, H., et al., *Effects of annealing ambient on oxygen vacancies and phase transition temperature of VO 2 thin films.* RSC advances, 2016. **6**(83): p. 79383-79388.
27. Song, Y., et al., *Raman spectra and microstructure of zinc oxide irradiated with swift heavy ion.* Crystals, 2019. **9**(8): p. 395.
28. Majumder, S., et al., *Investigations on solution derived aluminium doped zinc oxide thin films.* Materials Science and Engineering: B, 2003. **103**(1): p. 16-25.
29. Das, A. and D. Basak, *Efficacy of ion implantation in zinc oxide for optoelectronic applications: A review.* ACS Applied Electronic Materials, 2021. **3**(9): p. 3693-3714.
30. Bechambi, O., et al., *Effect of cerium doping on the textural, structural and optical properties of zinc oxide: role of cerium and hydrogen peroxide to enhance the photocatalytic degradation of endocrine disrupting compounds.* Materials Science in Semiconductor Processing, 2015. **39**: p. 807-816.

31. Vinitha, V., et al., *Two is better than one: Catalytic, sensing and optical applications of doped zinc oxide nanostructures.* Emergent Materials, 2021. **4**: p. 1093-1124.

CHAPTER 5- GAS SENSING APPLICATION

5.1 INTRODUCTION

This chapter reports on the responses to target gases at different operating temperatures as well as the sensing materials' ideal working temperature. The ZnO, 0.2%Pd-ZnO, 0.3%Pd-ZnO, 0.5%Pd-ZnO and 0.7%Pd-ZnO sensors were tested towards Ethanol, NO_2, SO_2, CO_2 at a resistance of 100 Ohms. The ZnO sensor did not detect these gases because of overloading, which is due to high resistance. Surface saturation on ZnO leads to reduced gas absorption and lowers the sensor's sensitivity**[1]**. Overloading the sensor can result in decreased selectivity, causing it to favour certain gases and potentially yield inaccurate readings**[2]**. Agglomeration of ZnO particles, driven by excessive concentration, reduces the available surface area for gas interaction, impacting sensor performance**[1]**. Diffusion restrictions caused by overloaded ZnO layers make it harder for gas molecules to access active sites, further diminishing sensitivity**[3]**. Overall, these factors collectively contribute to compromised gas sensing capabilities in the presence of surface saturation and overloaded ZnO layers.

Gas sensitivity is the most significant parameter mechanism and is useful for the chemically resistant MO performance**[4]**. Since electron affinity which is related to the work function of most metal oxides is linked to oxidizing or reducing gas, the adsorbed gas molecules in the case of oxidizing gas are anions on the surface of the MO**[5]**. Table 5.1 below displays the sensitivity measurements of different materials.

Two possible explanations for the change in electrical resistance of semiconductors are the energy band bending and the creation of the space-charge depletion zone surrounding and on the surface of the particle**[6]**. Surface energy barriers that vary in height and width are contingent upon the correlation between the charging of the adsorbed species' surface states and conduction electrons**[7]**. It has been noted that in gas sensors that use n-type semiconductor metal oxide, the resistance of the metal oxide increases when gases like O_3 or NO_2 interact with it, whereas the resistance of the oxide decreases when gases like CH_4 and CO_2 interact with it, table 5.1 summarises this behaviour**[8]**.

***Table 5. 1**: The Sensitivity measurement of material type and target gas type**[4]**.*

TYPE OF SENSITIVE MATERIAL	**TYPE OF AIMED GAS**	**RESPONSE(S)**
n-type	- oxidizing - reducing	R_g/R_a R_a/R_g
p-type	-oxidizing -reducing	R_a/R_g R_g/R_a

5.2 Fabrication of a sensor

The hydrothermal prepared ZnO, 0.2%Pd-ZnO, 0.3%Pd-ZnO, 0.5%Pd-ZnO and 0.7%Pd-ZnO powders were each transferred to a different small container using a spatula, after adding ethanol to each powder sample, they were sonicated. After that, the solutions were drop-casted onto an alumina substrate that had platinum electrodes screen-printed on it with a melting point of 1768°C as shown in figure 5.1. The fabricated ZnO and Pd-ZnO sensor's sensing layer were set to air dry at room temperature for the whole night. To achieve a sensing measurement, the sensors were concurrently put in an airtight chamber equipped with electrical and gas supplies. The performance of the fabricated sensors' gas detection was evaluated using the University of the Free State's gas testing system inside the KSGAS6S gas sensing station (KENOSISTEC, Italy). The ZnO sensor device was placed in a climatic gas testing chamber. A bias voltage of 5 V was supplied across the sensor terminals while dry air was first injected into the chamber to allow the sensor to reach equilibrium. Following the initial setup, the ZnO, 0.2%Pd-ZnO, 0.3%Pd-ZnO, 0.5%Pd-ZnO and 0.7%Pd-ZnO sensor devices were used to detect Ethanol, $\mathrm{NO_2}$, $\mathrm{SO_2}$, $\mathrm{CO_2}$ at various concentrations and temperatures (25°C, 75°C, 150°C, 200°C, and 225°C).

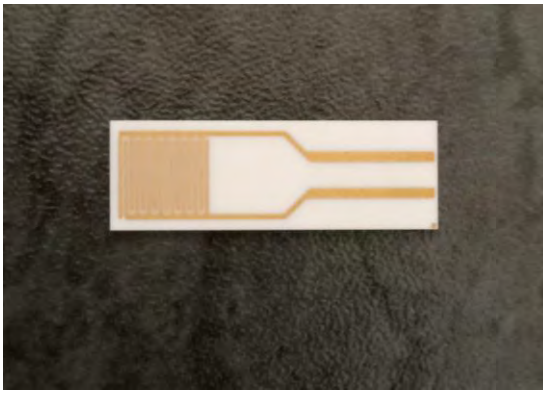

***Figure 5. 1**: Heat-able alumina substrate with platinum screen-printed heater (left) and electrodes (on the right).*

The optimal temperature for 0.2%Pd-ZnO, 0.3%Pd-ZnO, 0.5%Pd-ZnO and 0.7%Pd-ZnO based sensor devices, was found to be 150°C regarding NO_2 and Ethanol. When the sensors were exposed to reducing gases, the operating temperature was 25°C. The response was calculated using the equations in table 5.1 and recovery times of the sensors were also determined.

5.3 Pd-ZnO based gas sensor at Optimal temperature.

It is commonly known that the gas detection capabilities of Pd-ZnO gas sensors are significantly impacted by the operating temperature. All the fabricated sensors, namely 0.2%Pd-ZnO, 0.3%Pd-ZnO, 0.5%Pd-ZnO and 0.7%Pd-ZnO were used in the sensing tests to determine the ideal operating temperature. The tested gases towards these sensors are Ethanol, NO_2, SO_2, and CO_2. The optimal temperature was found to be 150°C and the two gases which responded at this temperature were NO_2 and ethanol. Ethanol is a reducing gas; may both oxidize and provide electrons to reduce other substances**[9]**. NO_2 is also an oxidizing gas**[9, 10]**. The summary of these gases' best behaviour toward Pd-ZnO at different concentrations of Pd is listed in table 5.2, operation temperature and concentration of gases. Figure 5.2 shows the plots of NO2 and ethanol behaviour at optimal temperature towards Pd doped ZnO sensors.

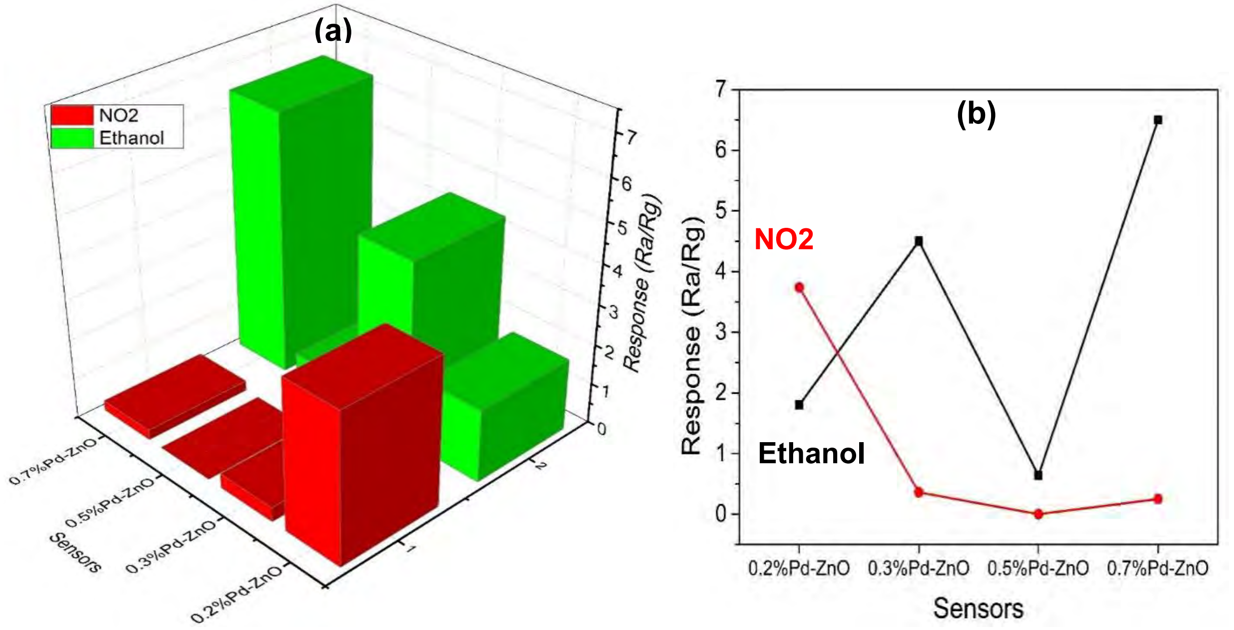

Figure 5. 2: *(a)The 3D graph of the sensor's vs response and gases (b) Line graph of sensors vs response of the gases at optimal temperature.*

The relation between various sensors and the sensors' response to 1.5-45 ppm of ethanol and 15-450 ppm of NO2 at optimal operating temperature is depicted in figure 5.2 (a) and figure 5.2 (b) respectively. The $\mathrm{NO_2}$ gas response decreases as the sensor variation concentration of Pd decreases, whereas from Ethanol it is increasing. The 0.5%Pd-ZnO sensor has the smallest response to all gases, 0.2%Pd-ZnO is the highest to $\mathrm{NO_2}$ and 0.7%Pd-ZnO is the highest to Ethanol.

5.4 Pd-ZnO Base Sensors of Ethanol at Optimal temperature

Furthermore, response and recovery characterisations are important aspects to consider when assessing ethanol sensor performance. All the fabricated sensors were subjected to 45 ppm ethanol at 150°C to compare the response-recovery behaviours. The observed response curves are displayed in Fig. 5.3 (A, B, C and D). The observed findings show that, in comparison to other sensors, the 0.7%Pd-ZnO sensor responds to ethanol more strongly.

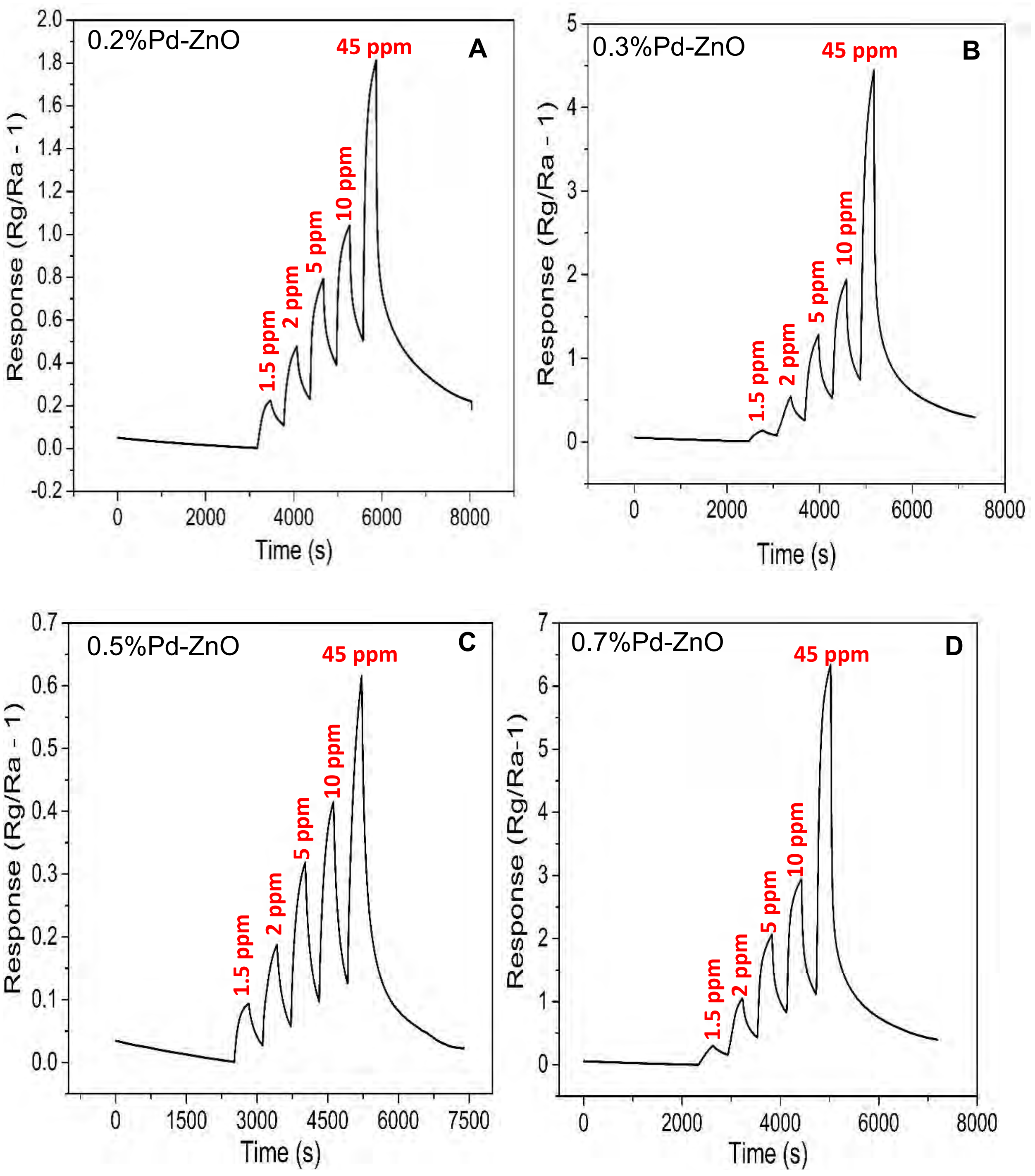

***Figure 5. 3** Gas sensing performance **A** 0.2%Pd-ZnO, **B** 0.3%Pd-ZnO, **C** 0.5%Pd-ZnO, and **D** 0.7%Pd-ZnO: towards Ethanol and at the same concentration.*

At a working temperature of 150°C, Figure 5.3 displays the typical dynamic response/recovery curves of the as-fabricated sensors to ethanol at concentrations ranging from 1.5 to 45 ppm. It is evident that all the fabricated sensors have a distinct and quick response that increases as the concentration of ethanol gas rises, and that the low detection limit of ethanol can reach 1.5 ppm. The resistances of the Pd-ZnO sensors did not return to their starting values after several cycles between exposure to ethanol gas and fresh air, indicating that all the manufactured sensors exhibit partial reversibility and remarkable repeatability. According to the experimental results, 0.7%Pd/ZnO sensors exhibit a faster reaction rate than other Pd-ZnO sensors, indicating the superiority of these sensors over the 0.2%Pd-ZnO, 0.3%Pd-ZnO and 0.5%Pd-ZnO sensor at varying ethanol concentrations. It is discovered that the reactions are almost proportionate to the rising ethanol concentration from the curves when the concentrations are further increased. According to the mentioned findings, the 0.7%Pd-ZnO sensor holds great promise for ethanol detection. According to these findings, the 0.7%Pd-ZnO sensor can detect ethanol vapors selectively and without interference from other gases since it is more sensitive to ethanol than other target gases. This is clearly observed in figure 5.3 D. The concentration with the greatest response on 0.7%Pd-ZnO is 45 ppm with a response time of 3.1 minutes, recovery time of 2.8 minutes. This concentration was plotted against all tested temperatures for this sensor in figure 5.4.

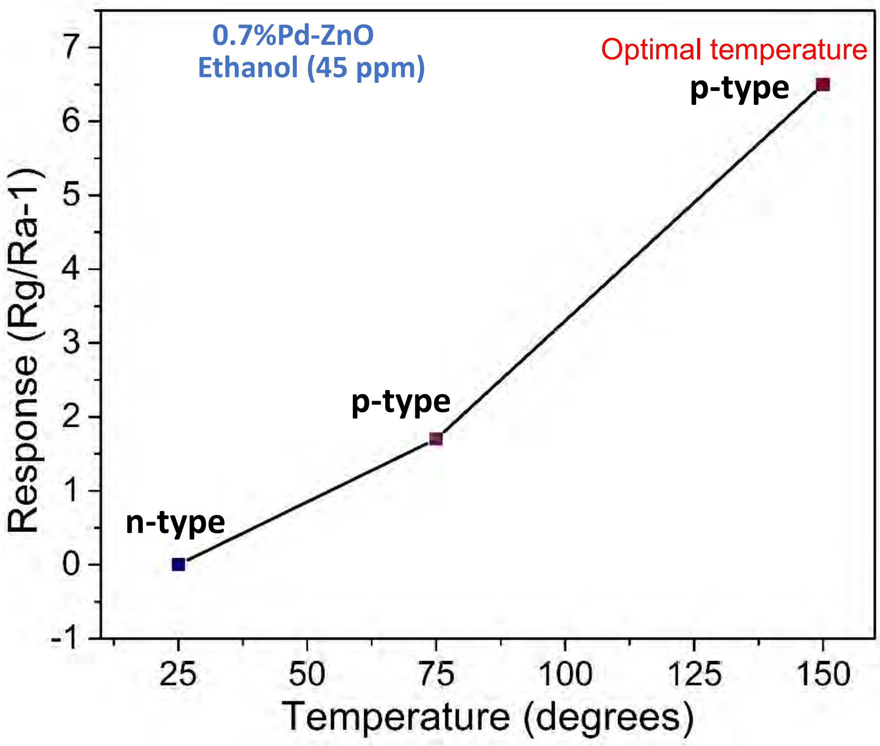

***Figure 5. 4**: Graph of the 0.7%Pd-ZnO highest performing sensor, concentration of 45 ppm at all tested temperatures including optimal temperature.*

5.5 Pd-ZnO Base Sensors of NO2 at Optimal temperature

Sensors 0.2%Pd-ZnO, 0.3%Pd-ZnO, 0.5%Pd-ZnO and 0.7%Pd-ZnO are not good for oxidizing gases at low temperatures. This is because of the electrical effect, which causes resistance to reduce more when exposed to reducing gases than to slightly rise when exposed to oxidizing gases, strengthening the sensor's reaction to reducing gases**[11]**. The 0.2%Pd-ZnO sensor is the optimal sensing concentration further increase above this concentration result in an undefined patten as figure 5.5 (A) illustrate. This sensor is an n-type, and it remains the only n-type material because it has the smallest Pd content. Higher doped material like 0.3%Pd-ZnO, 0.5%Pd-ZnO and 0.7%Pd-ZnO changed to p-type since we doped with acceptor impurity which is Pd. This sensor reaches a detection limit at 300 ppm for the highest response of 3.8, with a response time of 3.5 minutes and recovery time of 3.5 minutes .

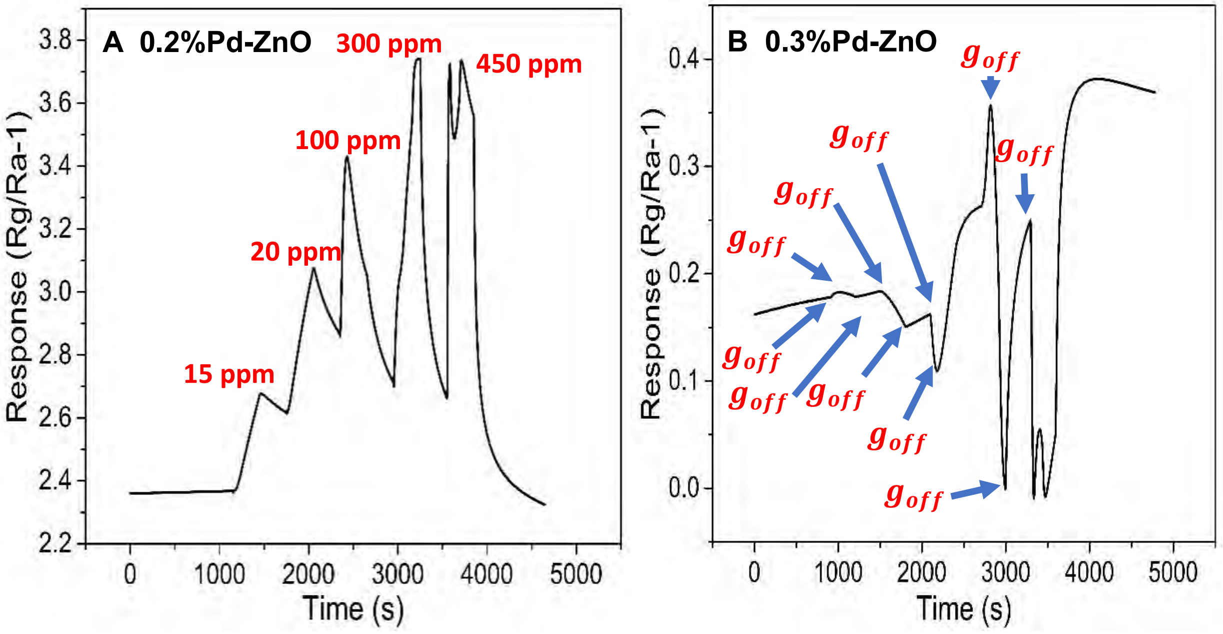

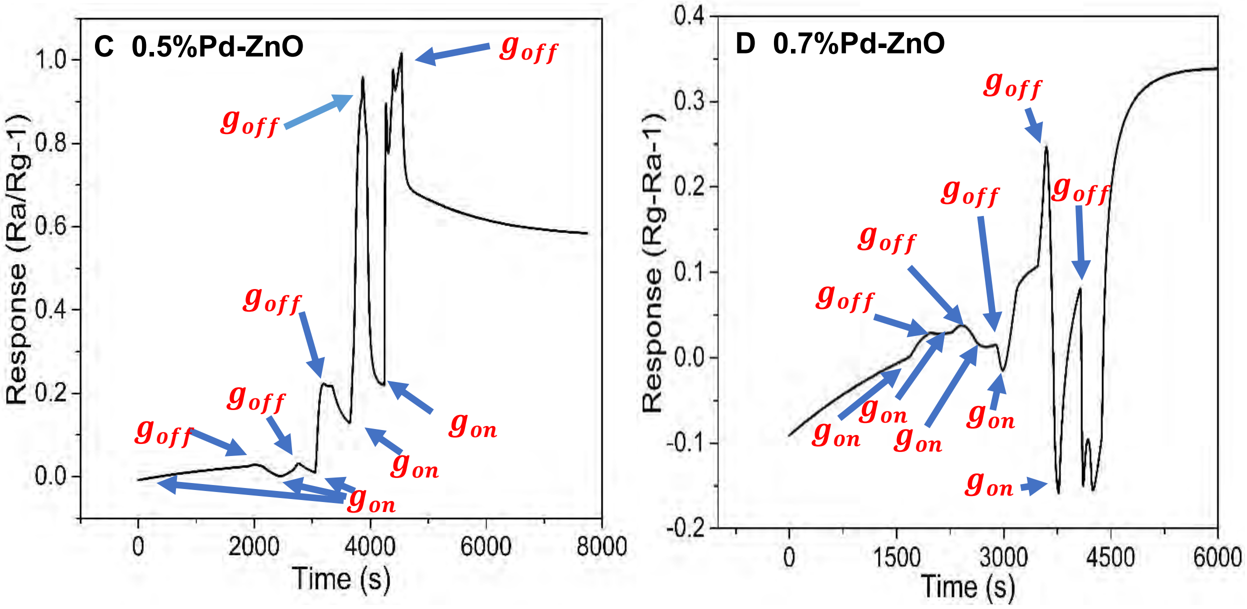

Figure 5. 5 *Gas sensing performance* ***A*** *0.2%Pd-ZnO,* ***B*** *0.3%Pd-ZnO,* ***C*** *0.5%Pd-ZnO, and* ***D*** *0.7%Pd-ZnO****:*** *towards* NO_2 *at the same concentrations.*

5.6 Sensitivity at optimal temperature

The sensor's sensitivity is indicated by the response vs. concentration curve's slope in figure 5.6. Higher sensitivity is shown by a steeper slope, which means that changes in gas concentration cause the sensor to react more strongly. For the ethanol plots in figure 5.6 (a) the 0.7%Pd-ZnO is more sensitive to ethanol gas since it has the steepest slope. This may be due to increased surface reactivity which is the adsorption and desorption of ethanol gas molecule on the surface of a sensor. The sensor with a great sensitivity in $\mathrm{NO_2}$ gas is 0.2%Pd-ZnO as observed in figure 5.6 (b), this is due to the enhanced catalytic activity which is promoted by Palladium as it is a good catalyst that can increase the material's catalytic activity and speed up the reaction between the sensing material and the target oxidizing gas.

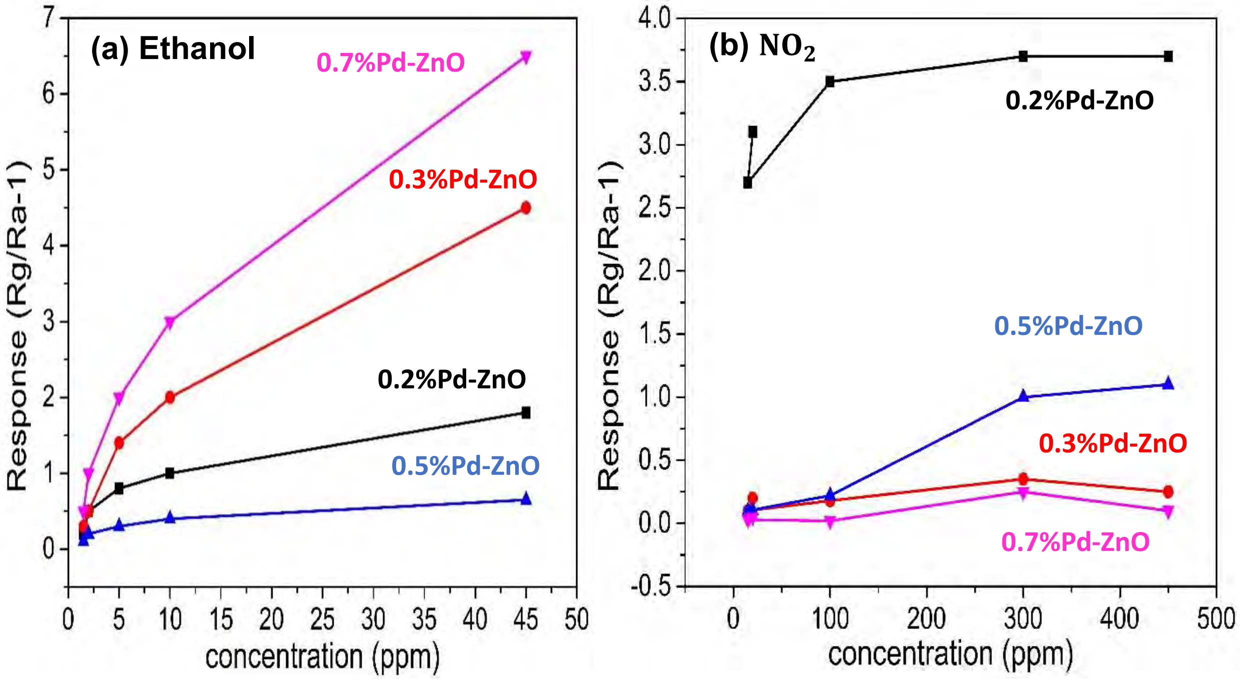

Figure 5. 6: *(a) Ethanol sensitivity line graphs of sensors responses vs concentrations, and (b) NO_2 sensitivity graph of sensors response vs concentrations.*

5.7 Low temperature sensing towards Reducing gases.

The response varies for all Pd-ZnO sensors as Pd content increases, reaches a maximum response of 0.5 at 0.5%Pd-ZnO sensor, the trend is decreasing from 0.2%Pd-ZnO to 0.3%Pd-ZnO and from 0.5%Pd-ZnO to 0.7%Pd-ZnO as shown in figure 5.7. The optimal sensing concentration is 0.5%Pd-ZnO, SO_2 is the gas with the highest response at this sensor. Reducing gases are a good candidate at room temperature because of the chemical process that happens when the counterpart material in the composite structured sensor for the oxidation reaction has better catalytic activity, leading to increased oxidation of reducing gasses**[12]**. The 0.7%Pd-ZnO sensor has the lowest response of all the three gases at 25°*C.*

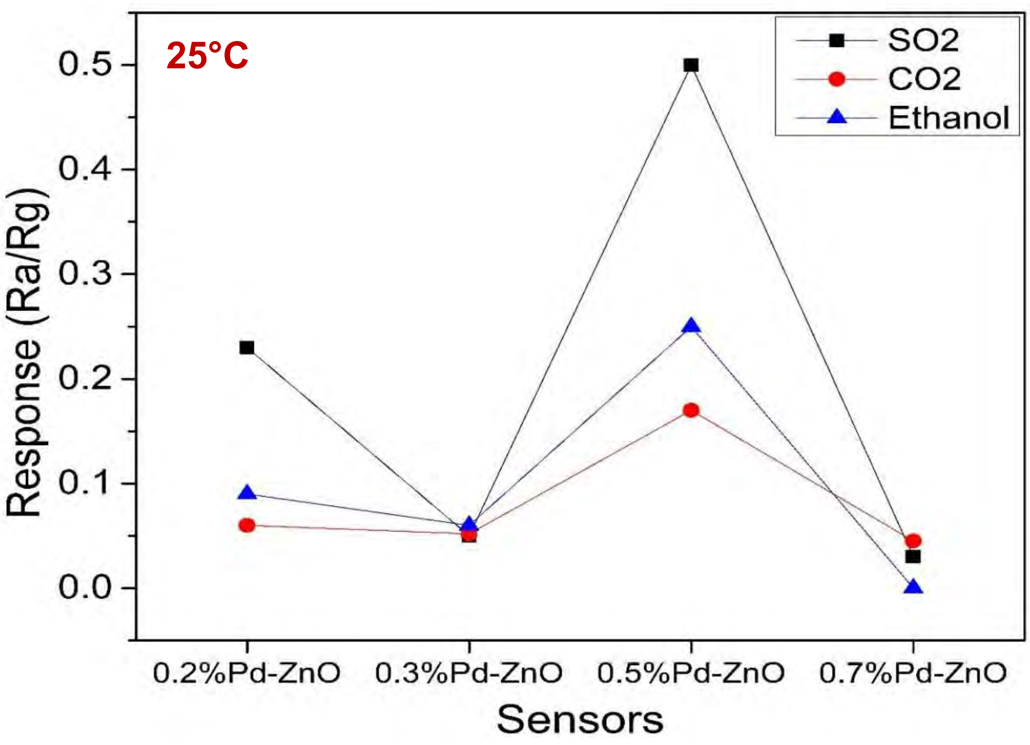

***Figure* 5. 7**: *The Plot of the sensors vs response towards reducing gases at room temperature (25°C).*

5.7.1 RT sensing towards 0.5%Pd-ZnO sensor.

The semiconductor materials have a lower conductivity at lower temperatures, while the resistance of 0.5%Pd-ZnO is high at room temperature (see figure 5.8 A, B, C, D, E and F). This increase in resistance at room temperature is the result of the interaction of the semiconductor material's surface with the molecules of the target gas. Also, the adsorption and desorption of gas molecules on the semiconductor material's surface become more dynamic at higher temperatures, which is why sensing happens at room temperature. There is an increased charge Carrier mobility at room temperature, material's conductivity is altered when the temperature is increased. Elevated temperatures have the potential to enhance the mobility of charge carriers, such as electrons or holes, within the semiconductor, hence promoting the decrease of resistance. The lower the temperature the higher the resistance for the reducing gases SO_2, CO_2 and ethanol. Specifically, this sensor 0.5%Pd-ZnO is the best candidate for low temperature sensing. Most sensors require thermal activation which is increasing the temperature to promotes more efficient interactions between the sensor material and gas molecules, but this sensor does not require any activation on sensing reducing gases. In figure 5.8 (A, B, C, D, E and F) the survey of the gas resistance at all temperatures is shown, followed by the gas response at room temperature.

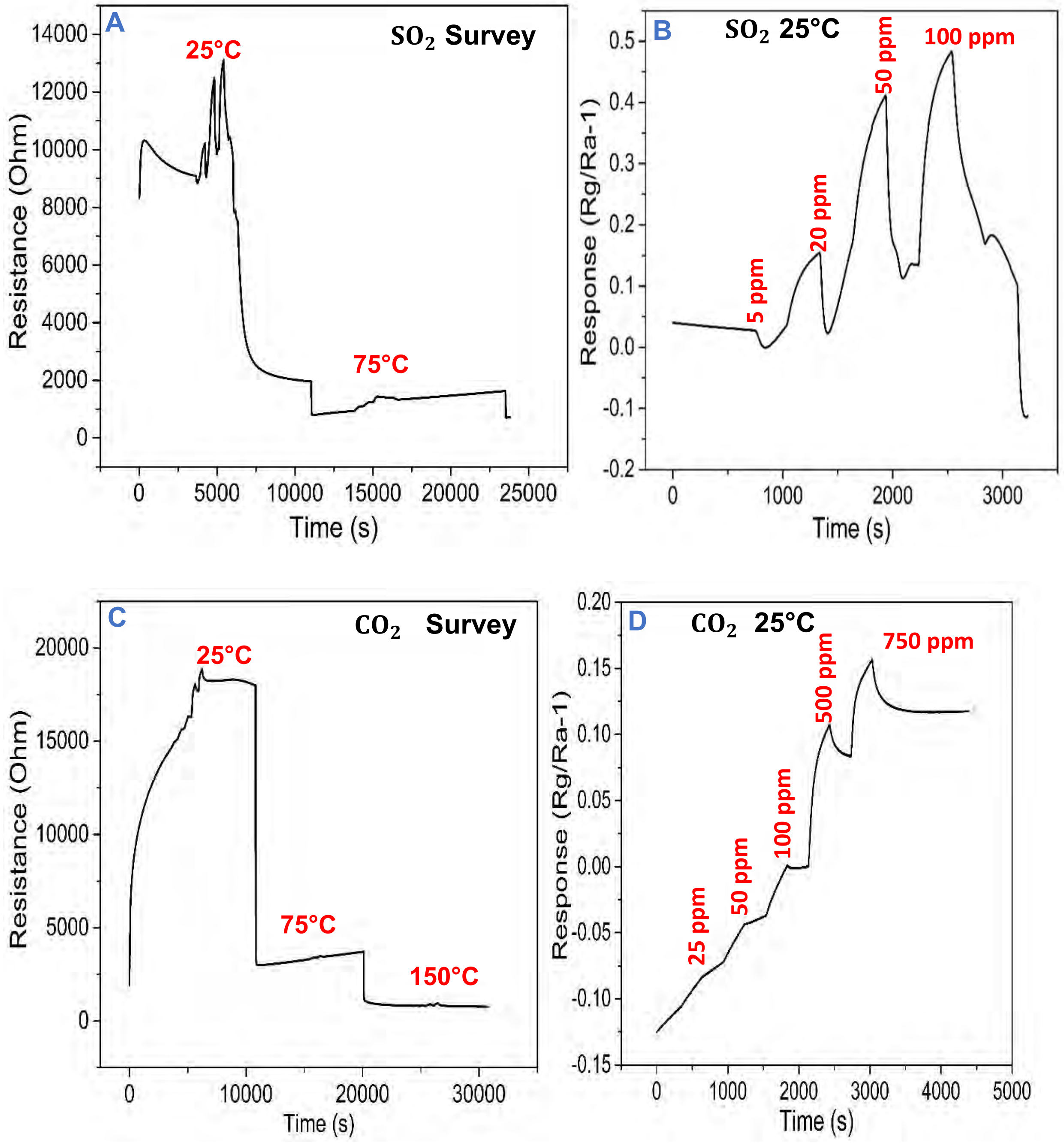

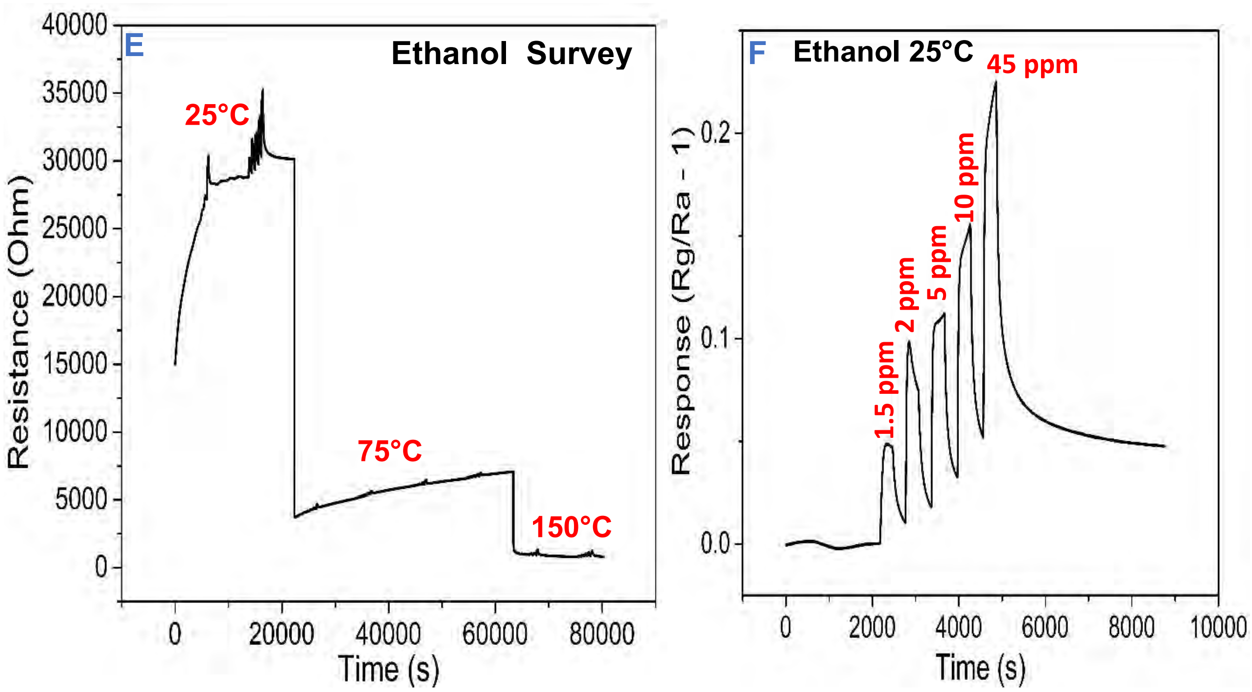

***Figure 5. 8**: The **A** SO_2 survey at 25°C, and 75°C temperatures, **B** shows SO_2 at sensing temperature of 25°C, **C** shows CO_2 survey at 25°C, 75°C and 150°C temperature, **D** shows CO_2 at the sensing temperature of 25°C, **E** shows ethanol survey plot at 25°C, 75°C and 150°C temperature, and **F** shows the ethanol sensing at room temperature.*

This sensor is good for low temperature sensing towards reducing gases, while CO_2 has only sense at 25°C as shown in figure 5.8 (**D** & **E**) and we see a big drop in resistance as the temperature increases. CO_2 has the highest response of 0.175 at a concentration of 750 ppm with a response time of 3.15 minutes and recovery time of 1.9 minutes. SO_2 gas follows the same trend. This gas was tested from 25°C to higher temperature but only responded to 25°C after that we see a drastic drop in resistance as the temperature increases, (see figure 5.8 **A** & **B**). SO_2 gas was exposed to the sensor in 5 different concentrations namely 5 ppm, 20 ppm, 50 ppm, 100 ppm and 120 ppm, but only the first four concentrations responded which means the sensor sensitivity range is reached at 100 ppm concentration and further increases in concentration result in no response. The highest response is 0.5 at 100 ppm with a response time of 5.6 minutes and a recovery time of 4.1 minutes. At 75°C temperature SO_2 gas did not sense at all; this is due to the low temperature characteristics of this sensor. Palladium is recognised for its catalytic activity, and its presence on the ZnO surface increases the gas-sensing characteristics of the material. Ethanol also shows good behaviour at room temperature where it has a response of 0.25 at 45 ppm with a response time of 3 minutes and a recovery time of 2.7 minutes. All these sensors recover faster than responding to these gases at room temperature. Pd-ZnO promotes the interaction between the target gases (SO_2, CO_2, ethanol) and the sensing material, resulting in a more substantial change in electrical properties. The presence of Pd also enhances the sensitivity of the material to sense (SO_2, CO_2, ethanol) at low concentrations compared to the literature**[4]**, which is difficult but crucial for accurate and reliable gas sensing. In practical applications where maintaining a certain working temperature may be difficult or undesirable, the Pd-ZnO sensor frequently shows acceptable stability and performance at moderate temperatures, such as 25 °C.

5.8 High Temperature Sensing towards Oxidizing Gas

The oxidizing gas NO_2 needs a thermal activation which is a high temperature for the sensor material to interact with the gas. For precise target gas concentration measurement, the linear range is necessary. At these concentrations, 0.2%Pd-ZnO, 0.3%Pd-ZnO and 0.7%Pd-ZnO sensors behaved non-linearly. These sensors reach a saturation point at 300 ppm, meaning the sensor's capacity to detect the gas has been fully used. We see a decrease in resistance and response at the highest concentration of 450 ppm. When the gas concentration varies, we observe the sensor's reversible response, which happens when the gas is withdrawn. The resistance reverts to its baseline, ensuring accurate and consistent data. The 0.2%Pd-ZnO is an n-type, and the rest are p-type. The behaviour of these sensors at 200°C and 225°C towards NO_2 gas is the same, the difference being the response which increases with the increase in temperature except for the 0.5%Pd-ZnO sensor.

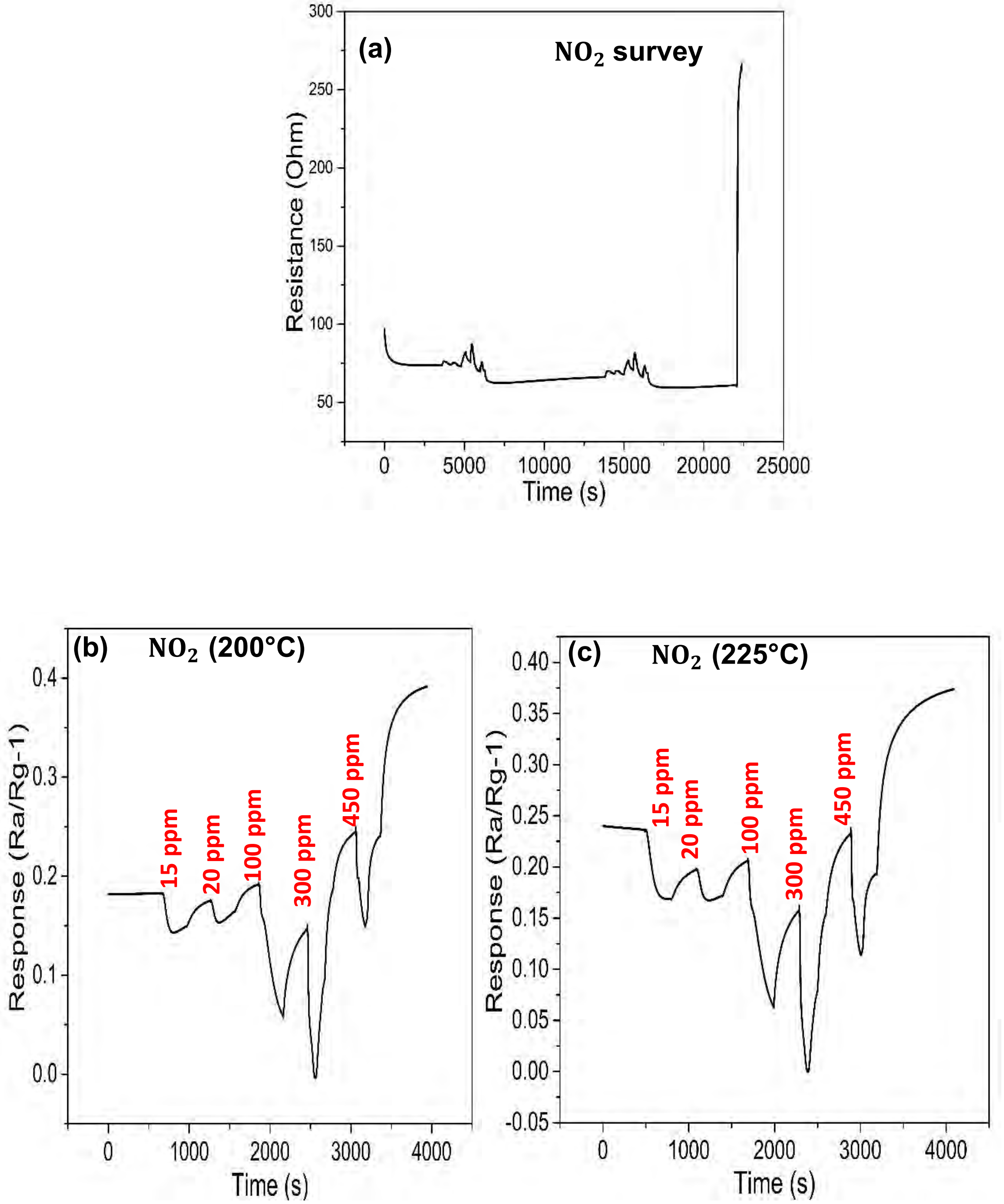

***Figure 5. 9**: NO_2 gas (a) survey graphs for the rate of resistance, rate of response (b) 0.2%Pd-ZnO at 200°C and (c) 0.2%Pd-ZnO at 225°C.*

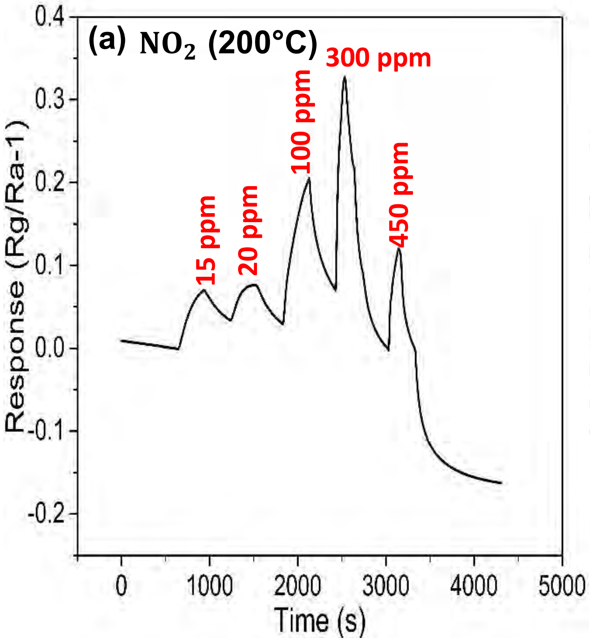

***Figure 5. 10**: NO_2 response vs time graph of (a) 0.3%Pd-ZnO at 200°C and (b) 0.3%Pd-ZnO at 225°C*

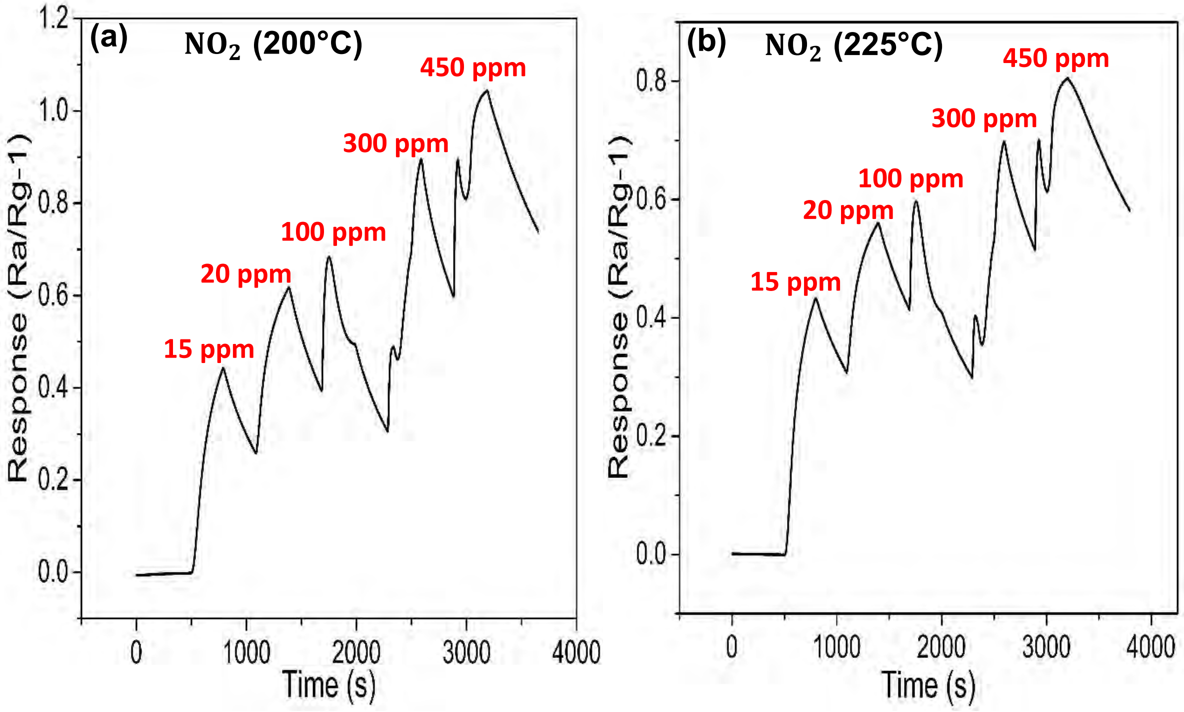

***Figure 5.12**: NO_2 response vs time graph of (a) 0.5%Pd-ZnO at 200°C and (b) 0.5%Pd-ZnO at 225°C.*

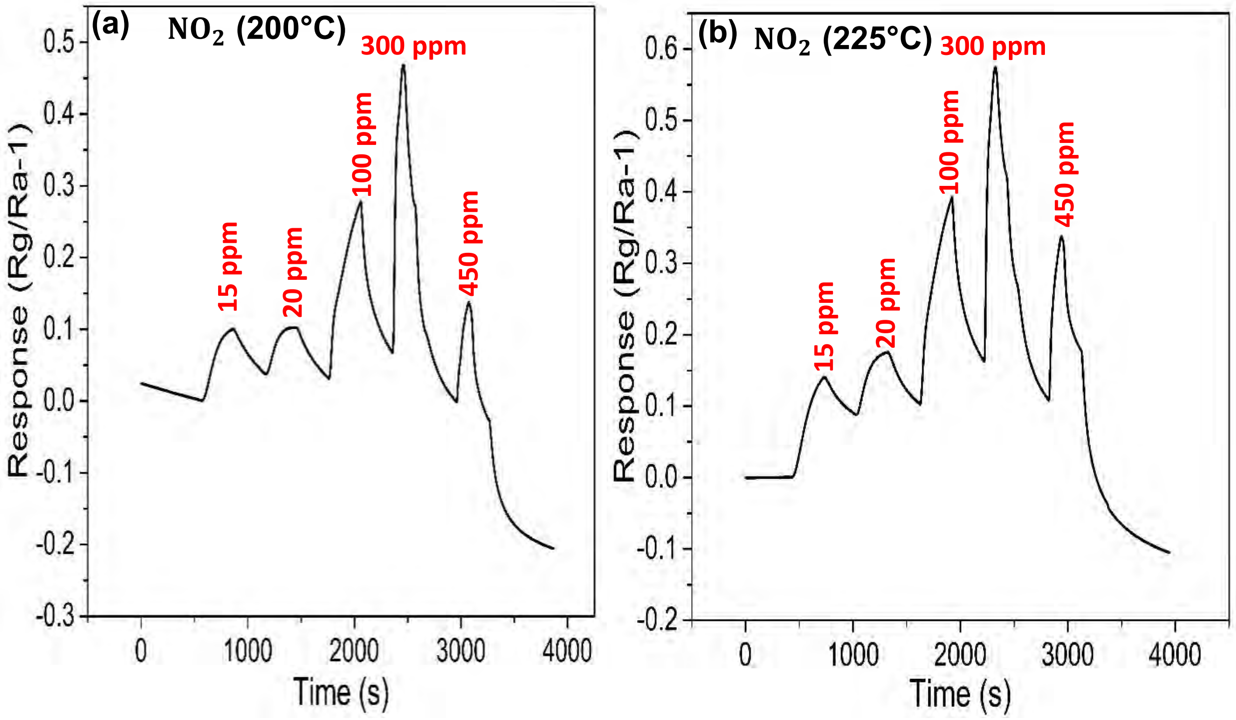

Figure 5.13: *NO_2 response vs time graph of (a) 0.7%Pd-ZnO at 200°C and (b) 0.7%Pd-ZnO at 225°C.*

The highest response to 0.2%Pd-ZnO, 0.3%Pd-ZnO and 0.7%Pd-ZnO is at 300 ppm, whereas in 0.5%Pd-ZnO it is at 450 ppm (as shown in figure 5.11). The 0.5%Pd-ZnO sensor behave differently compared to all other sensors, it is the one which has highest response at highest concentrations in both temperature of 200°C and 225°C. The highest response at 200°C is 1.1 with a response time of 3.3 minutes and recovery time of 3.4 minutes. At 225°C it is 0.8 with a response time of 2.8 minutes and recovery time of 6 minutes. A longer recovery time may result from the creation of stable intermediates on the sensor surface, whose desorption can happen more slowly. The process of desorption, in which NO_2 molecules separate from the sensor surface, occurs more slowly, leading to a prolonged recovery period.

***Table 5. 2**: The recent papers on detection of NO_2, SO_2, ethanol and CO_2 gases toward Pd-ZnO.*

MATERIAL	**ANALYTE**	**CONCENTRATION**	**TEMPERATURE (°C)**	**RESPONSE**	**REF.**
1mol% Pd@ZnOWs	$\mathrm{NO_2}$	1 ppm	100	13.5	**[13]**
Pd decorated ZnO Nanorods	Ethanol	1530 ppm	200	94	**[14]**
Ni-ZnO nanocomposite	$\mathrm{CO_2}$	2000 ppm	25	3.75	**[15]**
ZnO nanostructures	$\mathrm{SO_2}$	10 ppm	200	8.28	**[16]**
0.2%Pd-ZnO Nanorods	$\mathrm{NO_2}$	300 ppm	150	3.74	**This work**
0.7%Pd-ZnO nanorods	Ethanol	45 ppm	150	6.5	**This work**
0.5%Pd-ZnO nanorods	$\mathrm{CO_2}$	750 ppm	25	0.175	**This work**
0.5%Pd-ZnO nanorods	$\mathrm{SO_2}$	120 ppm	25	0.5	**This work**
0.5%Pd-ZnO Nanorods	$\mathrm{NO_2}$	450 ppm	200	1.1	**This work**
0.5%Pd-ZnO Nanorods	$\mathrm{NO_2}$	450 ppm	225	0.8	**This work**
0.7%Pd-ZnO nanorods	Ethanol	45 ppm	75	1.6	**This work**
0.5%Pd-ZnO Nanorods	Ethanol	45 ppm	25	0.25	**This work**

5.9 Gas sensing mechanism of the sensor

Various studies have demonstrated that the material and the concentration of chemisorbed oxygen density on the surface area of semiconductor oxide nanostructures are the main determinants of gas sensor performance**[17]**. Oxygen molecules on the sensor surface typically capture electrons from the conduction band when exposed to air, creating a depletion layer**[18]**. The ZnO sensitive unit's resistance decreased because of oxygen species reacting with the sensor in the presence of ethanol vapour and releasing electrons into the conduction band**[19]**.

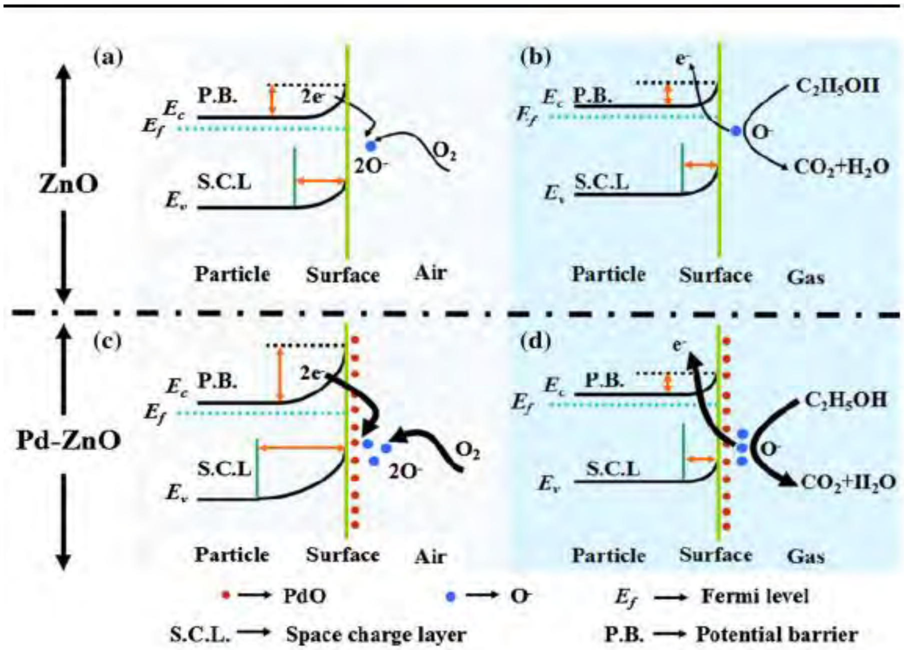

Figure 5.14**: Schematic band diagrams of ZnO and Pd-ZnO exposed to ambient **(a)** air and **(b)** ethanol gas, respectively, and to ambient **(c)** air and **(d)** ethanol gas, respectively[19]**.*

First, the well-known spillover effect explains the gas sensing process, Palladium causes the molecular oxygen on the surface of ZnO-sensitive material to dissociate more readily, increasing the depletion layer's width. Second, based on the Pd/ZnO sensitive material**[20]**. The heterojunction formed at the ZnO and PdO interface (p-type semiconductor) significantly enlarged the space charge layer near the interface. The amplified depletion layer started rapidly disappear when the sensors were placed in an ethanol vapour atmosphere, which led to a greater change in the resistance of the sensor and additional improvement in the response value**[21]**. Stated differently, the palladium addition may accelerate the pace of reaction with the adsorbed oxygen. A too high percentage of Pd content can suppress the gas sensing properties by decreasing the effective surface adsorption area, whereas an appropriate concentration of palladium can greatly improve the gas sensing properties.**[21]**.

6.0 References

1. Chaudhary, S., et al., *Chemical sensing applications of ZnO nanomaterials.* Materials, 2018. **11**(2): p. 287.
2. Rehman, A. and X. Zeng, *Methods and approaches of utilizing ionic liquids as gas sensing materials.* RSC advances, 2015. **5**(72): p. 58371-58392.
3. Potyrailo, R.A., et al., *Materials and transducers toward selective wireless gas sensing.* Chemical reviews, 2011. **111**(11): p. 7315-7354.
4. Bochenkov, V. and G. Sergeev, *Sensitivity, selectivity, and stability of gas-sensitive metal-oxide nanostructures.* Metal oxide nanostructures and their applications, 2010. **3**: p. 31-52.
5. Pacchioni, G., *Electronic interactions and charge transfers of metal atoms and clusters on oxide surfaces.* Physical Chemistry Chemical Physics, 2013. **15**(6): p. 1737-1757.
6. Mönch, W., *Semiconductor surfaces and interfaces*. Vol. 26. 2013: Springer Science & Business Media.
7. Tsoi, V., J. Bass, and P. Wyder, *Studying conduction-electron/interface interactions using transverse electron focusing.* Reviews of Modern Physics, 1999. **71**(5): p. 1641.
8. Dey, A., *Semiconductor metal oxide gas sensors: A review.* Materials science and Engineering: B, 2018. **229**: p. 206-217.
9. Tiwary, P., et al., *Room temperature ethanol sensing by chemically reduced graphene oxide film.* FlatChem, 2021. **30**: p. 100317.
10. Li, Q., W. Zeng, and Y. Li, *Metal oxide gas sensors for detecting NO2 in industrial exhaust gas: Recent developments.* Sensors and Actuators B: Chemical, 2022. **359**: p. 131579.
11. Choi, S.-B., et al., *Enhanced NO 2 gas-sensing performance of Pd/ZnO-codecorated SnO 2 nanorod sensors.* Applied Physics A, 2018. **124**: p. 1-9.
12. Park, S., et al., *UV-enhanced NO2 gas sensing properties of SnO2-core/ZnO-shell nanowires at room temperature.* ACS applied materials & interfaces, 2013. **5**(10): p. 4285-4292.
13. Chen, X., et al., *NO2 sensing properties of one-pot-synthesized ZnO nanowires with Pd functionalization.* Sensors and Actuators B: Chemical, 2019. **280**: p. 151-161.
14. Roy, S., et al., *Development of an ethanol sensor based on CBD grown ZnO nanorods.* Solid-State Electronics, 2013. **87**: p. 43-50.
15. Kumar, V., et al., *Environment-sensitive and fast room temperature CO2 gas sensor based on ZnO, NiO and Ni-ZnO nanocomposite materials.* Environmental Functional Materials, 2023.
16. Cao, L., et al., *In-situ growth of well-ordered ZnO nanowire-networks with interconnected junctions for enhanced SO2 gas sensing properties.* Applied Surface Science, 2024. **646**: p. 158899.

17. Liang, Y.-C., W.-K. Liao, and X.-S. Deng, *Synthesis and substantially enhanced gas sensing sensitivity of homogeneously nanoscale Pd-and Au-particle decorated ZnO nanostructures.* Journal of alloys and compounds, 2014. **599**: p. 87-92.
18. Rai, P., W.-K. Kwak, and Y.-T. Yu, *Solvothermal synthesis of ZnO nanostructures and their morphology-dependent gas-sensing properties.* ACS applied materials & interfaces, 2013. **5**(8): p. 3026-3032.
19. Hu, J., et al., *Optimization of Pd content in ZnO microstructures for high-performance gas detection.* Journal of Materials Science, 2015. **50**: p. 1935-1942.
20. Lin, Y., et al., *Room-temperature self-powered ethanol sensing of a Pd/ZnO nanoarray nanogenerator driven by human finger movement.* Nanoscale, 2014. **6**(9): p. 4604-4610.
21. Ge, C., et al., *Structural characteristics and UV-light enhanced gas sensitivity of La-doped ZnO nanoparticles.* Materials Science and Engineering: B, 2007. **141**(1-2): p. 43-48.

Chapter 6- SUMMARY AND CONCLUSION

The Powdered samples of ZnO, 0.2%Pd-ZnO, 0.3%Pd-ZnO, 0.5%Pd-ZnO and 0.7%Pd-ZnO were synthesised using the hydrothermal method. The following techniques were used to characterise these nanoparticles: XRD, SEM with EDS, XPS, Raman and UV/vis. The formation of ZnO was confirmed by XRD technique with all peaks from JCPDS file. The Pd peak which was supposed to be observed at 37.5 degrees from the Pd doped samples namely 0.2%Pd-ZnO, 0.3%Pd-ZnO, 0.5%Pd-ZnO and 0.7%Pd-ZnO did not appear, because this peak was suppressed by the three most intense peaks of ZnO namely (100), (002), and (101). The presence of Pd enhances the structure. This was discovered to be the reason for the Pd doped ZnO samples to have a varied crystallinity, according to XRD analysis. The intensity increases with an increase of the dopant amount; 0.5%Pd-ZnO is an optimal with the highest average crystal size of 37.2452 nm. From the SEM analysis all the particles are large and are in the micro range, agglomeration was more efficient in the presence of Pd. The morphology of ZnO is nanoparticle with a minimal separation of particle and Pd doped ZnO samples are rods with nanoparticles, the growth of rods and nanoparticles is proportional to the Pd concentration, and the growth of nanoparticles is faster than the growth of rods. The EDS analysis was able to detect Zn, O, and Pd from the higher doped samples 0.5%Pd-ZnO and 0.7%Pd-ZnO. The lower doped samples 0.2%Pd-ZnO and 0.3%Pd-ZnO did not show any Pd atom. This is because of the small added amount of Palladium to ZnO.

According to XPS measurement the elemental composition and oxidation of elements within the materials are O1s, Zn2p and Pd3d. The elements were fitted and deconvoluted to their respective energies for all samples, Oxygen showed one peak, while Zn showed two peaks which are $\mathrm{Zn2p_{1/2}}$ and $\mathrm{Zn2p_{3/2}}$. The detection of Pd was from higher concentration decorated samples, 0.5%Pd-ZnO and 0.7%Pd-ZnO. In other samples like 0.2%Pd-ZnO and 0.3%Pd-ZnO it was not observed due to a small, introduced amount of Pd. The Pd element showed two peaks, $\mathrm{Pd3d_{5/2}}$ and $\mathrm{Pd3d_{3/2}}$. The XPS fitting shows that the Zn, O, Pd peaks of the 0.5%Pd-ZnO sample has a greater area, energy (eV) and intensity (a.u) compared to the peaks of the 0.7%Pd-ZnO sample. Raman analysis shows the major dominant sharp peaks of E_2(low) and E_2(high). Raman active optical phonon mode identified as E_2 at 437 cm-1 is an indicator of the wurtzite hexagonal phase of ZnO. E_2(Low) is red-shifted for nanorods and E_2(High) is blue-shifted in all morphologies, but E_2(Low) was not apparent in other structures. E_2(High) mode is blue shifted by 6 units, and ZnO spectra is noisy compared to doped Pd-ZnO samples. This suggests that the pure ZnO samples' crystallinity is lower. However, when the samples have been doped with Pd, a crucial narrowing that denotes greater crystallinity is observed. The 0.5%Pd-ZnO has the smallest Raman shift compared to other samples and the recent literature. (A small Raman shift is associated with weaker or less intense Raman signals).

UV/vis shows the absorption peaks of ZnO, 0.2%Pd-ZnO, 0.3%Pd-ZnO, 0.5%Pd-ZnO, 0.7%Pd-ZnO which are 406 nm, 398 nm, 418 nm, 421 nm, 396 nm respectively. The greatest absorption peak was observed at 421 nm which is for 0.5%Pd-ZnO, and the absorption was mostly centered in the UV area, with minimal absorption of visible light. The 0.2%Pd-ZnO and 0.7%Pd-ZnO samples show a theoretical deviation on the band gap, which is greater than the band gap of pure ZnO, because introducing Pd metal should reduce the band gap. The is a decreasing trend of a band gap from 0.2%Pd-ZnO, 0.3%Pd-ZnO to 0.5%Pd-ZnO then a big increase from 0.5%Pd-ZnO to 0.7%Pd-ZnO which means that 0.5%Pd-ZnO is a sample with the smallest band gap 2.65 eV whereas the ZnO band gap is 2.75 eV.

Gas sensors were tested for ethanol, NO2, SO2, and CO2 gases at different operating temperatures. The gas sensors were made from ZnO, 0.2%Pd-ZnO, 0.3%Pd-ZnO, 0.5%Pd-ZnO, and 0.7%Pd-ZnO nanorods on interdigitated platinum structures. The testing temperature was from 25°C, 75°C, 100°C, 150°C, 200°C to 225°C, the optimal temperature was 150°C. The 0.2%Pd-ZnO sensor outperformed the others in terms of responsiveness and selectivity towards NO2 at an optimal temperature with a response of 3.8, whereas the 0.7%Pd-ZnO sensor performed exceptionally with a response of 6.5 towards ethanol at the same optimal temperature. The 0.5%Pd-ZnO sensor was found to be the best sensor in operating at room temperature towards reducing gases CO2, SO2 and Ethanol. The issue of energy consumption of metal oxide gas sensors with high working temperature is still unresolved hence the 0.5%Pd-ZnO nanostructures prepared in this work display potential solutions. The ZnO sensor did not sense any gas due to overloading caused by high resistance. Improved surface area and point defects (such oxygen vacancies) that reduce band gap and promote gas adsorption could also account for this reaction. It was also noted that when the concentration of the gas grew, the response time decreased.

The results have therefore demonstrated that the current sensor design could significantly help to design sensors for detecting gases emitted by spoiled meats at low temperatures. Also, these sensors will support the creation of an advanced chemical gas sensor with high sensitivity, quick response times, and recovery times.